Università degli Studi di Parma

Dottorato di ricerca in Fisica

XXIV ciclo

Ab-initio simulations of the Al/ZnO interface

Dottorando:
Mirco Bazzani

Relatori:
Prof. Davide Cassi
Prof. Alessandra Catellani

Contents

Chapter 1

Introduction

ZnO is a representative metal oxide wide-gap semiconductor that has been investigated most widely and intensively for basic optoelectronic devices such as ultraviolet light-emitting diodes (UV-LEDs) and thin-film transistors (TFTs) [1, 2], but also for the exploration of new research topics such as defect management, quantum phenomena, and integration with oxides with other functionalities. Most recently, it has found application for the realization of Transparent Conducting Oxides (TCOs), when doped with Aluminum (AZO) or Gallium: these TCOs are basic ingredients in the design of advanced optoelectronic devices and III generation photovoltaic cells, as an efficient contact for electron transport [4–7]. The problem of Aluminum incorporation in the ZnO matrix as dopant and the formation, characterization, and control of metal contacts at the semiconductor surface is a major task for optimizing device applications.

This thesis is devoted to a microscopic description of the Al/ZnO interface, as can be grasped via ab initio Density Functional Theory (DFT) simulations.

1.1 Crystal structure and electronic properties

The ZnO crystal structure is characterized by a tetrahedrally coordinated bonding geometry. Each zinc ion has four oxygen neighbour ions in a tetrahedral configuration and vice versa. This geometrical arrangement, which is well known from, for example, the group-IV elements C (diamond), Si, and Ge, is also common for other II-VI and III-V compounds. It is referred to as covalent bonding, although the bonds may have a considerable degree of polarity when partners with different electronegativity are involved. The tetrahedral geometry has a rather low space filling and is essentially stabilized by the angular rigidity of the binding sp^3 hybrid orbitals. In the crystal matrix, the neighbouring tetrahedrons form bi-layers aligned along

a polar axis: in the ZnO case, each bi-layer consists of a zinc and an oxygen layer. Generally, this arrangement of tetrahedrons may result either in a cubic zincblende-type structure or in a hexagonal wurtzite-type structure, depending on the stacking sequence of the bi-layers.

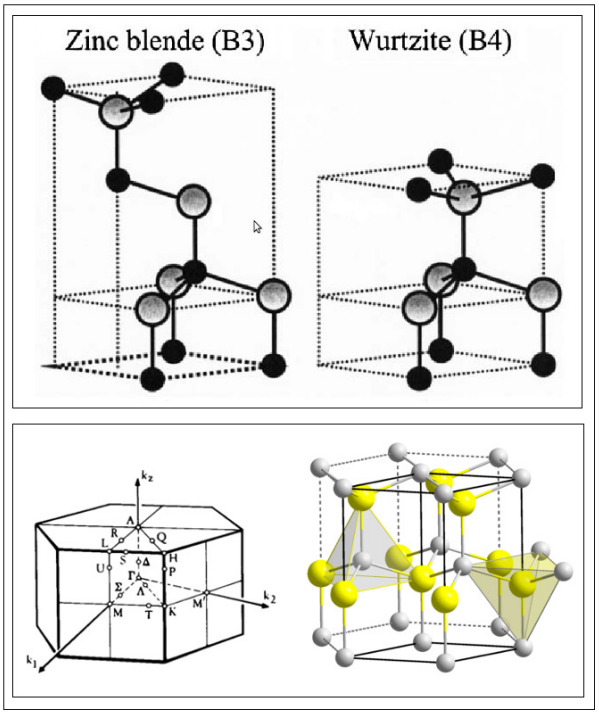

Figure 1.1: ZnO possible structures (top panel), under standard conditions the most stable structure is wurtzite. Bottom panel: Brillouin zone of the wurtzite structure hexagonal cell with high symmetry direction highlighted and the hexagonal elementary cell; the tetrahedral environment of each atom is evidenced.

The stable crystal structure of ZnO is the hexagonal wurtzite (WZ) lattice [8]: it is an uniaxial lattice, and its distinct axis, referred to as c-axis is a polar axis, as said above, and it is directed along one of the tetrahedral binding orbitals (C_{6v} *point group*). This hexagonal c-axis, generally defined as the (0001) direction, corresponds to a body diagonal axis of the cubic structure. In the plane perpendicular to the c-axis, the primitive translation vectors **a** and **b** have equal length and include an angle of 120^o. In contrast to zinc-blende (ZB), the wurtzite primitive unit cell contains two pairs of ions, in our case, two ZnO units. The ZnO bond has a considerable degree of polarity, caused by the very strong electronegativity of the oxygen atom. Wurtzite

does not have a centre of symmetry and no inversion axis: The reduced symmetry of the lattice, with respect to ZB, supports spontaneous polarization, a physical property described by a vector with fixed orientation in the crystal, namely the polar c-axis, which remains invariant under all crystal symmetry operations (rotations about the vector, and mirroring in any plain containing the vector) [9–13]. ZnO is thus a prototype pyroelectric material,. *i.e.* it presents a macroscopic electric polarization, or spontaneous dipole field [14]. In the following, we will describe how these relevant electronic properties and crystal anisotropy affect interface formation, and dopant diffusion.

ZnO-based optoelectronic devices exhibit interesting and attractive properties, many of which originate from the electronic structures inherent to oxides. Because oxides have a strong ionicity, their Conduction Band Minimum (CBM) and Valence Band Maximum (VBM) are usually formed by different ionic species (see Fig. 1.2. CBMs are mainly made up of orbitals from the metal cations, such as Zn^{2+} 4s orbitals and VBMs are mainly made up of O^{2-} 2p orbitals (Figure 1.2d). Oxides have large bandgaps because the large Madelung potential enhances the energy splitting between the cation s and O 2p orbitals. The well-overlapped wave function of the conduction band shown in Fig. 1.2 comes from this fact. That is why ZnO, SnO, and In_2O_3 have small electron effective masses of 0.23-0.35 m_e, where m_e is the mass of a free electron, and unexpectedly high mobility (mobility of ZnO can reach 440 $cm^2/(Vs)$ at room temperature and increases to 5000 $cm^2/(Vs)$ upon cooling to 100 K [15].

To complete the short overview of the very many interesting characteristics of bulk ZnO, it must be mentioned that it exhibits a direct band-gap of 3.37 eV at room temperature with a large exciton binding energy of 60 meV. The strong exciton binding energy, which is much larger than that of GaN (25 meV), and the thermal energy at room temperature (26 meV) can ensure an efficient exciton emission at room temperature under low excitation energy. As a consequence, ZnO is recognized as a promising photonic material in the blue-UV region.

1.1.1 Nanostructures

In addition to this, ZnO has been recently revealed to be extremely versatile for nano-devices: Indeed, the lattice anisotropy allows for different surface structures and anisotropic growth. Under thermodynamic equilibrium conditions, the facet with higher surface energy is usually small in area, while the lower energy facets are larger. Specifically, in the ZnO growth, the highest growth rate is along the c-axis and the large facets are usually the $(01\bar{1}0)$ and $(2\bar{1}\bar{1}0)$. By controlling the growth kinetics, deposition temperatures and

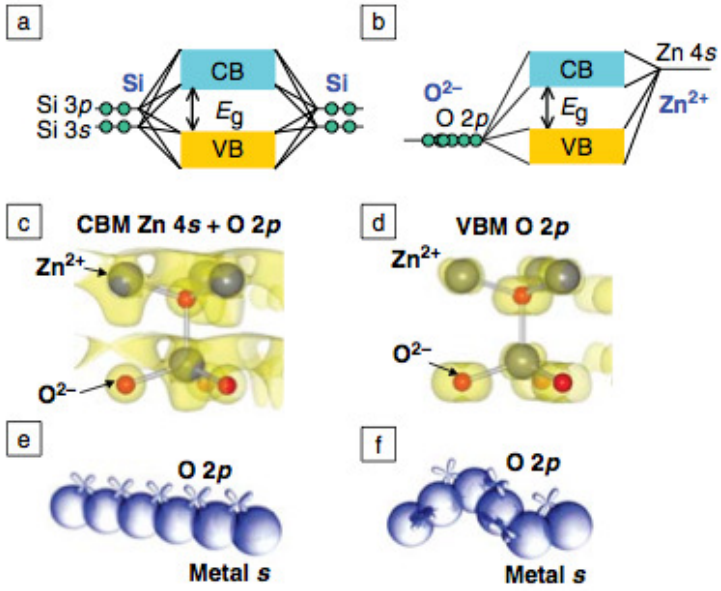

Figure 1.2: Schematic band structures of (a) Si and (b) ZnO. In typical oxides, a conduction- band minimum (CBM) is formed mainly by metal s orbitals, and a valence-band maximum (VBM) is formed mainly by O 2p orbitals, as seen in the wave functions of the (c) CBM and (d) VBM. (e) Schematic wave function of the CBM in an oxide crystal, which is formed by spatially overlapping metal s orbitals. (f) Even in a disordered structure such as an amorphous oxide, the magnitude of the overlap between the neighboring metal cations is not significantly modified. From [3].

pressures it is possible to change the growth behaviour and obtain low cost production of nanorods, ultralong nanobelts with diverse facets, nanocombs, branched hierarchical structures, nanohelixes and nanorings.

These nanostructures can be optimized to enhance specific characteristics and develop nano-devices (see e.g. [22] and references therein): Field effect transistors have been fabricated using individual nanobelts, where the nanobelt conductivity can be tuned by controlling its surface and volume oxygen deficiency; gas and chemical nano-sensors can be easily obtained by nano-belts, or bundles of nanowires; nanowires (NWs) can also be optimized to show quantization of thermal conduction at low temperatures, due to increased phonon-boundary scattering and modified phonon dispersion; nanowires and nanobelts can be the active element in nanoresonators and nano-cantilevers, and profit of the high piezoelectric constants of ZnO;

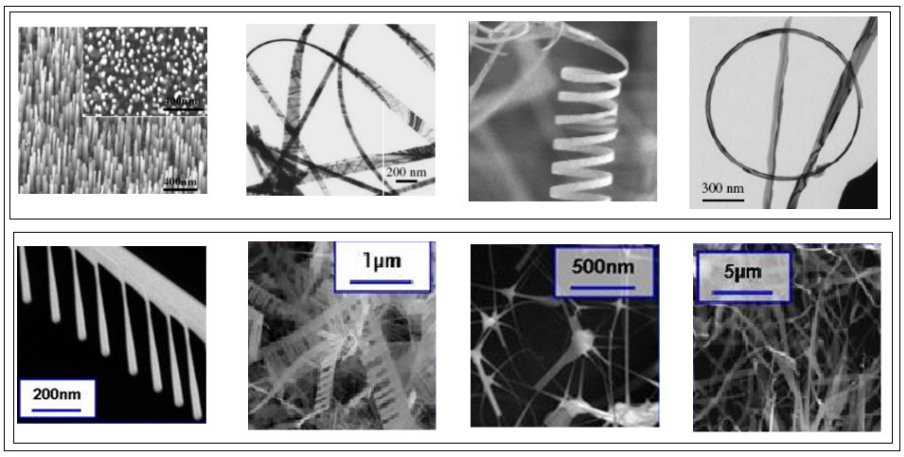

Figure 1.3: Some examples of ZnO nanostructure from [22] (top panel) and courtesy A. Zappettini et al. IMEM CNR Parma.

while ZnO nanowires have demonstrated UV lasing at room temperature.

Finally, recent applications in energy have been proved and optimized: on one side, researchers have taken advantage of the unique coupled semiconducting and piezoelectric properties of zinc oxide nanowires to create piezo-generators, opening the field of nano-piezotronics [17]. Furthermore, functionalized ZnO nanowires, grown on transparent conducting oxide substrates, were integrated as the wide band gap semiconductor into dye-sensitized solar cells: the crystallinity and orientation of the wires should allow for reduced losses at the dye/semiconductor interface and improved electron transport, that would change from hopping-percolation type to drift type transport (see e.g. [18] and Fig. 1.4).

1.1.2 The interface with metals

For any real application, a fundamental issue is the formation, control and characterization of a metal contact: this may be a fundamental issue in wide gap semiconductors in general, and in particular in low-symmetry crystal such as ZnO, and its nano-structures. Indeed, while for example the idea of the epitaxial growth of quasi-one-dimensional (1D) ZnO nanostructures on a TCO as structurally commensurated as possible (Fig . 1.4) is particularly appealing, since this would give the possibility to realize an oriented matrix without boundaries and to improve in this way the efficiency in charge transport, reducing the contact resistance between the ZnO and the TCO contact, real world is made harder by a number of difficulties. First of all, it

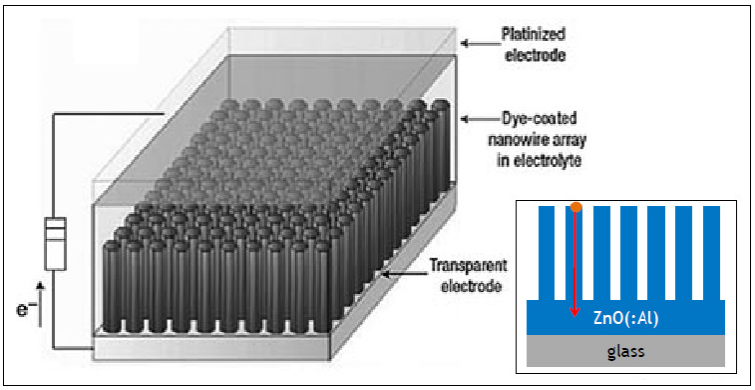

Figure 1.4: Schematic representation of DSSC (dye sensitized solar cell). Inset: a DSSC detail, the interface between AZO (transparent electrode) and ZnO wires.

is commonly recognized that doping of oxides is a complex problem [19, 20]: several efforts have been conduced to understand and optimise doping. Recently many computational efforts have been devoted to study defect formation and doping mechanisms mainly on bulk system, and on the basis of ab initio thermodynamics considerations [23], without taking into account the boundary problems offered by the presence of realistic low symmetry lattice structures (such as nanowires). Furthermore, not only dopant stability but diffusion also can be affected by the presence of boundaries and crystal anisotropy [20]. From the purely theoretical point of view, moreover, the study of complex oxides that involve d-states, and often crystallize in low symmetry lattices compatible with the presence of spontaneous polarization fields, is still the subject of intense debate [21, 22].

As mentioned above, an extremely new field is the realization of Transparent Conducting Oxides (TCOs) for application as electrodes in photovoltaic (PV) devices of novel generation [4]. In particular, it has been recently proposed that Aluminum-doped zinc oxide (AZO) films can be the optimal choice as an epitaxially matched TCO layer in ZnO NW-based dye-sensitized solar cells (DSSCs), since it has been observed that the optical, electrical, structural and morphological properties of the TCO films are essential in determining device performances.

Although AZO films have been successfully grown, the local geometry of the Al inclusion, the diffusion mechanisms, and the electronic properties of the system are still completely non characterized [24–27]. Transparent conductive oxides have attracted much interest, not only from the experimental realization, and for their applications in optoelectronic devices,

such as solar cells and liquid crystal displays, due to their high conductivity and high transparency in the visible region. Indeed, the remarkable combination of conductivity in an albeit wide-gap (i.e., transparent) material is not fully understood, along with the effect of dopants on charge transport: these issues contrast with the standard classification between zero-gap conductive and finite-gap optical materials and are still the subject of intense debate [21,22,28]. Hence, a full understanding of the formation, stability, and solubility properties of TCOs still constitutes a fundamental challenge and a technological goal.

Another fundamental issue towards the application is the formation of metal contacts. Metal/ZnO interfaces are central to all ZnO electronic devices, yet their electronic properties have only recently been explored in detail [2, 29, 31]. It has been shown that all the measured barrier heights are lower than the predicted Schottky-Mott values and do not vary accordingly to the difference in work function values [32]. The failure of the Schottky-Mott theory to predict the Schottky barrier heights (SBHs) indicates that interface features such as surface contamination, interface native defects, chemical bonding etc. play a very important role. Furthermore, to fabricate a high-performance optoelectronic device, low-resistance Ohmic contacts are essential. However, only a few results for Ohmic-contact formation on ZnO were reported [33–35]. From the theoretical point of view, beyond phenomenological models based on the branching point energy [38], a description of the metal/semiconductor interface can be performed via ab initio methods [39]. A detailed analysis of the effects of polarization fields and reduced lattice symmetry or structure boundaries (such as in NWs) are however lacking: these constraints pose further complications to a rather complex task.

1.2 This work

This thesis is part of a broad effort aimed at gaining a better description of the active elements in functionalized (hybrid and fully inorganic) nanostructures for energy applications, and a deeper understanding of charge and energy transfer mechanisms in these complex systems. Beside the fundamental interest in the challenging topics related to material science and nano structures, the control of the interactions at these interfaces offers a unique opportunity to unravel the interplay between structures and functionalities of increasing complexity and technological relevance. Our approach is based on ab initio Density Functional Theory (DFT) simulations and it consists in focusing on relevant microscopic properties and processes that characterize the fundamental building blocks of ideal structures and interfaces.

1.2.1 Selected Systems

AZO - The first task is related to the ab initio simulation of Aluminum-doped zinc oxide (AZO) as a TCO layer: first principles theoretical investigations offer the unique possibility of characterizing the optoelectronic properties of TCO at the microscopic level, taking directly into account the interplay between the electronic and structural properties of the system. Experimental findings suggest that Aluminum atoms into ZnO bulk substitute Zn ions inside the wurtzite structure. Preliminary DFT results on ZnO bulk systems including substitutional Al ions, reveal that the presence of Aluminum impurities does not modify the main features of ZnO bulk structure but promotes a strong shift of the Fermi level into the original conduction band of the metal-oxide compound, i.e. acting as n-dopant. As a result the system becomes conductive in agreement with the experimental findings [40, 41]. However, there is still not a clear description of the capability of Al ions to penetrate and diffuse inside the ZnO material, as well as to substitute covalently bonded Zn-ions in the crystalline structure: important physical quantities such as the penetration length, the reaction pathway and the energy barrier for the Al substitution are completely missing.

We simulated the effects of n-doping in ZnO material, via Al incorporation in the crystal matrix. We have considered different doping regimes, and different Al sites, comparing substitutional (at Zn) and interstitial defects: we provided a structural and electronic characterization of the compound by means of state-of-the-art plane-wave pseudopotential DFT total-energy-and-force minimization DFT code (Quantum-ESPRESSO suite [42]).

ZnO(0001) surface - In the same theoretical framework, we addressed the ZnO polar surfaces stabilization problem. This is very important to correctly approach the study of the Al/ZnO contact and to take into account the dipole field effects at the metal/semiconductor interface. The problem of ZnO polar surface stabilization has been an open, quite complicated, question for several years: a perfect agreement between theory and experiment must still be achieved, since, especially for highly reactive unstable surfaces, the particular reconstruction observed by a given experimental technique depends on growth ambient and preparation condition of the sample. Furthermore the most common theoretical solutions to quench the internal field treat the problem of polar surfaces mainly from the thermodynamic point of view, while the characterization of the electronic properties is almost lacking.

For these reasons we directly addressed the theoretical problem of the polar surface stabilization by means of ab initio DFT calculations. We compared different stabilization solutions, such as vacancies and hydroxylation, providing for each considered system the structural and electronic character-

ization.

Al:ZnO(0001) interface - After addressing the problem of ZnO polar surfaces stabilization we focused on the main target of the PhD project: the Al/ZnO(0001) interface simulation.

This aim is very challenging and actual due to the discrepancy between the different theoretical models and experiments, however, the determination of the behavior (Ohmic vs Schottky) is mandatory for an optimal modeling of any ZnO based device. This scenario is complicated since, from the experimental point of view, Schottky barrier height is found to vary depending on many interface factors such as the presence of defects and growth conditions. The presence of an internal polarization field poses further complexity to the issue: the microscopic description of the structural and electronic properties of the interface, as obtained by ab initio simulations, may be a fundamental tool to complement the experiments.

We simulated different interface systems, in presence or not of ZnO surface reconstructions in order to quantify and isolate the interface dipole field effects. We considered also free and buried interfaces for comparison. For all the studied interface systems an electronic and structural characterization was provided and finally an estimate for the Schottky barrier height is proposed.

1.2.2 Selected Methods

As already stated, the activity is based on state of the art total-energy and force calculations, in the framework of DFT: in particular we made use of the code PWscf, which is included in the Quantum-ESPRESSO (QE) package [42]. QE is a free linux-based suite of codes distributed under GNU license and explicitly implemented for the ab initio simulation of large-scale systems. QE codes are parallelised in MPI, and implemented on different architectures, including IBM-sp6 and Blue-Gene, as available in CINECA, Casalecchio (Italy) [42].

All calculations required the use of super cells of large number of atoms: (i) The realistic low Al dosage, necessary to simulate the dopant diffusion on metal-oxide materials, below solubility limit ($<$ 3-4 %) and (ii) the description of the "epitaxial" interface between Al and ZnO(0001) in such a way that no material was under strain, both required large super cells. The inclusion of Zn atoms and their 3d electrons explicitly, along with the need of sampling different configurations, made such ab initio calculations a formidable computational task which requires massive parallel computation, in terms of both CPU time and processor number for its completion.

Beyond total-energy-and-force-minimization and molecular dynamics, the

QE suite contain a large number of postprocessing tools for the analysis of result. Among these different tools, it should be mentioned epsilon.x, designed to evaluate the dielectric response of the material in the framework of band theory, without an explicit description of the electron-hole interaction, that allowed us to describe AZO properties.

1.2.3 Scheme of the Thesis

The thesis is divided in different chapters, according to the different systems studied:

The second chapter provides a short summary of the theoretical background and a description of main computational ingredients .

The third chapter is dedicated to the description of Al-doped ZnO: this is indeed already a published paper, which is presented as such. It contains a thorough analysis of the dopant effect, which provides in particular an explanation to the experimental observation of detrimental effects at high Al dosage on the optoelectronic properties of the compound. Our results unambiguously allowed to determine the role of interstitials in the cancellation of transparency, and reduced electron mobility.

The fourth chapter is devoted to a description of the clean ZnO(0001) surface. Although already largely studied both from an experimental and theoretical point of view, the available results on this polar surface are still controversial. The ideal truncated surface indeed is unstable, and a number of possible charge compensation mechanisms occur, depending on different ambient conditions. This subject is furthermore required for the subsequent analysis of the Al/ZnO(0001) interface. We have thus provided a detailed study of the electronic properties of the surface, with a thorough analysis of the electrostatics of the system, totally absent in the literature.

The Al/ZnO(0001) interface is the argument of the last chapter. Here the effects of spontaneous polarization play a fundamental role for the understanding of the electronic properties of the interface. We compared different possible configurations of the interface, to complement controversial experimental data.

The topics described above are contained in the papers included in this thesis or in preparation, and were presented at international seminars and conferences. Bibliography and the full list of the published and submitted papers is given in the last section of the thesis.

The reports of the different projects submitted to CINECA to obtain computer time are also included as appendix.

Bibliography

[1] A. Tsukazaki, A. Ohtomo, T. Onuma, M. Ohtani, T. Makino, M. Sumiya, K. Ohtani, S.F. Chichibu, S. Fuke, Y. Segawa, H. Ohno, H. Koinuma, M. Kawasaki, Nat. Mater. **4**, 42 (2005)

[2] K. Nomura, H. Ohta, A. Takagi, T. Kamiya, M. Hirano, H. Hosono, Nature **432**, 488 (2004)

[3] Toshio Kamiya and Masashi Kawasaki, MRS Bull. **33**, 1061 (2008)

[4] H.L. Porter et al. , Mater. Sci. Eng. B **119**, 210 (2005)

[5] S Tricot et al. J. Phys. D: Appl. Phys. **41**, (2008)

[6] Sung-Hae Lee, et al., J. Phys. Chem. C **114**, 7185, (2010)

[7] X. Jiang, F.L. Wong, M.K. Fung, S.T. Lee, Appl. Phys. Lett. **83**, 1875 (2003)

[8] Landolt-Boernstein - *Group III Condensed Matter Numerical Data and Functional Relationships in Science and Technology, Volume 41B: II-VI and I-VII Compounds; Semimagnetic Compounds*, Edited by O. Madelung, U. Roessler, M. Schulz

[9] L. Landau and E. Lifshitz, *Electrodynamics of Continuous Media* (Pergamon, Oxford, 1984);

[10] J. Nye, *Physical Properties of Crystals* (Oxford University Press, London, 1957);

[11] R. M. Martin, Phys. Rev. B **9**, 1998 (1974);

[12] R. Resta, Rev. Mod. Phys. **66**, 899 (1994);

[13] R. D. King-Smith and D. Vanderbilt, Phys. Rev. B **47**, 1651(1993)

[14] Andrea Dal Corso, Michel Posternak, Raffaele Resta, and Alfonso Baldereschi, Phys. Rev. B **50**, 10715-10721 (1994)

[15] A. Tsukazaki, A. Ohtomo, M. Kawasaki, Appl. Phys. Lett. **88**, 152106 (2006)

[16] Zhong Lin Wang, J. Phys.: Condens. Matter **16** (2004) R829

[17] Xudong Wang, Jinhui Song, Jin Liu, Zhong Lin Wang, Science **316**, 102 (2007)

[18] Kurtis S. Leschkies, Ramachandran Divakar, Joysurya Basu, Emil Enache-Pommer, Janice E. Boercker, C. Barry Carter, Uwe R. Kortshagen, David J. Norris, and Eray S. Aydil, Nanoletters **7**, 1793 (2007)

[19] J. A. van Vechten, in *Handbook of Semiconductors*, edited by S. P Keller - North-Holland, Amsterdam, 1980.

[20] J. Simon, et al., Science 327, **60** (2009); Phys. Rev B **79**, 241308 (2009)

[21] S. Lany and A. Zunger, Phys. Rev. B **78**, 235104 (2008)

[22] A. Janotti, D. Segev, C.G. Van de Walle,Phys. Rev. B **74**, 045202 (2006).

[23] S. Lany, J. Osorio-Guillasson, and A. Zunger , Phys. Rev. B **75**, 241203, (2007).

[24] Mercedes Gabas, Piero Torelli, Nicholas T. Barrett, Maurizio Sacchi, Fabien Bruneval and Ying Cui, Laura Simonelli Phys. Rev. B **84**, 153303 (2011)

[25] S. B. Majumder, M. Jain, P. S. Dobal, and R. S. Katiyar, Mater. Sci. Eng. B **103**, 16 (2003)

[26] T. Minami, Semicond. Sci. Technol. **20**, S35 (2005).

[27] J. Huepkes, J. Mueller, and B. Rech, *Transparent Conductive Zinc Oxide. Basics and Applications in Thin Film Solar Cells*, edited by K. Ellmer, A. Klein, and B. Rech, Springer Series in Materials Science (Springer, Berlin, Heidelberg, New York, 2007)

[28] P. Agoston, K. Albe, R. M. Nieminen, and M. J. Puska, Phys. Rev. Lett. **103**, 245501 (2009)

[29] B.J. Coppa, R.F. Davis, and R.J. Nemanich, Appl. Phys. Lett. **82**, 400 (2003)

[30] H.L. Mosbacker, Y.M. Strzhemechny, B.D. White, P.E. Smith, D.C. Look, D.C. Reynolds, C.W. Litton, and L.J. Brillson, Appl. Phys. Lett. **87**, 012102 (2005)

[31] M.W. Allen, M.M. Alkaisi, and S.M. Durbin, Appl. Phys. Lett. **89**, 103520 (2006)

[32] K. Ip, G.T. Thaler, H. Yang, S.Y. Han, Y. Li, D.P. Norton, S.J. Pearton, S. Jang, and F. Ren, J. Cryst. Growth **287**, 149 (2006)

[33] T. Akane, K. Sugioka, and K. Midorikawa, J. Vac. Sci. Tech- nol. B **18**, 1406 (2000)

[34] H.K. Kim, S.-H. Han, W.-K. Choi, and T.Y. Seong, Appl. Phys. Lett. **77**, 1647 (2000)

[35] S. Y. Young Kim, H W Jang, J K Kim, C M Jeon, W I Park, G C Yi, and J L Lee, Journal of Electronic Materials, Vol. **31**, No. 8, (2002)

[36] J. Hubbard, *Proc. Roy. Soc. London* 285:542, (**1965**)

[37] H. J. Monkhorst, and J. D., Phys. Rev. B **13**, 5188 (1976).

[38] M.W. Allen and S. M. Durbin Phys. Rev. B **82** 165310 (2010)

[39] M Peressi, N Binggeli and A Baldereschi J. Phys. D: Appl. Phys. **31** (1998) 1273-1299.

[40] Stephan Lany and Alex Zunger, Phys. Rev Lett. **98**, 045501 (2007)

[41] M. Bazzani, A. Calzolari, A. Catellani: *Ab Initio simulation of Al doped ZnO(AZO)*, presented at Hands on Tutorial on Ab Initio Molecular Simulations: Toward a First Principles Understanding of Materials Properties and Functions, Berlin, June 2009, manuscript in preparation.

[42] Paolo Giannozzi, Stefano Baroni, Nicola Bonini, Matteo Calandra, Roberto Car, Carlo Cavazzoni, Davide Ceresoli, Guido L Chiarotti, Matteo Cococcioni, Ismaila Dabo, Andrea Dal Corso, Stefano de Gironcoli, Stefano Fabris, Guido Frates, Ralph Gebauer, Uwe Gerstmann, Christos Gougoussis, Anton Kokalj, Michele Lazzeri, Layla Martin-Samos, Nicola Marzari, Francesco Mauri, Riccardo Mazzarello, Stefano Paolini, Alfredo Pasquarello, Lorenzo Paulatto, Carlo Sbraccia, Sandro Scandolo, Gabriele Sclauzero, Ari P Seitsonen, Alexander Smogunov, Paolo Umari and Renata M Wentzcovitch, J. Phys. Condens. Matter **21**, 395502 (2009)

Chapter 2

Elements of computational materials science

In this chapter we describe the basic ideas of density functional theory, and the approximate methods which in conjunction with todays powerful computing machinery allow the principles of quantum mechanics, which we usually call first, or ab initio principles, to be applied to complex poly-atomic systems.

An important simplification is obtained by using the Born-Oppenheimer (BO) approximation to separate the motion of the nuclei from the electronic degrees of freedom. The Hamiltonian of the system consisting of n electrons with coordinates $r \equiv \{r_i\}$ and N ions at positions $R \equiv \{R_i\}$ can be expressed as:

$$H = T_R^I + T_r^e + V^{eI}(R, r) + V^e(r) + V^I(R) \tag{2.1}$$

where the first two terms are the kinetic energies of the ionic and electronic subsystems, and the contributions of the electron-ion, electron-electron, ion-ion Coulomb interaction are denoted V^{eI} , V^e , and V^I . We can rewrite the total Hamiltonian as

$$H = T_R^I + H_0 \tag{2.2}$$

H_0 being the Hamiltonian of the system for fixed nuclei $H_0 = T^e + V^{eI} + V^e + V^I$. We can consider the Hamiltonian of Eq. 2.2 on the basis of the perturbation theory because of the usually small T^I due to the large masses of the atomic nuclei compared with the electron ones ($M_I \sim 2103 m_e$). As a result of this approximation, known as the Born-Oppenheimer approximation [1], the total system wave function, i.e. the solution of the Schroedinger equation $H\Psi(R, r) = E\Psi(R, r)$ is written as a product of two wavefunctions that depend separately on the electronic and ionic degrees of freedom: $\Psi(R, r) = \Psi_R(r)\Phi(R)$. This factorization offers the possibility to solve separately the electronic problem, which still is in general a manybody problem.

2.1 DFT, Kohn-Sham theorem and exchange and correlation functionals

In order to treat the electronic degrees of freedom of the system, we used the Density Functional Theory, based on the two theorems by Hohenberg and Kohn [2], which show that all ground state properties of a system can be deduced from the electronic density only, and that this density can be found by minimising the expectation value of the Hamiltonian as a functional of the density. We will be working within the Kohn-Sham [3] theorem, which consists of the replacement of the original many-electron problem by a problem of fictious non-interacting electrons in a self-consistent, density-dependent potential (Kohn-Sham (KS) potential). The non-interacting problem is devised as to reproduce the density of the interacting electrons. In this ansatz, the kinetic energy is obtained directly from the non-interacting wavefunctions, while other energetic terms are computed from the density. The Kohn-Sham potential (Eq. 2.3) is determined by the ionic Coulomb potential, by a Hartree term which describes electron-electron classical Coulomb interaction, and by a so-called exchange-correlation term, which describes quantum corrections to electron-electron interaction, effects of correlation, and corrections to the kinetic energy between the true interacting electrons and the Kohn-Sham non-interacting electrons.

$$V^{\sigma}_{KS}([n],\vec{r}) = V_{ext}(\vec{r}) + V_{Hartree}([n],\vec{r}) + V^{\sigma}_{XC}([n],\vec{r}) \tag{2.3}$$

Here we indicate with V^{σ}_{KS} the effective Kohn-Sham potential (at position r, with a functional dependence on the density n), V_{ext} the ionic Coulomb potential, V^{σ}_{XC} the exchange-correlation term and with σ the spin index. The non-interacting pseudo-electrons are then described by the Hamiltonian:

$$H^{\sigma}_{KS}([n],\vec{r}) = -\frac{1}{2}\nabla^2 + V^{\sigma}_{KS}([n],\vec{r}) \tag{2.4}$$

Unfortunately, the effect of exchange and correlation is not known exactly, since the Hohemberg and Kohn theorem asserts the existence of the universal functional, but it does not tell us how to construct it. Therefore the second approximation beyond BO resides in the choice of an exchange-correlation (XC) functional (we present some of the main families of XC functionals in the following subsections). All the potential terms are dependent on the electronic density, which lead to a "self consistent-field" (SCF) calculation (see Fig. 2.1) when the density is computed from the KS wavefunctions. This density leads to calculation of a new KS potential, which is in turn used to calculate new wavefunctions, and so on until a certain convergence criterion for charge density is fulfilled.

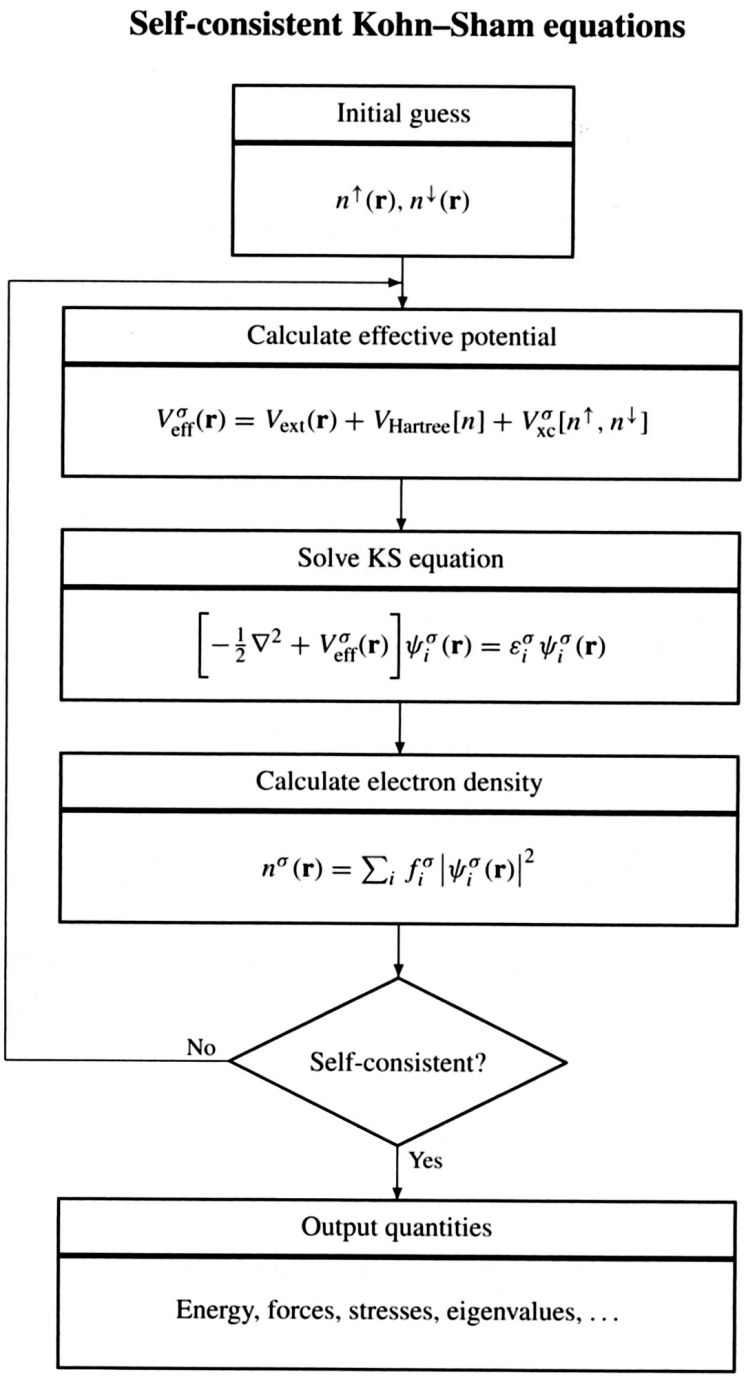

Figure 2.1: Schematic view of the self-consistent procedure to solve Khon-Sham equations obtaining the charge density ground state.

2.1.1 LDA and GGA exchange-correlation functional approximations

In the previous section the many-body problem was reduced into the form of a single-particle problem, by means of an exact formalism. The whole complexity of the electron-electron interaction was confined in the exchange-correlation term. Since DFT does not provide the analytical expressions of the functional $E_{XC}[n]$, the practical application of the theory requires the choice of approximated forms for $E_{XC}[n]$. Over the years many approximate expression have appeared, the most simple and widely used of which is the local density approximation (LDA). In a homogeneous gas of interacting electrons the density is constant and the exchange-correlation energy per particle $\epsilon_{xc}(n)$ is a function (not a functional) of the density. The total exchange-correlation energy is obtained by multiplying ϵ_{xc}^{hom} (exchange-correlation energy per particle for a homogeneous gas of interacting electrons) by the total number of electrons present in the gas: $E_{XC}[n] = N\epsilon_{xc}^{hom}(n)$. Within the approximation of local density, the non-homogeneous electron gas is treated in complete analogy: the total exchange-correlation energy is obtained by accumulating the contributions from every portion of the non-uniform gas as if it was locally uniform

$$E_{XC}^{LDA} = \int n(r)\epsilon_{xc}^{hom}(n(r))dr \tag{2.5}$$

In calculating the integral of Eq. 2.5 the function ϵ_{xc}^{hom} is evaluated for the local density n(r) of the inhomogeneous system under consideration: $\epsilon_{xc}^{hom} = \epsilon_{x}^{hom} + \epsilon_{c}^{hom}$ is the exchange and correlation energy per electron in the homogeneous electron gas of density n. The exchange part ϵ_{x}^{hom} is known explicitly from the theory of the homogeneous electron gas (see for example [4]), while the correlation part ϵ_{c}^{hom} ia available explicitly in the low- and high-density limits [5,6].

LDA is exact for an uniform system and is expected to be valid for systems with slowly varying electron density. For all the other cases the LDA approximation is indeed uncontrolled; its justification relies mainly upon its ability to reproduce the experimental ground-state properties of a large number of solids. This fact can be explained by observing that the exchange-correlation energy functional $E_{xc}[n]$ depends on the spherical average of the exchange-correlation hole. Thus, in first approximation it is not necessary for LDA to reproduce the details of the exact exchange-correlation hole, but it is sufficient that a good estimate of its spherical average is provided by the approximation [7]. LDA performs best to describe the ground state properties of nondegenerate systems. As regards to cohesion and binding, the LDA is found to "overbind". As a result, the calculated cohesive energies of solids and

atomization energies of molecules come out larger compared to experiments, and the lattice constants and bond lengths are smaller. For a comprehensive overview of the LDA/LSDA the reader is referred to the already cited Ref. [8, 9].

A number of methods have been developed to correct the deficiencies of the LDA. For a system of nonuniform density, E_{XC} is no longer adequately reproduced by Eq.2.5. A simple modification appears to be the inclusion of gradient terms ∇n, which leads to the Generalized Gradient Aproximation (GGA) [10],

$$E_{XC}^{GGA} = \int f(n, \nabla n) dr \tag{2.6}$$

Various recipes for constructing $f(n, \nabla n)$ have been proposed. In the following we will consider the gradient-corrected correlation functional of Perdew, Burke and Ernzerhof (PBE) [10].

Density functional theory with Hubbard term

Being proposed to describe ground state properties, both the LDA and the GGA generally exhibit a considerable underestimation of the semiconductor band gap: beyond optical properties and comparison with experimental information on excited states, not addressed by the theory, this problem in general affects also the calculated defect formation energy (see e.g. [11], and references therein). Thus, defect calculations based on LDA or GGA generally require ex post facto corrections which are applied to supercell total energies after the self-consistent calculation. Recent advances in electronic structure theory hold promise for band-gap-corrected ab initio methods, such as GW, exact-exchange, hybrid DFT, or Self Interaction Correction (SCI), to mention a few. These approaches are in general too demanding from the computational point of view to treat problems like defects, that require expanded supercells to approach the experimental dilution values.

A computationally expedient post-LDA is LDA+U [12, 13], which was originally developed to improve the LDA description of Mott insulators by introducing Hubbard-type interactions into LDA via an adjustable Coulomb parameter U [14]. The model has been fully developed in the self-consistent scheme and included in the Quantum-ESPRESSO codes by Cococcioni and De Gironcoli [15].

It has to be mentioned that in non-strongly correlated systems the band-gap correction is generally not achieved for physically meaningful values of U. A full band-gap correction can be empirically achieved, however, when LDA+U is used for the cation d states and, simultaneously, for anion or cation s states. Since the LDA+U method requires adjustable parameters for

the Coulomb and exchange energies U and J, physically meaningful values for these parameters have to be found. Possible strategies to determine suitable parameters are the adjustment of U_l so to reproduce experimental photoemission spectra, constrained LDA calculations, thermochemical considerations, or a self-consistency requirement between U and the orbital partial occupancies.

In the description of Al doping and diffusion in ZnO, we have adopted this coice: we use different U values for the Zn-3d, and for the O-2p states, calculated so to optimize the experimental band-gap in ZnO, and the energy position of Zn-3d states as obtained from photoemission experiments [30]: this approach will be described in details in the forthcoming Par. 2.3.3

We further note that there exists an additional complication with this method for defect formation energy calculations because of the need to calculate elemental reference energies [16] of the Zn metal and of the O_2 molecule in the case of ZnO: On one hand the appropriate U value for the Zn d states should be smaller in the metallic element than in the semiconductor ZnO, due to stronger screening. On the other hand, total energies should in practice be compared only for the same U. Thus we will use the experimental heat of formation to determine defect formation energies under both the metal-rich and the anion-rich conditions.

2.1.2 Practical aspects of DFT implementation scheme

Pseudo-potentials

Most atoms have core electrons which do not participate in chemical bonding and whose wavefunctions are not considerably affected by the environment. Thus, it is common to replace the core electrons and the nuclei by some pseudopotentials (PPs), which will be the third main approximation of the method described in this chapter. These are designed so that beyond a certain "core radius", the valence electron wavefunctions should be the same as it would within the all-electron atom. This approximation leads to two great gains in terms of computational time: first, it reduces drastically the number of electrons to be simulated; secondly, it reduces the number of plane waves (PWs) basis functions needed for an accurate description of the outer orbitals. It is important that the eigenvalues of the pseudowavefunctions coincide with the single particle energies of the all-electrons atom in a wide range of energy in proximity of the valence and conduction band, and that the corresponding wavefunctions coincide outside the core region (defined by a certain cutoff lenght r_c):

$$\phi(r) = \phi^{PP}(r) \quad for\ r > r_c \tag{2.7}$$

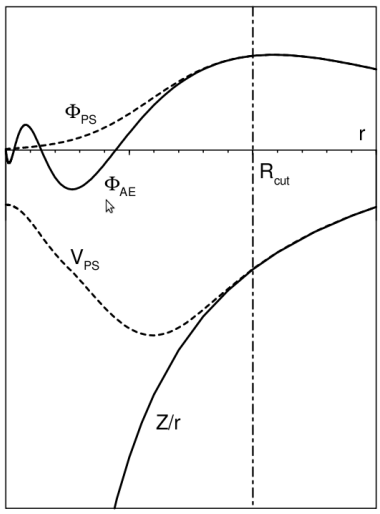

Figure 2.2: The smoothest behaviour of Pseudo-potential and wave function in the core region $r < r_c$. Outside this region they coincide.

Thus, a crucial parameter in the construction of atomic pseudopotentials is the cutoff radius r_c (see Fig. 2.2), dividing the electron sphere into a core region (chemically inert) $r < r_c$, and a valence region $r > r_c$ where chemical bonding takes place. The choice of r_c should ensure that the pseudopotential describes adequately the scattering properties of the ion in diverse atomic environments, a property usually referred to as *transferability*.

An additional requirement is the norm conservation of the pseudo-wave function, which leads to physical electron density. The price to be paid for norm conservation is nonlocality, i.e. the ionic pseudopotentials depend upon the angular momentum l. For this reason the PP is conveniently split in a local and nonlocal part $V_{atom} = V_{local} + V^l_{nonloc}$, where the last term is a sum over all l components of the atom.

Beyond norm-conserving pseudopotentials, recently a different approach has been proposed by Vanderbilt [18]. The so-called ultra-soft pseudopotentials still benefit of an ab initio description, although relaxing the requirement of norm-conservation, and are thus particularly suited to treat first-row elements, or large, complex systems. This sort of pseudopontials will be adopted throughout this work.

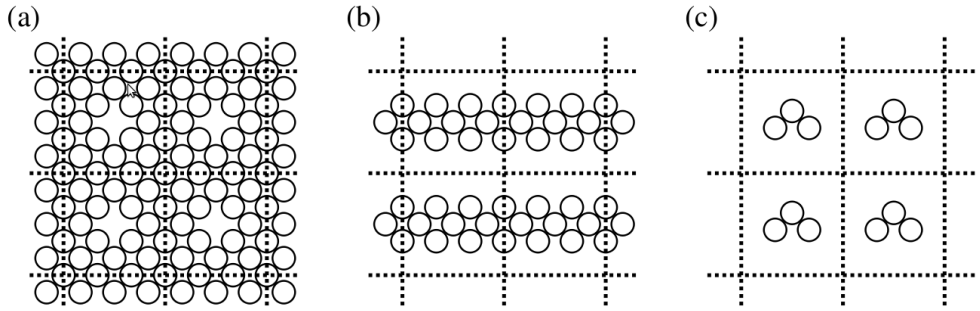

Figure 2.3: Supercell schematisation: a) bulk system in presence of a defect, b) surface system and c) isolated molecule.

Supercell approximation and plane-wave basis set

The supercell method is the ubiquitous approach for the study of solid-state systems where ideal periodicity is broken by e.g. defects or surfaces, to recover periodic boundary conditions. In principle, a solid may also be approximated by means of a large cluster. For sufficiently large clusters, the quantum mechanics of the centre-most atoms approximate those in a solid. However, the size of cluster required to approximate a solid is large due to the dominance of surface over bulk atoms in small and medium sized clusters. This consideration applies to all electronic structure methods, and the best general solution is to use a limited number of repetition of a primitive cell combined with periodic boundary conditions. In the supercell approach an artificial periodicity is imposed on the simulation cell to better model the continuum properties of the system. Bloch's theorem and Fourier representation may then be applied to the wavefunctions. For perfect crystals, a limited number of repetition of the primitive cell are used. The supercell must be large enough that these spurious interactions between replicas are negligible.

The supercell approach is particularly useful when systems in presence of defects or surfaces must be simulated as in the present work (see Fig. 2.3). A surface, for example is modeled with supercells containing a slab consisting of a given number of atomic layers and a vacuum region whose thickness should be chosen large enough in order not to introduce artifacts from the artificial periodicity along the surface normal. Also the slab thickness has to be sufficiently large to avoid the interaction between the two surfaces of the slab.

Since with the supercell approach Bloch's theorem and Fourier representation may be applied also to non periodic systems, let's see the implications

for Khon-Sham equations.

The Bloch theorem allows one to classify the electronic states of the Khon-Sham equations, $\phi(r)$ with $i = 1, .., N_{occ}$ with N_{occ} being the number of the occupied orbitals $N_{occ} = N_{nel}/2$, by a band index v and by the k vectors in the Brillouin Zone (BZ): $\phi_{v,k}(r)$. There are N discrete values of k in the BZ, as determined by the Born-von Karman periodic boundary conditions [19, 20], and $N_v = n_{el}/2$ valence bands, each of them occupied by two electrons. The Bloch states can be expanded in plane waves with the appropriate translational symmetry:

$$\phi_{v,k} = \sum_G c_{v,k+G}|k+G\rangle \qquad where \;\; |k+G\rangle = \frac{1}{N\Omega}e^{i(K+G)\cdot r} \tag{2.8}$$

the sum runs over an infinite number of Bravais G-vectors of the reciprocal lattice. In practice, however, one uses a truncated plane-wave expansion to include N_{PW} terms with kinetic energies only up to certain cutoff E_{cut} ,

$$|k+G| \leqslant E_{cut} \tag{2.9}$$

A sphere of radius $G_{max} = \sqrt{E_{cut}}$ and center k is constructed in reciprocal space and all reciprocal lattice vectors within or on the sphere are included in the expansion. Clearly N_{PW} depends on k, though not heavily, since k is a reduced wave vector, so the wave- functions $\phi_{v,k}$ are described with almost the same resolution in the r-space: variations of $\phi_{v,k}$ on a length scale larger than G_{max} are correctly described. A reasonable estimate for N_{PW} is obtained by dividing the volume of the sphere of radius G_{max} by the volume of the BZ:

$$N_{PW} = \frac{E_{cut}^{3/2}}{6\pi^2} \cdot \Omega \tag{2.10}$$

This shows that N_{PW} scales linearly with the volume of the unit cell Ω, if the same resolution in the r-space is desired. Using the expression 2.8 for the Khon-Sham orbitals and Eq.2.4 the Kohn-Sham equations takes a simple secular form with diagonal kinetic term, and including the Fourier coefficients of the effective potential can be written as:

$$\sum_G \left(\frac{1}{2}(k+G)^2\delta_{GG'} + \frac{4\pi|n(G-G')|}{\Omega|G-G'|^2} + V_{XC}(G-G') + \right.$$
$$\left. + \sum_I \left(e^{-i(G-G')d_I}V_I^{loc}(G-G') + \sum_l V_{I,l}^{nonloc}(k+G,k+G')\right)\right)c_{v,k+G'} =$$
$$= \epsilon_v(k)c_{v,k+G} \tag{2.11}$$

The dimension of the matrix to be diagonalized is N_{PW} and the computing time of solving an engevalue problem is proportional to N_{PW}^3. The computational effort can be reduced exploiting the crystal symmetries: a basis set of simmetrised plane waves can be used for the orbital expansion, and this allows to break up the engevalue problem into engevalue problems of small size.

Once Eq.2.11 has been solved for a given k vector, N_{PW} bands $\epsilon_n(k)$ are found, among these only the lowest N_v are occupied, and are those used to construct the ground-state density. This is true for insulators and semiconductors, in case of metals one has to consider the energy eigenvalues for the total number of k-points and look for the Fermi-energy, i.e. the highest occupied level.

Ionic structure relaxation

Once the electronic structure for a configuration is known, one is able to calculate forces acting on atoms using the "force theorem" or Hellman-Feynman theorem [21, 22], which states that for an electronic wavefunction which is a minimum of a given ionic configuration, the only energy derivatives to be taken into account are the explicit variations of the electronic Hamiltonian upon displacement of the atom, and the ion-ion interaction.

$$F_I = -\frac{\partial E}{\partial R_I} = -\left\langle \Psi \middle| \frac{\partial \mathcal{H}}{\partial R_I} \middle| \Psi \right\rangle \tag{2.12}$$

with F_I the force acting on an ion and R_I the position of this ion. Thus the ionic structure can be relaxed with the use of a new SCF calculation for each ionic step.

2.2 Method

2.2.1 Code and HPC

Quantum-ESPRESSO

Among the various state-of-the-art codes available, we chose Quantum-ESPRESSO for our simulations ([28], see also www.quantum-espresso.org).
Quantum-ESPRESSO is an integrated suite of computer codes for electronic-structure calculations and materials modeling at the nanoscale. It is based on density-functional theory, plane waves, and pseudopotentials. It is freely available to researchers around the world under the terms of the GNU General

Public License. Quantum-ESPRESSO is an initiative of the DEMOCRITOS National Simulation Center(Trieste) and SISSA (Trieste), in collaboration with the CINECA National Supercomputing Center in Bologna, the Ecole Polytechnique Federale de Lausanne, the Universite Pierre et Marie Curie, the Princeton University, the Massachusetts Institute of Technology, and Oxford University.

The core components of QE are PWscf and CP. The former performs self- consistent calculations (including structural optimization and molecular dynamics on the Born-Oppenheimer surface) in crystals, while the latter performs Car-Parrinello Molecular Dynamics (CP-MD) in cells with Periodic Boundary Conditions. Other important and well-established components are: Phonon, a set of codes for linear-response calculations; PostProc, utilities for visualization and data postprocessing; atomic, for pseudopotential generation and testing; PWcond, for ballistic conductance calculations. More recent additions and extensions include: GIPAW, for chemical shifts and EPR factor calculations; Wannier90, Wannier-function package; XSPECTRA, calculating X-ray spectra. The main components used in this work are PWscf and PostProc.

QE is parallelized using the Message-Passing paradigm, via calls to standard MPI (Message Passing Interface) library routines. Five parallelization levels are present, allowing some form of effective execution on all kinds of parallel machines. The different levels are organized as a hierarchy of processor groups, identified by different MPI communicators. In this hierarchy, groups implementing coarser-grained parallelizations are split into groups implementing finer-grained parallelizations.

Between these different parallelization levels, we used extensively the *Pool parallelization*: implemented by further dividing each group of processors into n_{pool} pools of processors, each taking care of one or more k-points. In both cases, good scalability of CPU time (but no scalability for RAM) can be achieved with a modest amount of communication among processors. Parallelization levels as implemented in QE allow good CPU and memory scalability up to several tens of processors (the total number of MPI processes is $N = n_{image} \cdot n_{pool} \cdot n_{PW}$) for systems including several tens to hundreds atoms.

Computer time The large size of the system (up to 250 atoms, 1000 electrons, millions of plane waves) and the need of reiterated DFT calculations for the different atomic configurations have required a great computational effort and a massive use of parallel supercomputers, in terms of CPU memory, CPU time and number of processors. As far as the code is concerned, QE has been proved to offer high performance and large scalability.

All the calculations of this work were performed on the CINECA super

computers IBM-sp6 and IBM Blue Gene/P. Computer time and porting and technical assistance were provided by CINECA, both via personal contacts, since they financed the PhD grant, and via specific large scale computational projects, submitted in these years (see the closing section for a list and a resume).

2.3 Computational details

Before starting the simulations of the systems of interest, tests calculations for the bulk materials, in order to evaluate the optimal parameters at convergence to describe the properties of the compound, are required. According to the practical DFT implementation scheme presented in the previous paragraphs, one has firstly to tailor the proper pseudopotentials/plane-wave/kinetic energy cutoff, choose the number of k-points to be included in BZ summations, and select a suitable approximation for the exchange-correlation functional.

These bulk tests are performed first of all for wurtzite ZnO structure, the most complex system to be treated; afterwards the obtained parameters were used for the other structures involved in this work, i.e. Al (cubic (100) and ccp (111) cells) and hcp Zn.

2.3.1 Convergence tests

The completeness of the plane-wave basis was checked by increasing the energy cutoff until the ZnO lattice parameters undergo small variations by less than 3%. We chose 28 Ry as a compromise between computational costs and accuracy, since above this value there are no appreciable changes of the total energy. This value was used also for Al and Zn calculations.

The convergence procedure just described is pointed out in Fig. 2.4 (left panel) in the case of Aluminum for example: Concerning the BZ summations, we followed the same procedure used for the energy cutoff, varing the number of the k points of the Monkhorst-Pack [23] grid as depicted in Fig. 2.4 (right panel) in the case of Aluminum. As it can be seen in this figure a 8x8x8 MP grid is sufficient for Al system description. This is true also for Zn, while for ZnO, being a semiconductor, a smallest 4x4x4 grid allows for a proper description of the system.

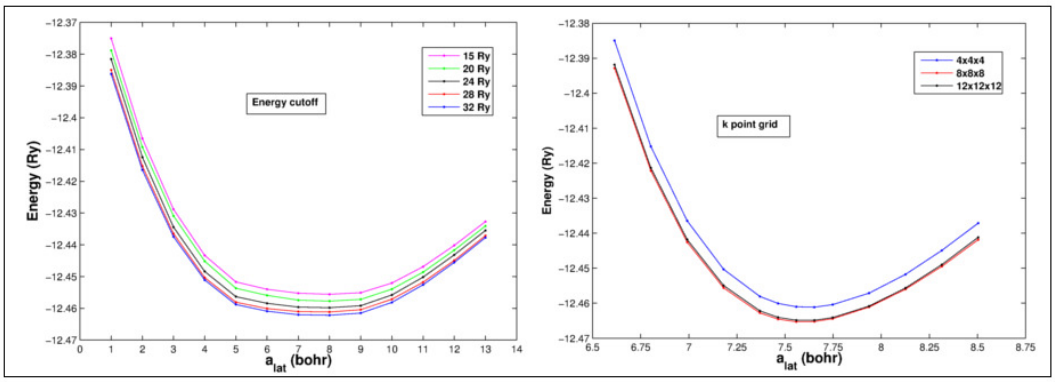

Figure 2.4: Energy cutoff convergence tests (left) and k point test (right) for Aluminum.

2.3.2 Structural properties

The equilibrium lattice parameter a_0 and the bulk modulus B_0 can be computed by evaluating the total energy for different values of the lattice parameters, and interpolating the total-energy-versus-volume curve $E(\Omega)$ with the equation of state of the solid ($E(\Omega)$ is the unit cell volume). The equilibrium lattice constant a_0 is the value that corresponds to the volume $E(\Omega_0)$ that minimizes the total energy, while the bulk modulus is related to the curvature of the energy curve at the minimum:

$$B_0 = \Omega \frac{\partial^2 E}{\partial \Omega^2}|_{\Omega=\Omega_0} \tag{2.13}$$

To find the minimum, a standard procedure is to change the volume, calculate the total energy of different volumes around the value that one expects for the system (e.g., from experimental data), and then interpolate. If the volume depends on only one lattice constant (as in simple cubic crystals), then one simply calculates the energy as a function of this lattice constant. Otherwise, an iterative procedure, that will be described later for an hexagonal crystal, is needed. Moreover, when the volume is changed, the number of plane-waves also changes if the cutoff is kept constant. There are, therefore, two conceptually different ways of plotting the curve $E(\Omega)$. In one case the number of plane-waves is kept constant; in the other case the kinetic energy cutoff is kept constant. The latter method results in a faster convergence of the lattice constant and the bulk modulus and is more physically meaningful, because a constant cutoff means a constant resolution for the wavefunctions in the real space. We used the second method. We interpolated the computed values $E(\Omega_i)$ with the Murnaghan equation [24] which

depends on three parameters: Ω_0 (the equilibrium volume of the unit cell), B_0 (the corresponding bulk modulus), B_0' (the derivative of the bulk modulus with respect to pressure):

$$E(\Omega) = \frac{\Omega_0 B_0}{B_0'}\left[\frac{1}{B_0'-1}\left(\frac{\Omega_0}{\Omega}\right)^{B_0'-1} + \frac{\Omega}{\Omega_0}\right] + const \tag{2.14}$$

In order to calculate the crystal structure of hexagonal lattices the energy minimization procedure is more complicated because we need to determine the equilibrium value of three parameters: a, c/a, u. The procedure can be cast into a four-step cycle [25]: the first three steps are tailored to determine a_0 and c/a_0 , with u parameter fixed at its theoretical value. In the fourth cycle the atoms are allowed to move in order to determine the equilibrium value u_0. Each cycle of the self-consistent optimization, which is usually stopped after one iteration, consists of the following steps: i) Fixed the value of c/a and calculate E over a set of values for a. One thus obtain, through the Murnaghan fit, the volume Ω_0 that minimizes the total energy for the ideal c; ii) Determine the energy variations as a function of c/a, to identify the equilibrium value $(c/a)_0$. This is accomplished by keeping constant the volume Ω_0 as determined in the previous step; iii) Repeat the the first step, but now choosing as fixed value for c/a its equilibrium value $(c/a)_0$ as determined in the previous step. By varying E over a set of values for a we identify the equilibrium value a_0. iiii) Fix a_0 and $(c/a)_0$ and perform a structural optimization allowing the atoms inside the cell free to move. As a result one obtains the equilibrium value u_0 and the ground state total energy E_0 of the hexagonal unit cell.

At the end of this procedure the obtained equilibrium parameters for ZnO were: a = 3.2886 Å, c/a = 1.6161 and u=0.3772. These lattice parameters are in good agreement with the experiment results [31].

2.3.3 Electronic properties

PBE

After the previous tests we started bulk simulations on the ZnO system: for this purpose we used the PWscf code that performs self-consistent calculations including structural optimization. Then, in order to investigate the electronic properties, we calculated the ZnO band structure from non-self-consistent field calculations (NSCF) based on the electronic density originating from SCF calculation and considering the k-points on the high-symmetry lines of interest as shown in Fig. 2.5 top panel.

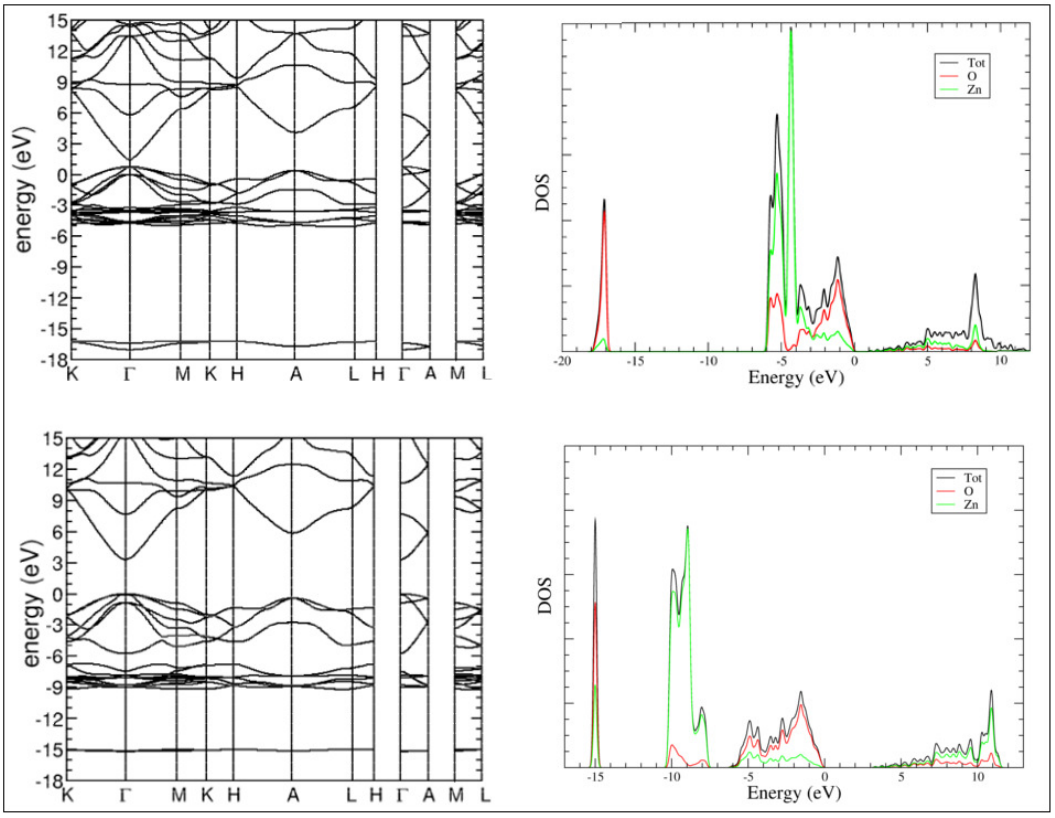

Figure 2.5: ZnO band structure along the high-symmetry lines of interest of the BZ and DOS: PBE (top) and PBE+U (bottom). As it can be seen from the comparison between top and bottom panels the U term introduction is responsible for the gap reopening and Zn 3d - O 2p bands separation.

Looking at the ZnO band structure, we find the contribution at about -18 eV arising from the Oxygen s states, while between -6 and -3 eV there are the strong d character bands originating mostly from the Zn 3d states. The next group of bands is mainly derived from O 2p orbitals; the lowest conduction bands have strong Zn 4s contributions [30]. We computed also the density of states (DOS) and the projected density of states (PDOS) using atomic wavefunction orthogonalized according to Lowdin's scheme [26], computed on the Monkhorst-Pack grid (Fig. 2.5 top panel). As it can be seen the band gap is only about 0.7 eV in contrast with the experimental one (3.3 eV). In general as it is well known, both LDA and GGA understimate the gap. Furthermore the presence of the strongly correlated Zn d orbitals complicates this scenario inducing a fictitious hybridization with states with p (O) and s (Zn) symmetry that is responsible of further lowering of the gap, and wrong

location of the d-bands.

PBE+U

In order to improve the description of Zn 3d orbitals correlation preventing the valence band top fictitious interaction and to correct the band gap the U correction was used.

The Hubbard correction was optimized via numerical fit of an on-site U_d = 12.0 eV term on Zn d-states, and a U_p = 6.0 eV on O p-states: the inclusion of the U potential on both the anion and cation appears to be fundamental for an optimized description of p-d interaction [11, 26] as discussed before. As it can be seen from Fig. 2.5 bottom panel, this choice of parameters sets the value of the Kohn-Sham gap to 3.1 eV, very close to the experimental one (3.3 eV).

We explicitly verified that the inclusion of the Hubbard correction does not change the structural and electronic properties of the compound, a part for the corrections in band edges quoted above. The small variation on lattice parameters (max 1%) is fully negligible (within the error bar of our method).

2.3.4 Planar average technique

To conclude this short summary of the methodology adopted, we discuss in the following a method to compare different calculations, for different systems, with a common energy reference.

We adopted the planar average technique in the dipole potential analysis of Chap. 4 and for the Schottky Barrier calculations of Chap. 3 and 5. The determination of the valence-band offset (Schottky barrier) across the interface between two semiconductor (metal/semiconductor), involves indeed lining up the band structures of the two materials. Hence, the band structures of the two semiconductors have to be determined with respect to some reference level. The valence band offset (Schottky barrier) is then determined by aligning the macroscopic average electrostatic potentials of the two semiconductors (Metal/semiconductor) [33,36]. For this purpose, only the variation of the electrostatic potential at self-consistency perpendicular to the interfacial plane is of interest. The dependency on the other two coordinates can be removed by averaging in planes parallel to the interface (Fig. 2.6 top panel):

$$\bar{V} = \frac{1}{S}\int_S V(x,y,z)dxdy \tag{2.15}$$

where S is the area of the unit cell in the plane of the interface. This results in a one-dimensional function that still exhibits periodic variations in the

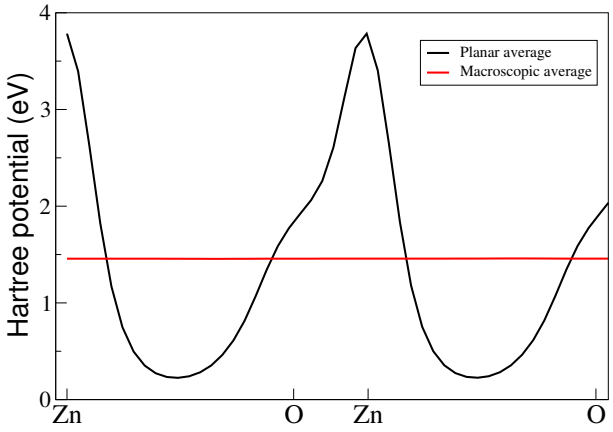

Figure 2.6: Planar (black line) averages and macroscopic (red line) averages of the Hartree potential calculated in the ZnO unit cell.

direction perpendicular to the interface. This function can be further elaborated to obtain the so called "macroscopic average", to enhance variations across the interface. The macroscopic average is found by averaging $\bar{V}(z)$ over a meaningful distance: this is usually evaluated on typical length scales of the system, e.g. one usually takes the lattice parameter in the direction perpendicular to the interface, a (Fig. 2.6 bottom panel):

$$\bar{\bar{V}} = \frac{1}{a}\int_{-a/2}^{+a/2} \bar{V}(z')dz' \tag{2.16}$$

This average offers the possibility to reduce the three dimensional potential (charge) to a one dimensional problem where potential and charge are still linked by a one dimensional Poisson equation (macroscopic average commutes with the spatial differentiation which occurs in the Poisson equation), so it preserves physical meaning. Furthermore it offers a way to compare calculations for different systems, whose energy values would be in general ill defined, via alignment of meaningful energy levels, the macroscopic average of the potential in bulk.

Bibliography

[1] Born, M., and Oppenheimer, Annalen der Physik, Volume **389**, Pages 457 - 484 389, 20 (1927), 457-484.

[2] Hohenberg, P., and Kohn, W., Phys. Rev. **136**, 864 (1964).

[3] W. Khon, and L. J. Sham, Phys. Rev **140**, A1133 (1965).

[4] E. K. U. Gross, E. Runge, and O. Heinonen *Many-Particle Theory* Adam Hilger, Bristol, 1991.

[5] E. Wigner, Phys. Rev. **46**, 1002 (1934).

[6] M. Gell-Mann, and K. A. Brueckner, Phys. Rev. **106**, 364 (1957).

[7] O. Gunnarsson, M. Jonson, and B. I. Lundqvist, Phys. Rev. B **20**, 3136 (1979)

[8] R. M. Dreizler, and E. K. U. Gross *Density functional theory: an approach to the quantum many-body problem*, Springer-Verlag, Berlin, 1990.

[9] R. O. Jones, and O. Gunnarso, Rev. Mod. Phys. **61**, 689 (1989).

[10] J. P. Perdew, K. Burke, and M. Ernzerhof, Phys. Rev. Lett **77**, 3865 (1996).

[11] S.Lany and A. Zunger, Phys. Rev. B **78**, 235104 (2008)

[12] V. I. Anisimov, F. Aryasetiawan, A. I. Lichtestein, *J. Phys.: Cond. Matt.* 9:767-808, (1997)

[13] V. I. Anisimov, J. Zaanen, O. K. Andersen, *Phys. Rev. B* **44**, 943, (1991)

[14] J. E. Jaffe and A. Zunger, Phys. Rev. B **29**, 1882 (1984)

[15] M. Cococcioni and S. de Gironcoli, Phys. Rev. B **71**, 035105 (2005)

[16] Chris G. Van de Walle and Jorg Neugebauer J. of Appl. Phys. **95**, 8, (2004)

[17] J. Hubbard, *Proc. Roy. Soc. London* 285:542, (**1965**)

[18] David Vanderbilt, Phys. Rev. B **41**, 7892-7895 (1990)

[19] N. W. Ascroft, and N. D. Mermin, *Solid state physics*, Sounders College Publishing, Philadelphia, 1976.

[20] J. C. Slater, *Quantum theory of molecules and solids Vol. II*, McGraw Hill, New York, 1965.

[21] Feynman R., Phys. Rev. 56, 340 (1939).

[22] Hellmann, H. *Einfuhrung in die Quantumchemie*. Franz Duetsche, Leipzig, 1937.

[23] H. J. Monkhorst, and J. D. Pack, Phys. Rev. B **13**, 5188 (1976).

[24] F. D. Murnaghan, Proc. Nat. Acad. Sci. U.S.A. **30**, 244 (1944).

[25] B. J. Min, C. T. Chan, and K. M. Ho, Phys. Rev. B **45**, 1159 (1992).

[26] Lowdin, P.-O. The Journal of Chemical Physics **18**, 3 (1950), 365-375.

[27] Terentjevs, A. Catellani, D. Prendergast, and G. Cicero, Phys. Rev. B **82**, 165307 (2010)

[28] Paolo Giannozzi, Stefano Baroni, Nicola Bonini, Matteo Calandra, Roberto Car, Carlo Cavazzoni, Davide Ceresoli, Guido L Chiarotti, Matteo Cococcioni, Ismaila Dabo, Andrea Dal Corso, Stefano de Gironcoli, Stefano Fabris, Guido Frates, Ralph Gebauer, Uwe Gerstmann, Christos Gougoussis, Anton Kokalj, Michele Lazzeri, Layla Martin-Samos, Nicola Marzari, Francesco Mauri, Riccardo Mazzarello, Stefano Paolini, Alfredo Pasquarello, Lorenzo Paulatto, Carlo Sbraccia, Sandro Scandolo, Gabriele Sclauzero, Ari P Seitsonen, Alexander Smogunov, Paolo Umari and Renata M Wentzcovitch, J. Phys. Condens. Matter **21**, 395502 (2009)

[29] H. Karzel et al. Phys. Rev. B **53** 11425 (1996)

[30] Pollmann et al. Phys. Rev. B **47**, 12 (1993)

[31] A. Calzolari, A. Catellani, J. Phys. Chem. C **113**, 2896 (2009)

[32] M Peressi, N Binggeli and A Baldereschi J. Phys. D: Appl. Phys. **31** (1998) 1273-1299.

[33] Baldereschi A, Baroni S and Resta R Phys. Rev. Lett. **61** 734 (1988)

[34] Richard M. Martin, *Electronic structure*, Ed. Cambridge, (**2008**)

Chapter 3

Al doped ZnO - AZO

This Chapter is devoted to the study of Al doped ZnO, usually addressed as AZO. As shortly described in the Introduction of this thesis, this compound has recently found renewed interest for applications as electrode in LED and photovoltaic cells, because it combines the transparency inherent to the wide gap host matrix of ZnO with the conductivity induced by a rather high n doping associated with Al dosages around 3%, thus behaving as a Transparent Conductive Oxide (TCO). This peculiar presence of conductivity in an albeit wide-gap material is not fully understood: Indeed, this remarkable combination of electrical and optical properties is unusual and contrasts with the standard classification between zero-gap conductive and finite-gap optical materials.

In the following, we propose the results obtained from first principles theoretical investigations of the optoelectronic properties of TCO: ab initio methods offer the possibility of a description at the microscopic level, taking directly into account the interplay between the electronic and structural properties of the system. The results are organized in three subsections.

The first part is devoted to the structural and electronic characterization of bulk ZnO: some recent experimental data have shown that it is not possible to increase doping beyond solubility limit, where a degradation of the optoelectronic properties of the compound is observed. Our simulations, presented in a paper recently published as Applied Physics Letters, and here reproduced, allowed us to define the role of interstitial defects as detrimental to both mobility and transparency.

In the second section of the chapter, we shortly summarize the results on Al diffusion, and the role of surfaces in Al adsorption. These calculations (subject of a Laurea Thesis [1]), have been presented in some international conferences, and a paper is in preparation.

Finally, we address the problem of the interface formation between ZnO and AZO.

3.1 AZO Bulk

The following article appeared in Appl. Phys. Lett. 98, 121907 (2011) and may be found at http://dx.doi.org/10.1063/1.3567513.

Optoelectronic properties of Al:ZnO: Critical dosage for an optimal transparent conductive oxide

Mirco Bazzani, Andrea Neroni, Arrigo Calzolari, and Alessandra Catellani

Citation: Appl. Phys. Lett. **98**, 121907 (2011); doi: 10.1063/1.3567513
View online: http://dx.doi.org/10.1063/1.3567513
View Table of Contents: http://apl.aip.org/resource/1/APPLAB/v98/i12
Published by the American Institute of Physics.

Optoelectronic properties of Al:ZnO: Critical dosage for an optimal transparent conductive oxide

Mirco Bazzani,[1,2] Andrea Neroni,[1,2] Arrigo Calzolari,[3,a)] and Alessandra Catellani[2,b)]
[1]*Department of Physics, University of Parma, I-43100 Parma, Italy*
[2]*CNR-IMEM Parco Area delle Scienze, 37A, I-43100 Parma, Italy*
[3]*Theory@Elettra Group, Democritos Simulation Center, CNR-IOM, Istituto Officina dei Materiali I-34012, TriesteItaly*

(Received 18 November 2010; accepted 23 February 2011; published online 22 March 2011)

We study the effects of aluminum doping on the electronic and optical properties of ZnO, via density functional simulations. We discuss the bandstructure and absorption properties of Al:ZnO as a function of the dopant concentration, and compare with recent experimental data. Our results support the formation of a transparent conductive oxide compound up to an incorporation of Al of about 3% in substitutional Zn sites. We propose an explanation to the observed degradation of conductivity in terms of interstitial defects expected to occur at high doping concentrations, beyond the Al solubility limit. © *2011 American Institute of Physics*. [doi:10.1063/1.3567513]

Doping of oxides is a complex problem:[1] several efforts have been conducted to understand and optimize doping of these materials that suffer from volatility of oxygen, accompanied by large lattice anisotropy, responsible for inhomogeneous diffusion.[2]

Because of the coexistence of high conductivity and high transparency in the visible region, the realization of transparent conductive oxides (TCOs) through doping has attracted much interest for optoelectronic device applications, such as solar cells and liquid crystal displays. Among all, it has been recently proposed that aluminum-doped zinc oxide (AZO) films can be the optimal choice as TCO layers in ZnO nanowire-based solar cells.[3–5] The optical, electrical, structural, and morphological properties of the TCO films are essential in determining device performances. Yet the remarkable combination of conductivity in an albeit wide-gap (i.e., transparent) material is not fully understood, along with the effect of dopants on charge transport: these issues contrast with the standard classification between zero-gap conductive and finite-gap optical materials and are still the subject of intense debate.[6–8] Furthermore, experimental data[9–11] have shown nonmonotonic variations in the electronic properties of AZO films increasing dopant concentration: recent transport measurements[11] have revealed an unexpected deterioration of mobility beyond the Al solubility limit ($\simeq$3%). Hence, a full understanding of the formation, stability, and solubility properties of TCOs still constitutes a fundamental challenge and a technological goal. First principles investigations offer the unique possibility of characterizing the optoelectronic properties of TCOs at an atomistic level, taking directly into account the interplay between the electronic and structural properties of the system.

In this paper we discuss the electronic and optical properties of AZO, by means of *ab initio* simulations. We first discuss how doping affects the electronic properties of AZO up to the experimental solubility limit (3%–4%),[10] presenting the details of neutral substitutional Aluminum at Zn sites in terms of density of states (DOS) and dielectric function of the doped compound. We further consider high dosages simulating clustering and interstitial defects: we suggest a possible explanation to the detrimental effect on the optoelectronic properties at high doping concentration in terms of the presence of interstitial Al defects.

We performed density functional total-energy-and-force calculations, as implemented in the QUANTUM-ESPRESSO package.[12] PBE generalized gradient approximation[13] is applied to the exchange-correlation functional. The atomic potentials are described by *ab initio* ultrasoft pseudopotentials.[14] The electronic wave functions (charge density) are expanded in a planewave basis with an energy cutoff of 28 Ry (280 Ry). AZO bulk systems are simulated by periodic supercells, multiples of the undoped ZnO lattice parameters. For Brillouin zone (BZ) integration, we use 16 special k-points in the irreducible wedge of the bulk BZ. All structures are relaxed until forces on all atoms are lower than 0.03 eV/Å.

We considered different doped systems, obtained varying the number of substitutional Al atoms, in the range [0%–3.2%], in the virtual crystal approximation. In order to simulate high dosage experimental conditions, we also performed cluster defect calculations, in the same supercell. Clustering can be simulated via substitutional Al atoms situated in next nearest neighbor position, or with inclusion of interstitial defects. To evaluate the role of clustering, we compared different model systems at the same high (3.2%) Al content.

We first focus on the results for the low dosage configurations, where Al dopants substitute Zn atoms. Upon relaxation, Al–O bonds of about 1.8 Å are formed, close to the bond length in Al_2O_3, with slight elongation of the bond along the polar axis, that tends to increase with Al content, in agreement with experiments.[15] These structural modifications remain localized around the Al site: at low dosage the presence of the defects preserves the overall tetrahedral coordination and the positions of the second neighbor Zn and O atoms are hardly affected by the Al substitution. The DOS of the doped bulk is represented in Fig. 1: doping the wide-gap oxide with substitutional Al is not associated with the inclusion of defect states in the pristine ZnO gap that remains

a)Present address: Centro S3, CNR-NANO Istituto di Nanoscience, I-41100 Modena, Italy.
b)Electronic mail: alessandra.catellani@imem.cnr.it.

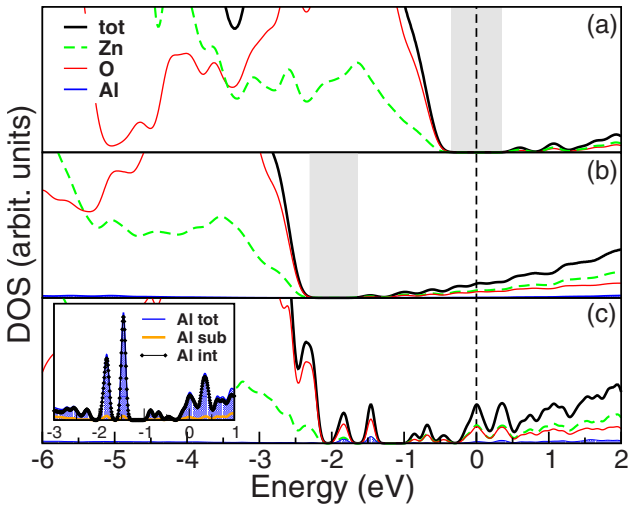

FIG. 1. (Color online) Total and projected DOSs for (a) clean bulk ZnO, (b) substitutional, and (c) interstitial AZO at 3.2% Al content. DOSs are aligned at the EF (vertical line), and normalized to the Zn 3*d* peak area. The gray areas indicate the pristine ZnO gap. Inset zooms on the Al contributions (substitutional and interstitial) around the gap.

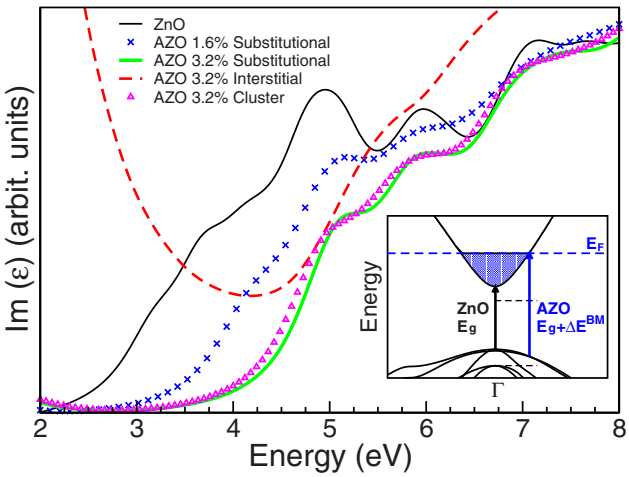

FIG. 2. (Color online) Imaginary part of the dielectric function at varying Al content. Inset: schematic bandstructure representation of the BM effect and the optical gap enhancement.

almost unchanged. Indeed, apart from low energy contributions (<−7.5 eV), Al electrons are fully donated to the system as additional free charge: the effect is reflected in a mere shift of the Fermi level (EF) up in the conduction bands. See Ref. 16 for the dependence of EF on Al content. AZO appears like a strongly doped wide-gap semiconductor, where the original characteristics of bulk ZnO are maintained. These results are in agreement with previous studies at partial Al contents.[7,17]

In order to describe the optical response of the films, we have calculated the imaginary part of the dielectric function $Im[\epsilon(\omega)]$ (i.e., absorption spectrum) in the framework of band theory, without the electron-hole interaction.[18,19] In this case, calculations are performed employing norm conserving PBE pseudopotentials, and an *ad hoc Hubbard* potential to correct the bandgap.[8,20–22]

The $Im[\epsilon(\omega)]$ spectrum is displayed in Fig. 2 for different Al contents: we observe a strong blueshift ($\simeq$1.5–2.0 eV) of the absorption edge for substitutional AZO. Other features are, however, relevant to note: (i) smaller Al contents correspond to smaller onset shifts; (ii) the overall spectral features are maintained, no peaks associated to Al are visible; (iii) going from ZnO to AZO, part of the optical anisotropy is removed, as reflected by comparing the dielectric function components in the directions parallel and perpendicular to the polar ZnO axis (see Ref. 16); (iv) there is a non negligible diffusive background at smaller energies (0–2.5 eV), that is linked to low intensity transitions toward the partially occupied conduction band minimum (CBM). In agreement with experimental findings,[23] these results confirm the role of Al doping, while preserving ZnO transparency to light in the visible range.

The observed blueshift can be explained in terms of the Burnstein–Moss (BM) effect,[24] that predicts a widening of the optical gap caused by blocking the lowest-energy transitions (see inset of Fig. 2). In clean ZnO the absorption edge is mainly due to the direct highest occupied molecular orbital (HOMO)-lowest unoccupied molecular orbital (LUMO) transition at Γ. Since the CBM of ZnO is almost parabolic with a small DOS, even a low Al dosage induces the filling of the pristine LUMO state at Γ, which is no more available for electronic transitions. Thus, the next available direct transition is shifted at higher energies and different k-points. The BM correction to ZnO E_g gap may be estimated within the effective mass approximation: in the case of AZO 3.2% (substitutional) we obtain $\Delta E^{\mathrm{BM}} \simeq 1.4$ eV, in very good agreement with the dielectric function results of Fig. 2. The coexistence of direct band gap, and almost parabolic conduction bands are prerequisite for good TCOs: this marks a fundamental difference with e.g., TiO_2, which is also considered for applications similar to ZnO, but it does not show TCO behavior, having CBM with high DOS.

On the basis of these results, it could seem that the performances of AZO as TCO can be incessantly improved simply increasing the Al dosage, since this would be reflected in a higher number of free light carriers available for transport. This is, however, in contradiction with recent experiments that evidence a remarkable worsening in the transport properties of AZO films beyond an Al content, corresponding to the solubility limit.[11]

To provide an explanation for this nonlinear behavior, we took into account the effects of interacting Al defects when they assume a pure substitutional (cluster) or a mixed substitutional and interstitial configuration. Indeed, it has been proposed that interstitial Al defects may appear when the solubility limit ($\simeq$3%) is overcome.[10] As long as Al occupies only substitutional sites the overall picture described above does not change. On the contrary, the simulation of interstitial defects shows completely different characteristics and marks a discontinuity in the behavior of the doped compound: additional localized filled states appear in the pristine ZnO gap, pushed down from conduction bands of the clean ZnO. These states tend to increase in number with increasing doping and have strong Al and O components [Fig. 1(c)]. They are almost dispersionless, being described by nearly flat bands, i.e., large effective masses and low electron mobility, in contrast with the substitutional configuration. The presence of localized gap states, which act as traps for the optical transitions, is responsible for a deep modification of the dielectric function (dashed line, Fig. 2), since they allow for light absorption in the visible range (i.e., the compound is no more transparent). They are thus associated with vanishing of TCO behavior. These findings can be ascribed to struc-

tural modifications of the crystal: in proximity of Al ions, Zn atoms are also kicked-off in interstitial positions, leaving the neighbor O atoms undercoordinated. Notably, Al–O and Zn–Al bonds are formed instead of Al–Al ones. This structural modification—linked to undercoordinated oxygen atoms rather than to Al–Al interaction—is responsible for degradation of optical and transport properties observed in the experiments at high Al dosage.[11]

In conclusion, our calculations allow us to discriminate two distinct optoelectronic regimes in Al:ZnO, depending on the Al concentration, providing a comprehensive explanation of controversial experimental results. In particular, we highlighted the role of interstitial Al defects on the degradation of the optoelectronic properties of AZO: our results suggest an optimal TCO behavior for AZO under 3%–4% of Al content.

We thank Piero Torelli for sharing unpublished results and Fondazione Cassa di Risparmio di Trento e Rovereto for financial support (DAFNE). Computer time was provided by CINECA through and ISCRA project-AID. M.B. acknowledges CINECA for the PhD grant.

[1]J. A. van Vechten, in *Handbook of Semiconductors*, edited by S. P. Keller (North-Holland, Amsterdam, 1980).
[2]J. Simon, V. Protasenko, C. Lian, H. Xing, and D. Jena, Science **327**, 60 (2010).
[3]H. Porter, C. Mion, A. Cai, X. Zhang, and J. Muth, Mater. Sci. Eng., B **119**, 210 (2005).
[4]M. N. E. M. S. Tricot, C. Boulmer-Leborgne, and J. Perrière, J. Phys. D: Appl. Phys. **41**, 175205 (2008).
[5]S.-H. Lee, S.-H. Han, H. S. Jung, H. Shin, J. Lee, J.-H. Noh, S. Lee, I.-S. Cho, J.-K. Lee, J. Kim, and H. Shin, J. Phys. Chem. C **114**, 7185 (2010).
[6]P. Ágoston, K. Albe, R. M. Nieminen, and M. J. Puska, Phys. Rev. Lett. **103**, 245501 (2009).
[7]S. Lany and A. Zunger, Phys. Rev. B **78**, 235104 (2008).
[8]A. Janotti, D. Segev, and C. G. Van de Walle, Phys. Rev. B **74**, 045202 (2006).
[9]K.-M. Lin, Y.-Y. Chen, and K.-Y. Chou, J. Sol-Gel Sci. Technol. **49**, 238 (2009).
[10]P. Torelli, private communication (September 2010).
[11]H. Mondragón-Suárez, A. Maldonado, M. de La, L. Olvera, A. Reyes, R. Castanedo-Pérez, G. Torres-Delgrado, and R. Asomoza, Appl. Surf. Sci. **193**, 52 (2002).
[12]P. Giannozzi, S. Baroni, N. Bonini, M. Calandra, R. Car, C. Cavazzoni, D. Ceresoli, G. L. Chiarotti, M. Cococcioni, I. Dabo, A. D. Corso, S. de Gironcoli, S. Fabris, G. Fratesi, R. Gebauer, U. Gerstmann, C. Gougoussis, A. Kokalj, M. Lazzeri, L. Martin-Samos, N. Marzari, F. Mauri, R. Mazzarello, S. Paolini, A. Pasquarello, L. Paulatto, C. Sbraccia, S. Scandolo, G. Sclauzero, A. P. Seitsonen, A. Smogunov, P. Umari, and R. M. Wentzcovitche, J. Phys.: Condens. Matter **21**, 395502 (2009) (see also www.quantum-espresso.org).
[13]J. P. Perdew, K. Burke, and M. Ernzerhof, Phys. Rev. Lett. **77**, 3865 (1996).
[14]D. Vanderbilt, Phys. Rev. B **41**, 7892 (1990).
[15]J. U. Brehm, M. Winterer, and H. Hahn, J. Appl. Phys. **100**, 064311 (2006).
[16]See supplementary material at http://dx.doi.org/10.1063/1.3567513 for detailed information about the dependence of EF position as a function of Al content, and optical anisotropy.
[17]P. Palacios, K. Sánchez, and P. Wahnón, Thin Solid Films **517**, 2448 (2009).
[18]R. Colle, P. Parruccini, A. Benassi, and C. Cavazzoni, J. Phys. Chem. B **111**, 2800 (2007).
[19]The size of the system prevents the application of many body techniques such as configuration interaction or GW-Bethe Salpether, while simulation of infinite systems does not allow the application of time dependent density functional theory. The complete simulation of the absorption spectra goes beyond the aim of this work.
[20]Y. Dong and L. Brillson, J. Electron. Mater. **37**, 743 (2008).
[21]We optimized the Hubbard correction via numerical fit of an on-site $U_d = 12.0$ eV term on Zn d-states, and a $U_p = 6.0$ eV on O p-states: the inclusion of the U potential on both the anion and cation appears to be fundamental for an optimized description of $p-d$ interaction (Ref. 22). This sets the value of the Kohn–Sham gap to 3.1 eV, very close to the experimental one (3.3 eV). The inclusion of Hubbard correction does not change the structural and electronic properties of the doped compound.
[22]A. Terentjevs, A. Catellani, D. Prendergast, and G. Cicero, Phys. Rev. B **82**, 165307 (2010).
[23]T. Ohgaki, Y. Kawamura, T. Kuroda, N. Ohashi, Y. Adachi, T. Tsurumi, and F. M. H. Haneda, Key Eng. Mater. **248**, 91 (2003).
[24]T. S. Moss, Proc. Phys. Soc. **67**, 775 (1954).

Supplemental Information for: Optoelectronic properties of Al:ZnO: critical dosage for an optimal transparent conductive oxide

Mirco Bazzani[1,2], *Andrea Neroni*[1,2], *Arrigo Calzolari*[3], *and Alessandra Catellani*[*,1]

[1] CNR-IMEM, Parco Area delle Scienze, I-43100 Parma, Italy

[2] Dipartimento di Fisica, Università di Parma, I-43100 Modena, Italy

[3] Theory@Elettra Group, Democritos Simulation Center, CNR-IOM Istituto Officina dei Materiali, I-34012 Trieste, Italy

*Corresponding Author Footnote:

Alessandra Catellani, Phone: +39-0521-269200. Fax: +39-0521-269206, e-mail: alessandra.catellani@imem.cnr.it.

S1. Electronic Properties of AZO: Fermi Level

As discussed in the main text, doping zinc-oxide with substitutional Al is not associated with additional states in the pristine ZnO gap that remains almost unchanged. Indeed, apart from low energy contributions (< -7.5 eV), Al electrons are fully donated to the system as additional free charge (see Fig. SI-1). The effect is reflected in a mere shift of the Fermi level (EF) up in the conduction bands. This allows to describe in a pictorial way the dependence of EF position as a function of Al content on top of the band structure of clean, undoped ZnO, as depicted in Fig. SI-2.

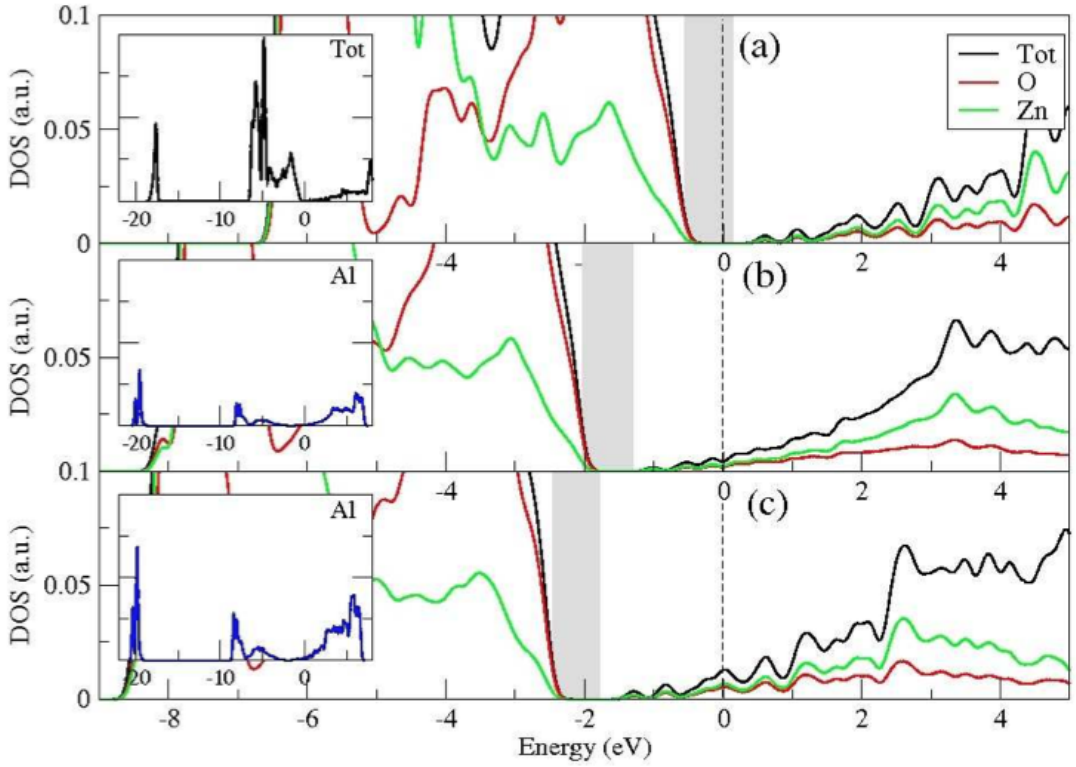

Figure SI-1. From Top to Bottom, the three panels represent the DOS for clean buk ZnO (a), for AZO at 1.6% Al content (b), and at 3.2% Al content (c). DOS are aligned at the Fermi level of the system, taken as zero of the energy scale, and normalized to the Zn_{3d} peak area. The grey areas indicate the pristine ZnO gap, while the dashed line is the position of the Fermi level. Panels help identification of Al contribution to the total DOS. (Results from PBE calculations).

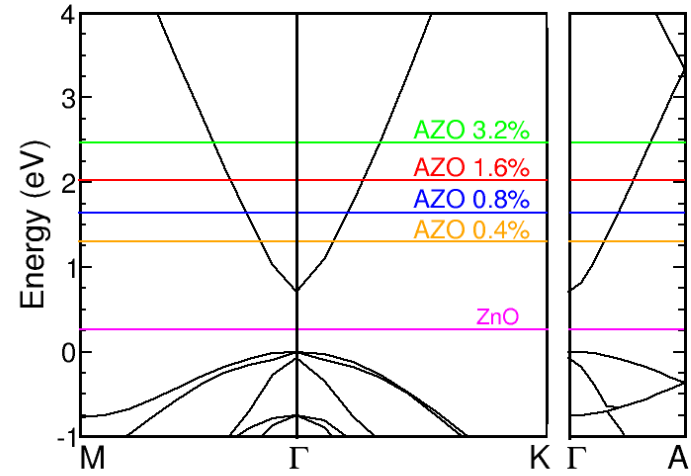

(a)

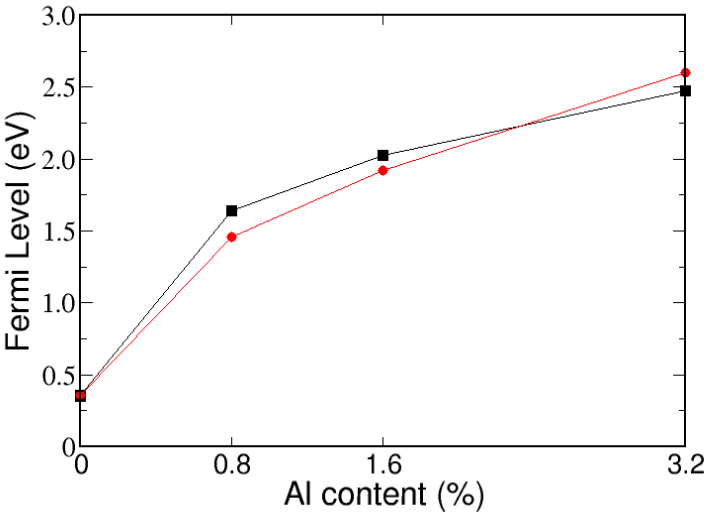

(b)

Figure SI-2. (a) Fermi level alignment corresponding to different Al dosages, with respect to the ZnO bulk band structure. In (b) we compare the SCF results explicitly displayed as a function of the Al content with the parabolic approximation $E_F \propto n^{2/3}$ used to evaluate the Burstein-Moss contribution to optical transition. (Results from PBE calculations).

S2. Optical Properties of AZO

The imaginary component of the dielectric function Im[ε(ω)] (*i.e.* absorption spectrum), calculated in the framework of band theory, without the electron-hole interaction [S1, S2] and employing norm conserving PBE pseudopotentials, with an *ad hoc Hubbard potential* to correct the bandgap [S3-S5], reveals that, going from ZnO to AZO, part of the optical anisotropy is removed. The comparison of the dielectric function components in the directions parallel and perpendicular to the polar ZnO axis depicted in Fig. SI-3 for *e.g.* 1.6% Al content clearly reveals the effect.

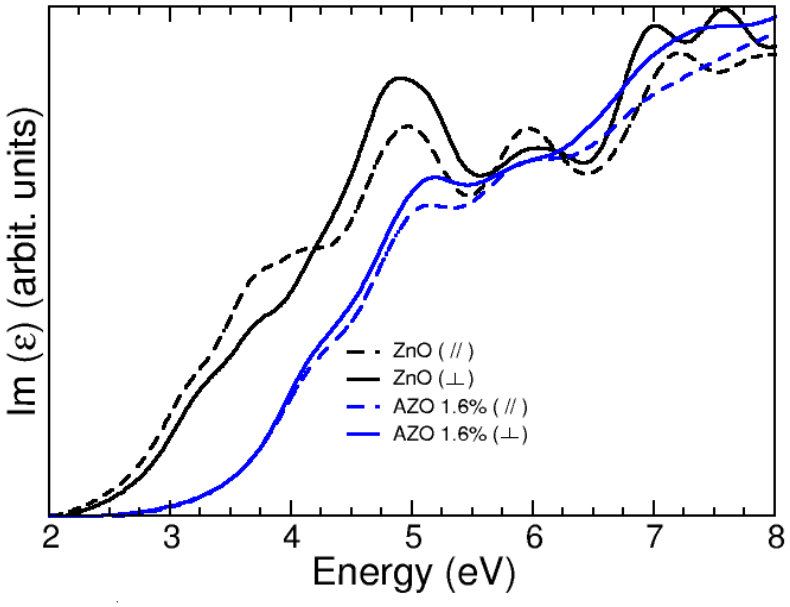

Figure SI-3. Imaginary part of the dielectric function for clean and Al doped ZnO. We indicate with different lines the parallel (continuous) and perpendicular (dotted) components of Im[ε(ω)], with respect to the polar axis.

References

[S1] R. Colle, P. Parruccini, A. Benassi, and C. Cavazzoni, *J. Phys. Chem.B* **111** 2800 (2007).

[S2] The size of the system prevents the application of many-body techniques such as CI or GW-BSE, while simulation of infinite systems does not allow the application of TDDFT. The complete simulation of the absorption spectra goes beyond the aim of this work.

[S3] A. Janotti, D. Segev, and C.G. Van de Walle, *Phys. Rev. B* **74**, 045202 (2006).

[S4] Y. Dong and L.Brillson, *J. Electronic Mater.* **37**, 743 (2008).

[S5] We optimized the Hubbard correction via numerical fit to the experimental energy band position.s obtaining an on-site U_d=12.0 eV term on Zn *d*-states, and a U_p=6.0 eV on O *p*-states: the inclusion of the U potential on both the anion and cation appears to be fundamental for an optimized description of *p-d* interaction [S6]. This sets the value of the Kohn-Sham gap to 3.1 eV, very close to the experimental one (3.3 eV). The inclusion of Hubbard correction does not change the structural and electronic properties of the doped compound.

[S6] A.Terentjevs, A. Catellani, D. Prendergast, and G. Cicero, *Phys. Rev. B* **82**, 165307 (2010).

3.2 Al diffusion

In order to fully understand the role of Al impurities in ZnO, and evaluate non uniformities in dopant incorporation, as induced by the spontaneous polarization field typical of the wurtzite lattice, a description of the diffusion mechanisms and energy barriers experienced by Al adatoms in the lattice bulk would be fundamental. Probing in particular the site stability and paths along the three inequivalent low index directions (the polar axis, and the two non-polar axes normal to most common nanostructure faces) of an Al in bulk and at surfaces, would allow to obtain a precise evaluation of the diffusion processes.

As a first effort in this direction, we have performed a series of ab initio calculations of the role of surfaces on the stability of substitutional Al ions in the ZnO matrix. We have chosen to study first the non-polar surfaces, as nanostructures usually present nonpolar lateral facets [1].

With the same frame described for AZO bulk, namely DFT-PBE total-energy-and-force calculations, with the same number of plane waves and commensurate k-point mesh, to maintain consistency between different simulations, we have studied the role of non-polar $(10\bar{1}0)$ surfaces in a supercell approach (see Fig. 3.1). All atoms are allowed to move, until forces are below 0.03 eV/Å.

For clean ZnO, the presence of the surfaces induces an atomic relaxation of the first and underlaying layers, to optimize charge transfer induced by the dangling bonds, and no surface state is found in the band gap, in agreement with previous results (see [2] and refs therein).

We have then substituted one Zn atom with Al, in different layers, at increasing distances from the surface, evaluating the total energies of the different systems thus obtained. This allows to compare the stability of the defect as a function of the depth in bulk ZnO, thus allowing for a first diffusion model, within standard rate equations.

In order to compare the different stabilities, we have evaluated the formation energies in terms of the chemical potentials of the compounds [3, 4]:

$$\Delta H_D = [E_{Def} - E_{Host}] + qE_F + \sum \pm (\mu + \delta\mu) \tag{3.1}$$

where ΔH_D is the formation enthalpy, E_{Def} the self-consistent total energy of the defected system, E_{Host} the self-consistent total energy of the ZnO matrix without defects, q the impurity charge state (q=1 for Al), E_F the Fermi energy of the system in presence of the defect and μ the chemical potential of each atomic species (see Tab. 3.1 for the calculated chemical potentials). By varying the chemical potential of $\delta\mu$ we are able to simulate

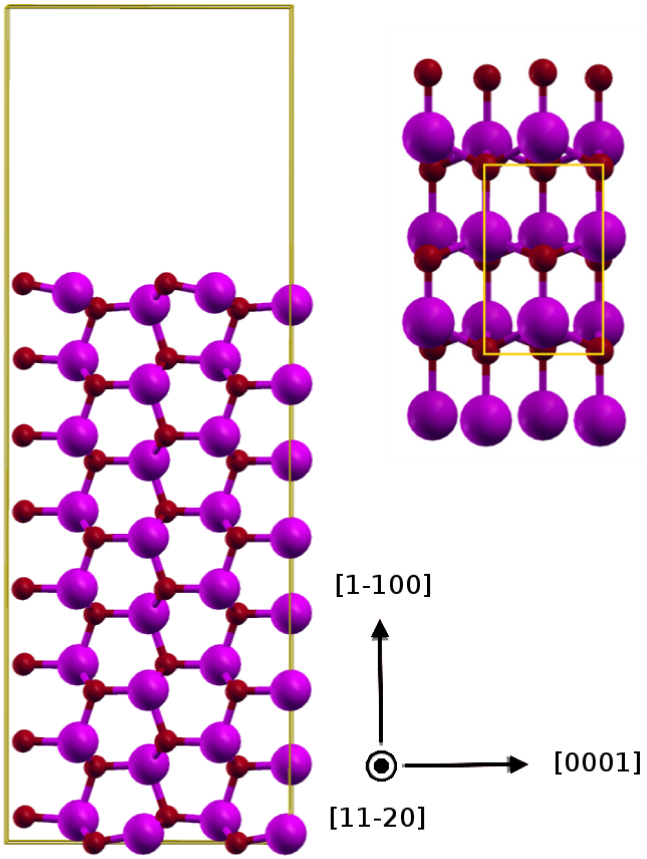

Figure 3.1: Side (Left) and Top (Right) view of the 8 Zn- O bilayer supercell with 2×2 lateral periodicity (yellow rectangle) used. Zn (O) atoms are indicated by pink (red) spheres. The overall height of the supercell is 31.2 Å i.e. the sum of the slab (20.6 Å) and the vacuum regions (10.6 Å).

the different growing conditions (in particular the two extremes O-rich and Zn-rich conditions).

From these energies it is possible to estimate the defect concentration created at the surface as a function of the substitution depth using the Arrhenius law:

$$n = Ce^{-\frac{\Delta H_D}{k_B T}} \tag{3.2}$$

where C is a normalization constant for the number of surface defects and T is set to a typical experimental growth value. These results are shown in Fig. 3.2: as it can be seen we obtain a clear tendency for Al to stay preferably in bulk sites, far from the surface, at variance with the experimental and theoretical evaluation for different compound semiconductors (e.g AlGaAs).

	Chemical potential μ (Ry)
Zn	-126.577
O	-31.892
ZnO	-158.722
Al	-12.465

Table 3.1: Chemical potential for each atomic species, obtained from bulk calculations. These values are used for the defect energy formation calculation.

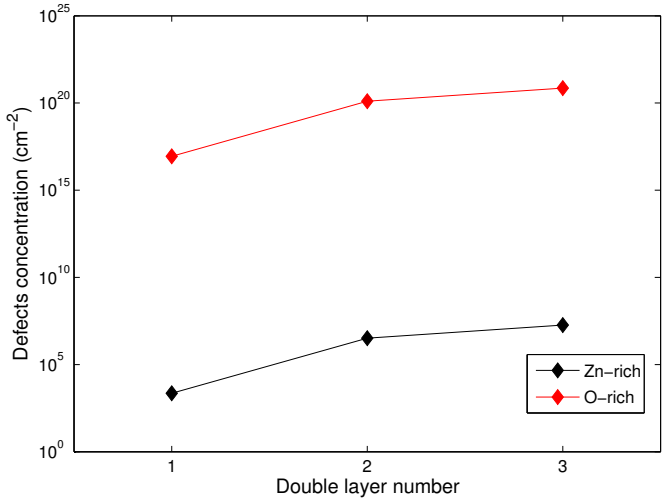

Figure 3.2: Substitutional defect concentration in Zn-rich (black) and O-rich (red) conditions as a function of the substitution depht.

3.3 ZnO/AZO interface

After providing a complete characterization of the AZO opto-elctronic properties and a preliminary investigation of the doping mechanism as well as a description of Al diffusion, we focused on the AZO/ZnO interface. This is indeed the relevant interface that controls electron transport in innovative solar cell design. Although preliminary experimental results on this interface have been recently achieved, it is not at all clear whether the electric contact at the interface is of Schottky or Ohmic type, nor if there is undesired diffusion of Al into ZnO.

For this purpose we performed an ab initio simulation of the AZO/ZnO interface in the same frame described for AZO bulk calculations to maintain consistency. In particular the interface system is composed by an AZO (1.6%)

supercell (with the same characteristics of those described in Par. 3.1) interfaced with an equivalent undoped ZnO supercell (see Fig. 3.3). The contact between the two materials is carried out along the polar direction, since this is the direction of the NWs experimental growth. The system thus obtained was very demanding from a computational point of view since it is composed by 256 atoms and so more than a thousand electrons.

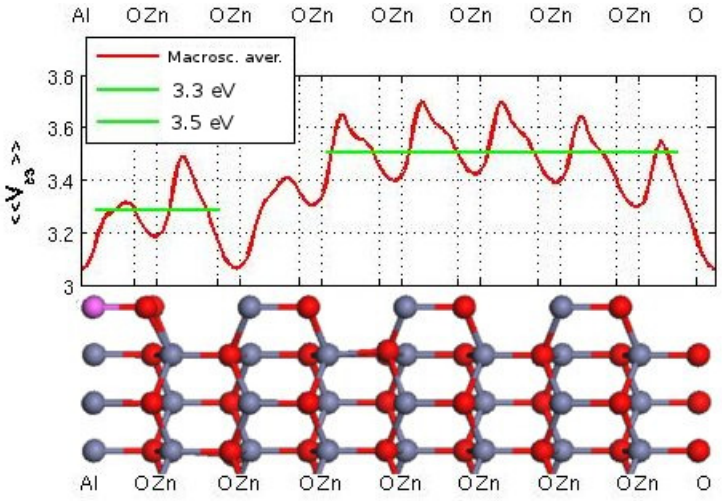

Figure 3.3: Macroscopic average potential of the AZO/ZnO interface along the polar direction (top panel) and the supercell system oriented in the same direction of the potential (bottom panel). Zn (O) atoms are indicated with gray (red) spheres, while Al atoms are shown as pink spheres.

We adopted planar average technique for determining the valence band offset across the interface between AZO and ZnO as described in Chap. 2. As it can be seen in the top panel of Fig. 3.3, where the potential trend across the supercell is shown, the valence band offset at the interface is about 0.2 eV. Thus we found an Ohmic behaviour for the AZO/ZnO interface in agreement with experimental indications [5]. This is a desirable property of the contact, to minimize losses.

It must be noted however that the simulated AZO/ZnO interface corresponds also to a lower (1/2) density alloy, by construction as can be seen by inspection of the lower panel of Fig. 3.3. Thus ohmicity, as calculated, is a trivial result.

3.4 Conclusions

In this chapter the main results of the ab initio DFT investigation performed on AZO system were summarized. Our analysis of the structural, electronic and optical properties allow us to discriminate two distinct optoelectronic regimes in AZO, depending on the Al concentration, providing a comprehensive explanation of controversial experimental results. In particular, we highlighted the role of interstitial Al defects on the degradation of the optoelectronic properties of AZO: our results suggest an optimal TCO behavior for AZO under 3-4% of Al content.

The preliminary description of the diffusion mechanisms and energy barriers experienced by Al adatoms in the lattice and the analysis of AZO/ZnO interface complete the study, offering relevant indications to complement the experimental data on the subject.

Bibliography

[1] Andrea Neroni, Laurea Specialistica in Scienze dei Materiali, Physics Department, University of Parma, December 2009

[2] A. Calzolari, A. Catellani, J. Phys. Chem. C **113**, 2896 (2009)

[3] Chris G. Van de Walle and Jorg Neugebauer J. Appl. Phys., **95**, 8 (2004)

[4] A. F. Kohan, G. Ceder, and D. Morgan and Chris G. Van de Walle Phys. Rev. B, **61**, 22 (2000)

[5] Sung-Hae Lee et al., J. Phys. Chem. C **114**, 7185-7189, 2010,

Chapter 4

ZnO polar surfaces

4.1 Introduction

Solid compounds, built by stacking (partially) charged atomic layers, may expose polar surfaces . This is particularly true in the case of materials that crystallize in low symmetry structures, compatible with a macroscopic polarization [1–5] (built in of a spontaneous finite macroscopic dipole), such as the wurtzite lattice, which is the stable crystal structure of ZnO [6,7]. In this case, upon direct truncation of the crystal along the polar axis, namely the stacking direction of the alternating tetrahedrally coordinated O^{2-} and Zn^{2+} ions, the obtained surface is polar and unstable due to the diverging electrostatic energy [8,9]. The surface must therefore be energetically compensated by adopting a modified or reconstructed surface structure.

Zinc Oxide is indeed the prototypical material of this kind: when the wurtzite ZnO crystal (Fig. 4.2) is sliced perpendicular to the (0001)-axis, two different polar surfaces that are both exposed in natural crystals, termed the Zn-terminated ZnO(0001) and the O-terminated ZnO(000$\bar{1}$) surface, are formed (Fig. 4.2). From simple electrostatic considerations one could predict that the removal of a quarter of the surface ions (O^{2-} for ZnO(000$\bar{1}$) and Zn^{2+} for ZnO(0001)) would nullify the resulting dipole and lead to stable nonpolar surfaces. However, the exact structure of both ZnO(0001)-type surfaces and the implications for surface stability are still being debated intensively [10–21], notwithstanding the wide attention that has been focused on the polar ZnO surfaces both for their experimental interest, since for instance most of ZnO nanostructures are grown or dominated by polar surfaces, and from the theoretical point of view. Several stabilization mechanisms that allow for dipole compensation can take place, with increasing reconstruction size: the simplest situation can occur via modification of surface charges by partial filling of electronic surface states, between different edge states at opposite surfaces (Highest Occupied states localized at the ZnO(000$\bar{1}$) and

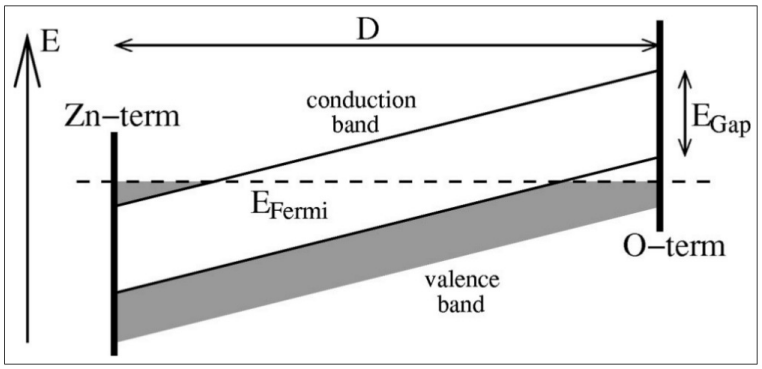

Figure 4.1: Schematic illustration of the band structure after electrons have moved from the O- to the Zn-terminated surface of the slab. Depending on the band gap and the thickness D of the slab, a residual electric field remains inside the slab. From [12].

Lowest Unoccupied states localized instead at the ZnO(0001)), leading to a sort of Fermi level pinning, a mechanism often addressed to *surface metallicity* (see [12] and Fig. 4.1). Different structures may be however obtained also via modification of the surface composition, via e.g. surface defect formation (vacancies) or adsorption of charged foreign species (e.g. H atoms or OH groups). Most recently, for the Zn-terminated (0001) surface, results from scanning tunnelling microscopy (STM) [11, 13] in combination with density functional theory [14] allowed to propose a large surface reconstruction where the surface is stabilized by the spontaneous formation of a high concentration of Zn-deficient triangular pits and step edges terminated by under-coordinated O atoms. This triangle-based mechanism of compensation should stabilize the surface over a large range of oxygen and hydrogen chemical potentials. Under more H-rich conditions, instead, the stable surface configuration involves OH groups absorption with 1/2 monolayer coverage, whereas He-TDS experiments show OH(1x1) reconstruction in the same conditions.

Because of the different affinities of Zn and O, the situation for the O-ZnO termination is more complicated. This surface is very reactive, so that it can be observed only during a limited time. HAS experiments, under UHV conditions, showed (1x1) hydrogen-covered surfaces; when the H atoms are removed, the surface reconstructs with a (1x3) unit cell [10] appears. Thermodynamic ab initio simulations [15] show that for a wide range of temperatures and pressures, the most stable surface structure presents 1/2 monolayer H coverage. At high temperatures and low H partial pressures instead, a structure with 1/4 surface oxygen atoms missing becomes the most stable one.

Both configurations are electrostatically compensated. Also the clean stoichiometric surface can exist, but only at high oxygen and very low H partial pressures.

The most common theoretical solutions described above, treat the problem of polar surfaces mainly from the thermodynamic point of view. Generally, a perfect agreement between theory and experiment must still be achieved, since, especially for highly reactive unstable surfaces, the particular reconstruction observed by a given experimental technique depends on growth ambient and preparation condition of the sample. Furthermore, in a real piece of material, and most importantly in nano-structures, any sort of surface charge compensation occurring at one side would be driven entirely by electrostatics, thus one should expect a similar rearrangement and charge redistribution on the opposite surface, accompanied by a quenching of the macroscopic field, which is not observed experimentally [16]. The most common theoretical solutions proposed for the stabilization of the polar ZnO surfaces beyond charge transfer and *surface metallization* are based on thermodynamic considerations [13, 14]. A comprehensive understanding of the different mechanisms and their suitability to describe realistic experimental situations along with a detailed description of the electronic properties of the ZnO(0001) surfaces is still lacking.

In order to obtain a reasonable starting point for successive simulations of the metal/ZnO interface, but also in view of the existing controversy between theoretical and experimental data, we have performed a series of *ab initio* simulations, comparing different possible surface terminations. Since there exists a stoichiometry equivalence between triangles and vacancies, we selected the latter solution because it is less expensive from a numerical point of view. Indeed it can be demonstrated that a triangular pit with side length n possesses the same number of dangling bonds of n isolated vacancies and the same ionic contribution. This equivalence is confirmed also from the structural analysis that shows the same interlayer distance trend within the slab [14]. Vacancies are therefore a good model system to characterize the stabilization issues of the Zn-terminated surface, albeit offering a reasonable compromise in terms of computational effort. Since from the experimental point of view the situation is more complicated for the O-$(000\bar{1})$ surface (the smaller experimentally observed O(1x3) and H(1x1) reconstructions do not respect the charge compensation rule), we adopted vacancies also for this surface. We further considered also the effect of adatoms, such as H, or OH, on the different terminations, being dissociative adsorption of water one of the possible surface stabilization mechanisms [10, 36]. The adopted methodology and the main results are described in what follows.

4.2 Method

From the computational point of view, studying electric fields within a periodic boundary condition approach is an ill defined problem. The oppositely charged ions at the two surfaces in the slab produce positively charged Zn-(0001) and negatively charged O-(000$\bar{1}$) surfaces, resulting in an asymmetric slab with a non vanishing normal dipole moment: thus the electrostatic potential on the two sides of the slab would be different at the cell boundaries, which is impossible if periodic boundary conditions have to hold, so an artificial uniform field is built in the cell, to cancel the potential discontinuity at the cell boundaries as depicted in Fig. 4.3.

Similarly to the other calculations presented in this work, we performed density functional total-energy-and-force calculations, as implemented in the Quantum-ESPRESSO package [32]. PBE generalized gradient approximation [33] is applied to the exchange-correlation functional and an ad hoc Hubbard potential to correct the bandgap, as already discussed for the simulation of optical properties in AZO [25]. The atomic potentials are described by ab initio ultrasoft pseudopotentials [34]. The electronic wave functions (charge density) are expanded in a planewave basis with an energy cutoff of 28 Ry (280 Ry). A 4 x 4 x 1 Monkhorst-Pack mesh is used for the Brillouin zone integration.

We have thus considered different slab sizes in a periodic supercell approach containing up to twelve (0001) bilayers and a vacuum thickness of 18 Å are considered in order to compare different stabilization mechanisms and study slab size effects on the dipole field. Clean surfaces and external compensation field simulations were performed in 1x1xN supercells (N=3,4,6), whereas vacancies and adsorbates reconstructions are studied in 2x2xN supercells, the smallest cells suitable to respect the empirical charge rule $R_1/(R_1 + R_2) \sim 1/4$[1]. All atoms in the supercell were allowed to relax. The structural optimization is terminated when the magnitude of the Hellmann-Feynman forces on each ion is less than 0.03 eV/Å.

In summary, the stabilization configurations studied in this work are (see Fig. 4.2): i) clean Zn/O-terminated surfaces, ii) Zn and O vacancies at the Zn/O-terminated surfaces (a surface vacancy every four Zn in the (0001) and every four O in the (000-1) surfaces, i.e. 1/4 ML, according to the empirical charge rule was introduced), iii) OH group absorption on the Zn-terminated surface (1/2 ML) and O vacancy on O-terminated surface and iiii) OH groups at the Zn-terminated surface and H absorption at the O-terminated surface. For the latter, since the O-(000$\bar{1}$) surface shows a natural affinity for H atoms

[1] R_1 and R_2 are respectively the inter and intra Zn-O bilayer distance.

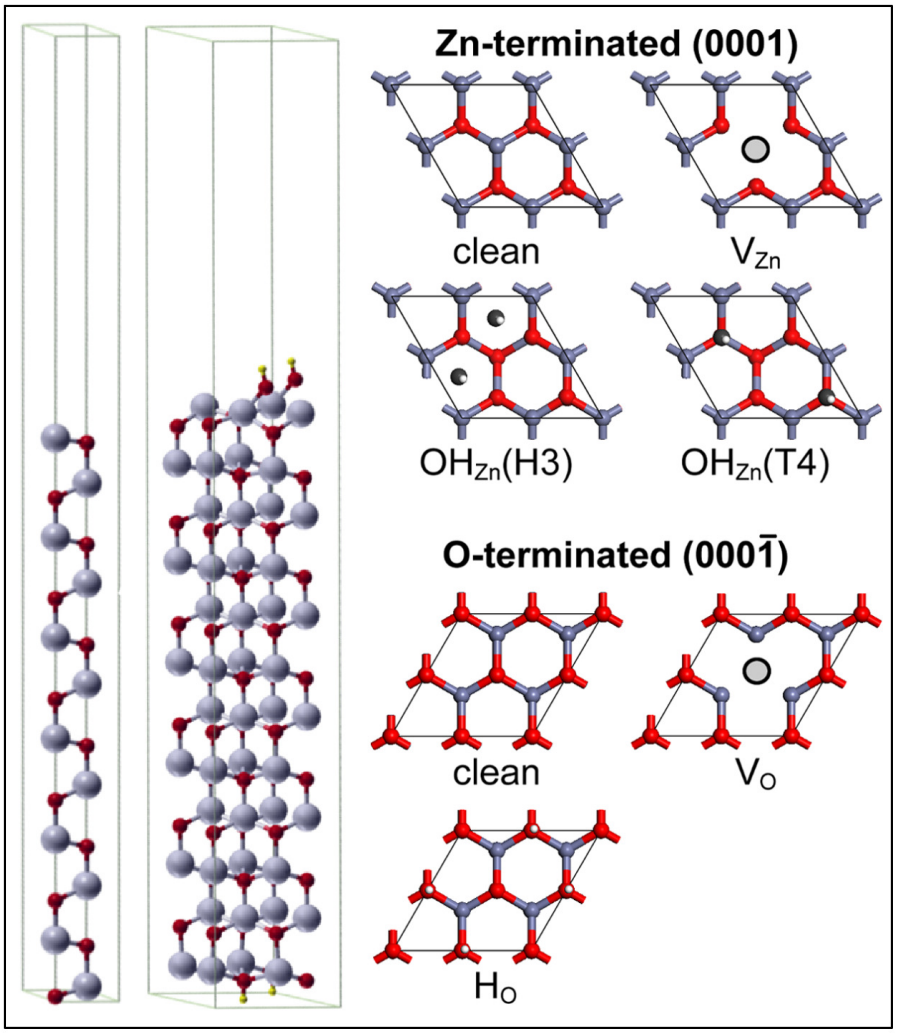

Figure 4.2: Left panel: the two different supercell, 1x1 and 2x2, used for calculations. Right panel: the different surface reconstructions adopted for 2x2 supercell: vacancies and OH groups absorption for Zn-(0001) (top panel); vacancies and H atoms introduction for O-(000$\bar{1}$) (bottom panel). Vacancies are evidenced by a black circle, while red (grey) spheres indicate O (Zn) atoms, small bright grey spheres indicate H atoms.

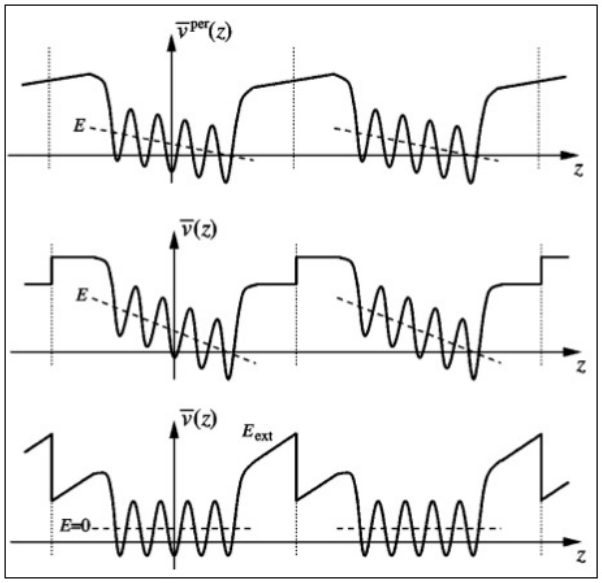

Figure 4.3: Schematic picture of the planar-averaged potential for periodically repeated slabs: a) with periodic boundary conditions, b) dipole-corrected slabs with vanishing external electric field, and c) dipole-corrected slabs with vanishing internal electric field. From ref. [24]

while the Zn-(0001) one is reactive towards OH radicals, a fully symmetric slab (both surfaces are termined with OH groups) with no net dipole moment can be constructed with a 1/2 ML H at the O-$(000\bar{1})$ and 1/2 ML OH at the Zn-(0001) surfaces respectively.

Comparison of different slab calculations are made possible via analysis of the macroscopic average of the Hartree potential (Chap. 2).

4.3 Truncation: the clean (1×1 surface)

As a test case to analyze the electrostatics of the ideal system, and fix slab size and major contributions, we have considered the clean (1×1 surface), as obtained by simple truncation of bonds in the (0001) direction. We analyzed different slab lengths along the polar direction, ranging from 6 to 32 ZnO bilayers and let the system relax. The results are summarized in Fig. 4.4 where it is clear that the slab size does not affect the variation of electric potential across the ZnO region. Indeed, the slope inside the slab, in the portion occupied by ZnO, is related to the macroscopic polarization field of the wurtzite compound. This result allowed us to limit the size of the simulated systems to 12 bilayers. This is important because the surface reconstructions

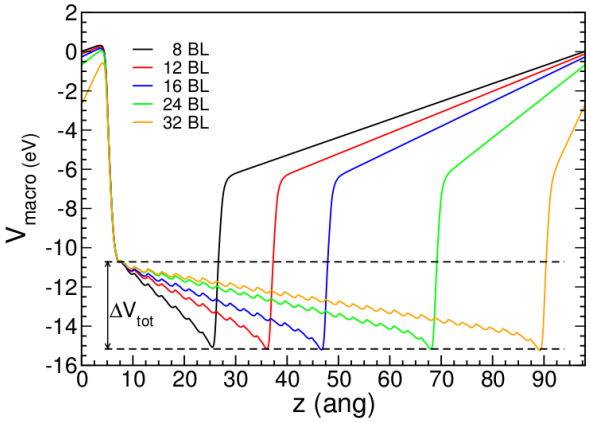

Figure 4.4: 1x1 test ststem: macroscopic potential as a function of the slab size. The electric potential across the slab is not influenced by the number of bilayer considered.

considered require to expand the cell size in the xy plane having to fulfill the surface charge stabilization requirement. In this way the system size increases rapidly as the computational costs.

The most important results of the tests conduced on the clean surface concern the dipole field and its effect on the electronic properties of the system. Fig. 4.5 b)-top panel shows the LDOS relative to the bulk like bilayer located in the slab central region (black) and the surface ones located at O an Zn sides (red and blue respectively). The first noticeable thing is the metallization shown by the system due to the absence of a gap region. As it will be clarified in more detail in Par. 4.4, this is an artificial effect due to a band shift induced by the dipole field which results in a valence and conduction band overlap. This field effect can be understood by comparing these LDOS with the supercell potential trend shown in the same figure (Fig. 4.5 a): as it can be seen the LDOS shift of the two surfaces (red and blue lines) with respect to the bulk one (black), is exactly the potential difference between the edges and the central part of the slab (Δ_1 and Δ_2 respectively). As evidenced, in Fig. 4.5 b)-bottom panel, when applying these rigid shifts to the two different contributions, we observe a gap reopening: the system is no more metallic and the ZnO DOS features are recovered. Since the slope,thus the DOS shifts and fictitious metallicity are related only to the macroscopic dipole, which is a ground state property of the compound, the U correction does not otherwise influence the results. Metallicity can occur only if the potential variation inside the slab is larger than the material band-gap, being an artifact of the calculations in different cases.We thus performed the calculations on larger reconstructions without the U correction.

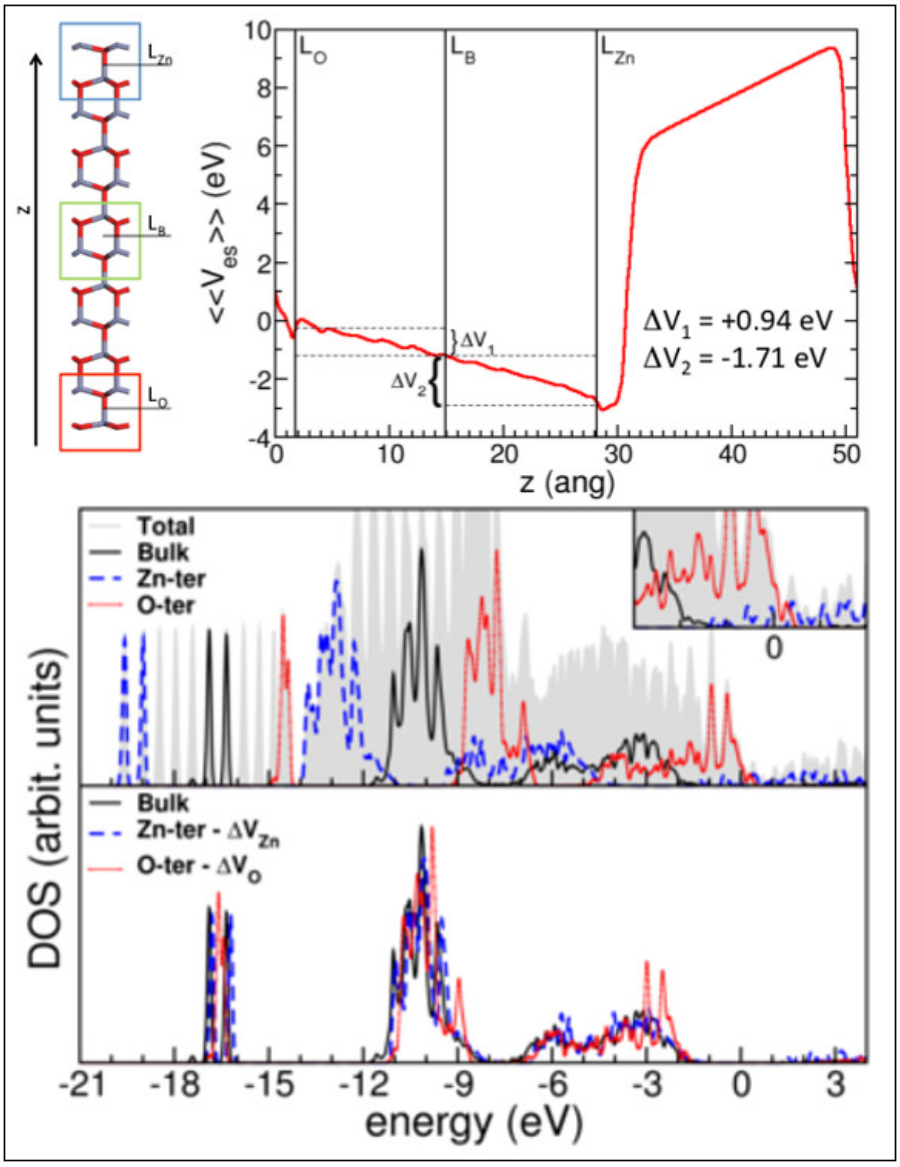

Figure 4.5: Potential trend across the slab (top): The potential differences between the bulk region of the ZnO slab and the two polar surfaces are shown. Local Density of State (LDOS) of the same slab regions (top panel) and the O and Zn-terminated surface LDOS (bottom panel) shifted by the respective values displayed in the potential trend figure. The LDOS shift of the two surfaces with respect to the bulk one is exactly the potential difference between the edges and the central part of the slab

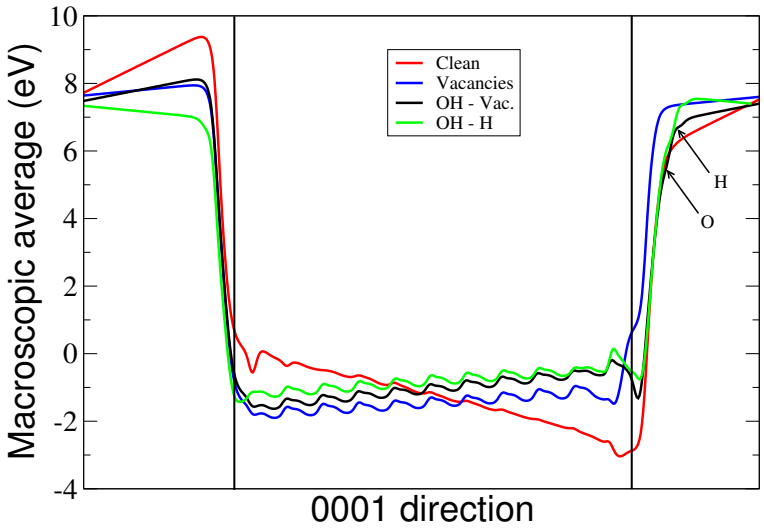

Figure 4.6: Potential trend for clean (red), both terminations vacancy reconstruction (blue), OH-Zn(0001)/vacancies-O(000$\bar{1}$) (black) and OH-Zn(0001)/H-O(000$\bar{1}$) (green) surfaces.

4.4 Defected surfaces

As mentioned in Par. 4.1, a possible solution to quench the dipole field across the slab is to reduce the surface charge through a modification of the surface region composition. The need to satisfy the empirical charge rule leads to an enlargement of the system in the plane perpendicular to the polar direction which depends on the particular reconstruction adopted. For the reconstructions considered in the present work (H and OH adsorption, vacancies and combinations of these) a 2×2 two dimensional cell is sufficient to fulfill the charge compensation criteria, thus all the defected systems calculations were performed in this cell.

We start our analysis comparing different surface stabilization choices in terms of the potential across the supercell. In Fig. 4.6 we show the macroscopic average of the Hartree potential for the different case systems analyzed: vacancies offer an efficient compensation of the extra charges at the two surfaces, as it can be seen from the strong slope reduction with respect to the clean surface calculation. The electric dipole potential inside and consequently outside the slab, are less intense than in the clean case of about 3 eV. Hence the removal of surface charge inhibits the charge transfer mechanism from the outermost layer to the bulk like ones, reducing, as expected, the dipole field.

Let us now consider the different reconstructions adopted: black and green

lines of Fig.4.6 are related respectively to the macroscopic average potential for OH-Zn(0001)/vacancies-O(000$\bar{1}$) and OH-Zn(0001)/H-O(000$\bar{1}$) terminated slabs. One can note that the potential inside the slab is nearly the same for all the three cases and the only differences lie near the surfaces and depend on the details of the various reconstructions. Indeed, the substantial equivalence in terms of dipole potential between all the different compensation choices, is induced by the fact that all reconstructions satisfy the empirical charge rule. As expected a residual dipole potential difference of intensity ranging from 0.5 (OH absorption cases) to 0.9 eV (vacancies case) induced by the surface, and also due to finite size slab effects, is present also in these cases. The residual slope for all these reconstructions is reversed with respect to the clean surface indicating an overcompensation of the surfaces.

4.4.1 Surface Formation Energy and structural analysis

The formation energy, an important surface parameter, corresponds to the energy variation due to the creation of a surface, it is given by the relation that follows:

$$E_{surf} = lim_{N\to\infty} \frac{E_{slab} - E_{bulk}}{A_{slab}} \tag{4.1}$$

Here, E_{slab} and E_{bulk} are the total energies of the unit cell for a n-bilayer slab (a cell with vacuum) and the corresponding bulk (a cell without vacuum with the same number of layers), respectively. A_{slab} is the total area of the surface considered. In order to limit the error due to the dependence of the dipole field on the slab thickness, this value is obtained calculating the surface energy for different slab sizes (or number of layers in the slab, N) and extrapolating the result to $N \to \infty$. When the slab is thick enough, the formation energy linearly increases as a function of the number of layers, i.e. the points lie on a line that asymptotically gives the E_{surf} value for a semi-infinite system. From Fig. 4.7 we obtain that 6 ZnO bilayers are sufficient to simulate the ZnO(0001) surface.

Since both surface terminations are inevitably present for polar surfaces, Eq. 4.1 gives the formation energy of both surfaces, i.e. the cleavage energy, that is the only one well defined for non symmetric slabs with inequivalent surfaces. Fig. 4.7 shows the cleavage energy behaviour as a function of slab size: first of all, it is interesting to note that we obtain an almost linear behaviour, which is a further indication that the slabs considered here are already thick enough to reproduce bulk and non interacting surfaces. The angular coefficient and ordinate value extrapolated at the limit of infinite slab size have thus physical meaning. Focusing on clean case (squares), the only active stabilization mechanism is charge transfer. Surface energy converges

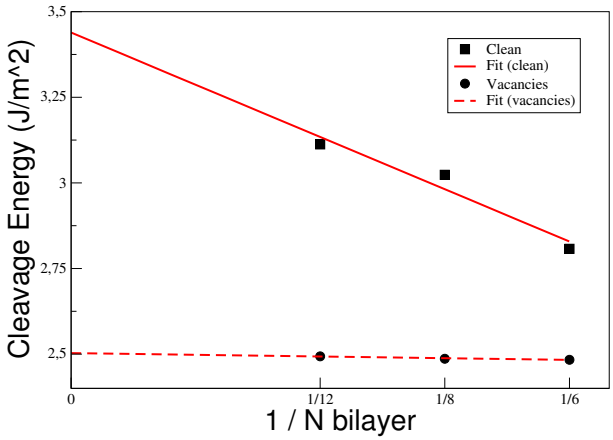

Figure 4.7: Cleavage energy as a function of slab size for clean (squares) and vacancy(circles) reconstructed surfaces and the related linear fit, solid and dashed lines respectively.

slowly to the value of 3.4 J/m^2 (0.21 $eV/^2$) in very good agreement with previous data [14, 15]. The same linear behaviour is found for compensated slabs: when the vacancy model system is considered, as shown in Fig. 4.7 (circles), we found the value of 2.5 J/m^2 (0.15 $eV/^2$). The energy value difference between clean and vacancy cases is attributed to the charge transfer compensation mechanism and the reduced dipole field in the reconstructed cases, with respect to the ideal truncation. We found that this difference is directly related to the formation energy of O and Zn vacancies on the two surfaces:

$$E_{form}^{2vac} = E_{2x2}^{vac} - 4E_{1x1}^{clean} + \mu_{Zn} + \mu_O = 2.65\ eV \tag{4.2}$$

$$(E_{cleav}^{2x2,vac} - E_{cleav}^{1x1,clean}) \times A = 2.15\ eV \tag{4.3}$$

where in Eq. 4.2 E_{form}^{2vac} is the formation energy of the Zn and O vacancies at the two terminations, E_{2x2}^{vac} is the self-consistent total energy calculation for a slab with Zn and O vacancies, the self-consistent total energy calculation for a clean slab is E_{1x1}^{clean} and finally μ_{Zn} and μ_O are the Zn and O chemical potential; while in Eq. 4.3 $E_{cleav}^{2x2,vac}$ is the cleavage energy for a slab with Zn and O vacancies and $E_{cleav}^{1x1,clean}$ is the cleavage energy for a 1×1 slab with clean surfaces and finally A is the surface area.

Another interesting stabilization parameter is the interlayer distance for the two surfaces, since their relaxation strongly depends on the dipole field intensity. Starting from the Clean case, Tab. 4.1 shows that the largest relaxation is found for the O-terminated surface, where the outermost double-layer distance is compressed by almost 50 %. This agrees very well both with previous theoretical works [12] and results of x-ray experiments [17, 21]. For the

	O-$(000\bar{1})$	Zn-(0001)
Clean	-0.316 Å(−49%)	-0.187 Å(−29%)
Vacancies	-0.058 Å(−9%)	-0.381 Å(−59%)
OH and Vac.	-0.058 Å(−9%)	+0.026 Å(+4%)
OH and H.	-0.013 Å(−2%)	+0.039 Å(+6%)

Table 4.1: Zn-O bond length variation (absolute and percentage in parenthesis) with respect to the bulk value (0.645 Å) for the outermost layer at the two slab size, namely at the O-$(000\bar{1})$ and at the Zn-(0001) surfaces. Strong contraction (-) or elongation (+) of the surface Zn-O distance respect to the bulk value indicates a surface structure rearrangement due to the dipole field.

Zn-terminated surface instead there is a discrepancy between theory and experiment indicating that charge transfer is not the best model to describe the stabilization of this surface. Tab. 4.1 shows a contraction of about 29% in very good agreement with all other calculations that predict a contraction of 20%-30% for this surface, whereas no appreciable double-layer distance reduction is revealed by experiments. These considerations suggest that the strong contraction of interlayer distance is due to a greater reactvity and a metallic behaviour of O-termination respect to the Zn one. For the latter surface, Tab. 4.1 highlights the different behaviour for reconstructed cases: for Zn termination, comparing OH and vacancy reconstructed Zn(0001) surfaces, we notice an expansion of about 5% for the first one[2], while a very strong contraction greater than 50% for the last case. Both data are in perfect agreement with the literature [14]. Comparing Tab. 4.1 and Fig. 4.6, it is clear that the variation in bilayer distance is a marker of surface dipole field intensity. In addition, as it will be verified in Par. 4.4.2, the different contraction of the two surfaces is related to the presence of surface states with high density of states.

Analyzing the Zn-O interlayer distance also from the inner layer of the slab, it is possible to appreciate a strong reduction of the internal dipole field in the reconstructed cases: the interlayer distances assume the bulk value already after the first two bilayers. In the clean case instead the bulk value is not reached even for the inner bilayer due to a greater dipole field presence. Another interesting thing observed is that the layer distances of the outermost bilayer reach faster the inner values in the reconstructed cases

[2]This value arises from the average of Zn first layer position since this layer relaxed positions are influenced by OH presence. In particular we found that Zn bound to the OH group are subject to a lower elongation, so that they are located 0.28Ålower than the other Zn atoms of the layer

(second-third bilayer). This is because charge transfer mechanism is inhibited unlike the clean case in which a greater charge penetration in the inner layer is present.

4.4.2 Electronic properties

After showing the potential behaviour within the slab, we focus on DOS and LDOS analysis in order to understand the microscopic mechanisms related to charge transfer between partially occupied states of both surfaces, a phenomenon closely related to the slab dipole field. In the simplified ionic model the outermost layer partial ionicity of $\pm 3/2$ implies that electrons of Zn-terminated (0001) and O-terminated (000-1) surfaces are respectively in conduction and valence band. In this case, thus, the VB would not be entirely filled, giving rise to the supposed metallicity of ideally cleaved surfaces.

DOS analysis
Fig. 4.8 shows the density of states (DOS) for all the considered reconstructions. The first noticeable thing is the expected *metallization* phenomenon shown by the system, due to the presence of occupied states close to the Fermi level (narrow peaks close to the valence band (VB) in a) and b) panels), where valence and conduction bands overlap. This is true only for the first two cases, while in the cases of absorption of OH groups (c) and d)) the presence of a gap and the absence of surface states are noticed. Comparing with Tab. 4.1, the presence of high DOS surface states in the gap is accompanied by large contractions of the interlayer distances at the surfaces. Considering the four cases of Fig. 4.8, from top to bottom panel, a gradual trend towards the ZnO bulk DOS structure is noticed for the valence band top since the narrow peaks related to surface states vanish. In d) panel, even, the gap reaches the bulk values. This further increase of the gap, respect to c) panel, is due to the presence of H atoms at O-termination, that fill the valence band O states[3]. This recovery of bulk features is explained considering that the charge transfer mechanism is more efficiently inhibited starting from the clean surface to the reconstructed ones, as evidenced by DOS and from the occupations of the state. Physically, this is due to a more efficient acceptor levels behaviour, created by the absorption of OH groups, able to completely empty the Zn *4s* surface states near the conduction band (CB). This does not happen indeed in the clean case in which the surface states depletion is only partial. As discussed before, the clean surface is indeed the

[3]We remind that these calculations are performed with standard DFT-PBE and no U correction for the band gap.

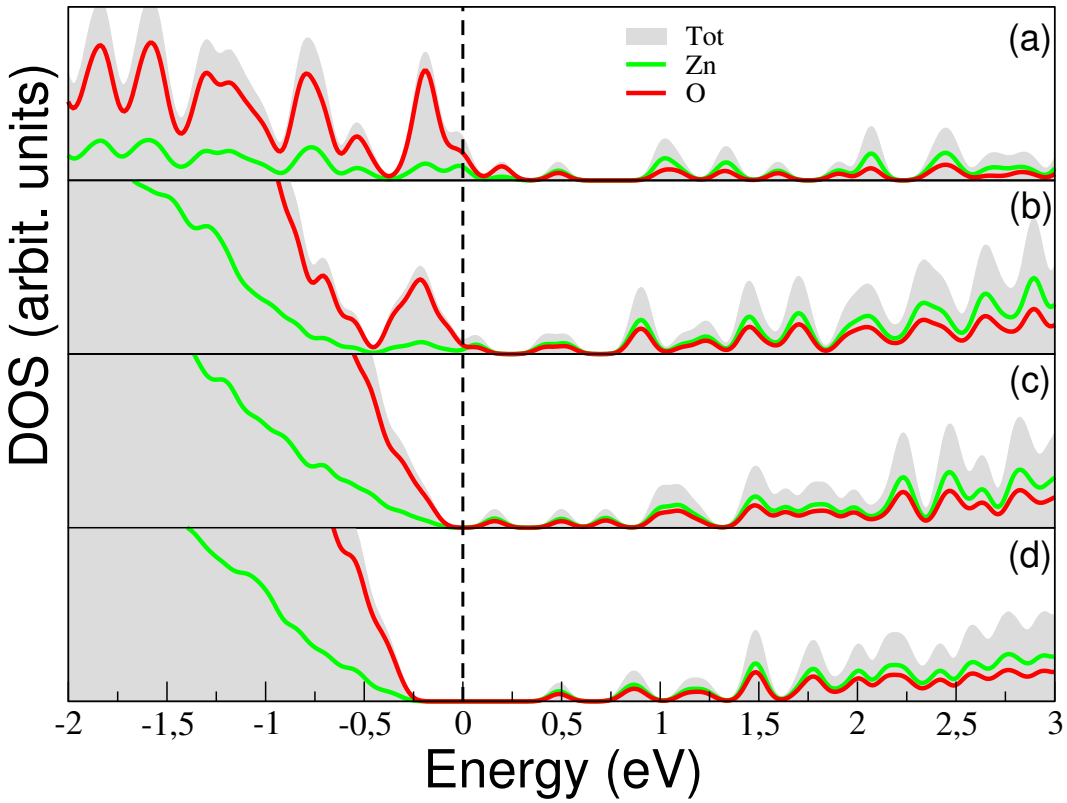

Figure 4.8: DOS for the different configurations studied, in the relevant energy range, around the band gap: a)clean surfaces (1x1x6 slab), b)vacancy reconstructed surfaces (2x2x6 slab) c) OH reconstructed Zn-terminated surface and vacancy reconstructed O-terminated surface (2x2x6 slab) and d) OH reconstructed Zn-terminated surface and H reconstructed O-terminated surface (2x2x6 slab)

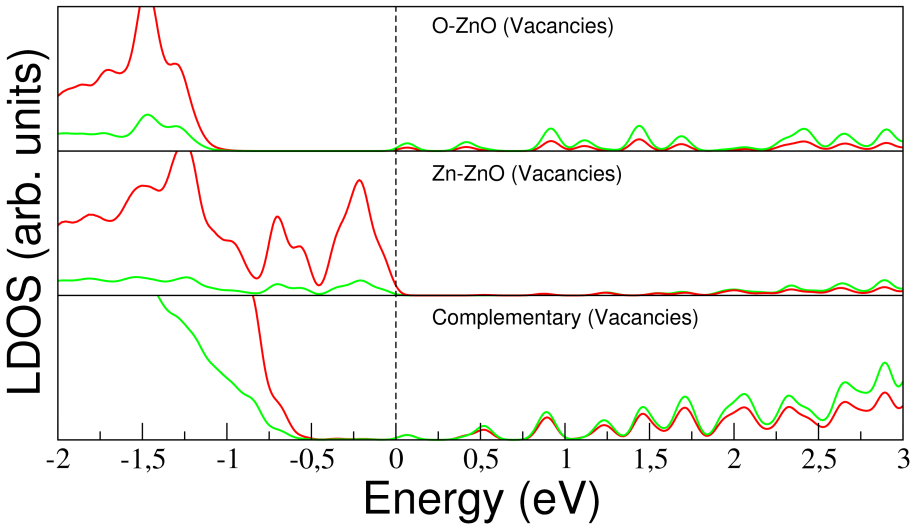

Figure 4.9: a) and b): LDOS of vacancy reconstructed surfaces (outermost layers); c): Complementary of previous LDOS (inner layers, bulk simulation).

only case where the dipole field is larger than the band gap, thus the slab is really metallic; in the other systems, the correction of the band gap problem re-opens the band-gap and cures the fictitious metallicity. The occurrence of surface states is thus not affected by U correction being a marker of each specific reconstuction

Although in c) and d) cases surface states occupations are not fractional and a gap is present, Fig. 4.6 clearly shows the same dipole potential across the slab for all the surface reconstructions. This is because the formation of surface states is not the only contribution to the charge transfer mechanism, but also the presence or absence of dangling bonds is crucial. In the OH case the absence of dangling bonds removes the presence of surface states with fractional occupations at the valence band top that contribute to the reduction of the gap. The same happens in the conduction band when H atoms (d panel) replace vacancies (c panel) to stabilize the O-terminated surface.

The absence of surface states and the wider gap shown in c and d panels, does not imply a smaller slab field with respect to vacancies case. This is because, from the charge reduction point of view, both reconstructions lead to a reduction of $1/4\ e^-$ and consequently to the same potential trend inside the slab, since both satisfy the electrical compensation.

LDOS analysis

To support the previous discussion on the fictitious nature of the surfaces

metallization and to clarify the surface character of the gap states, we performed a local density of states (LDOS) analysis. Fig. 4.9 shows the vacancy model system LDOS plots for O and Zn-terminated surfaces (a and b panel respectively) and for the complementary bulk-like part of the slab (c panel). As it can be seen in a and b panels, both Zn and O termination exhibit a gap, so each surface is individually non-metallic. Thus the metallicity is simply due to the effect of the electric field in a finite slab size, which tends to shift the bands. This shift is responsible of the valence top and conduction band bottom overlap, as if the two LDOS were shifted on each other as observed in DOS plot (see Fig.4.8). Further, Fig. 4.9 a,b) highlight that the DOS shift for each surface, as expected, is of the same order of the relative potential differences showed in Fig. 4.6, as pointed out in Fig. 4.5. The comparision with Fig 4.9 c) where the bulk (the inner layers) LDOS is shown, proves the surface nature of the states close to the Fermi level. Indeed the narrow peaks due to the Oxigens at the valence band top are totally absent in the bulk LDOS, and only a small component for those deriving from Zn at the conduction band bottom remains, due to the their greater penetration in the bulk.

HOMO-LUMO analysis
In order to complete the characterization of the surface states, HOMO and LUMO (Highest Occupied Molecular Orbital and a Lowest Unoccupied Molecular Orbital) plots for reconstructed and clean surfaces are shown (Fig. 4.10): first of all, from the analysis of the charge projection along the slab length, we notice that in all cases HOMO and LUMO are localized on different surfaces, consistently with LDOS plot. Analyzing in more detail these states, we find different origin and location for them. As it can be seen in Fig. 4.10, in the clean case (a), HOMO and LUMO are located, as expected, on O and Zn side respectively, whereas in the other reconstructed cases the locations are inverted. This is due to the re-hybridizaton processes related to rupture and subsequent formation of new bonds that the surface modification implies.

Since HOMO mainly comes from O 2p states it is either associated with O-term($000\bar{1}$) surface dangling bonds (clean case, Top panel in Fig. 4.10) or to residual dangling bonds at Zn vacancies/adsorbates in the Zn-term(0001) surface. The opposite is true for LUMO state, mainly originating from Zn-s* like states. Comparing Fig. 4.10 and 4.6 we notice that, the reverse HOMO-LUMO localization is also correlated to the slab potential trend: the potential slope variation from clean to recostructed surfaces shown by Fig. 4.6,indeed, closely follows the change in HOMO-LUMO surface location. Thus we can conclude that the HOMO-LUMO location is largely influenced by the residual dipole field.

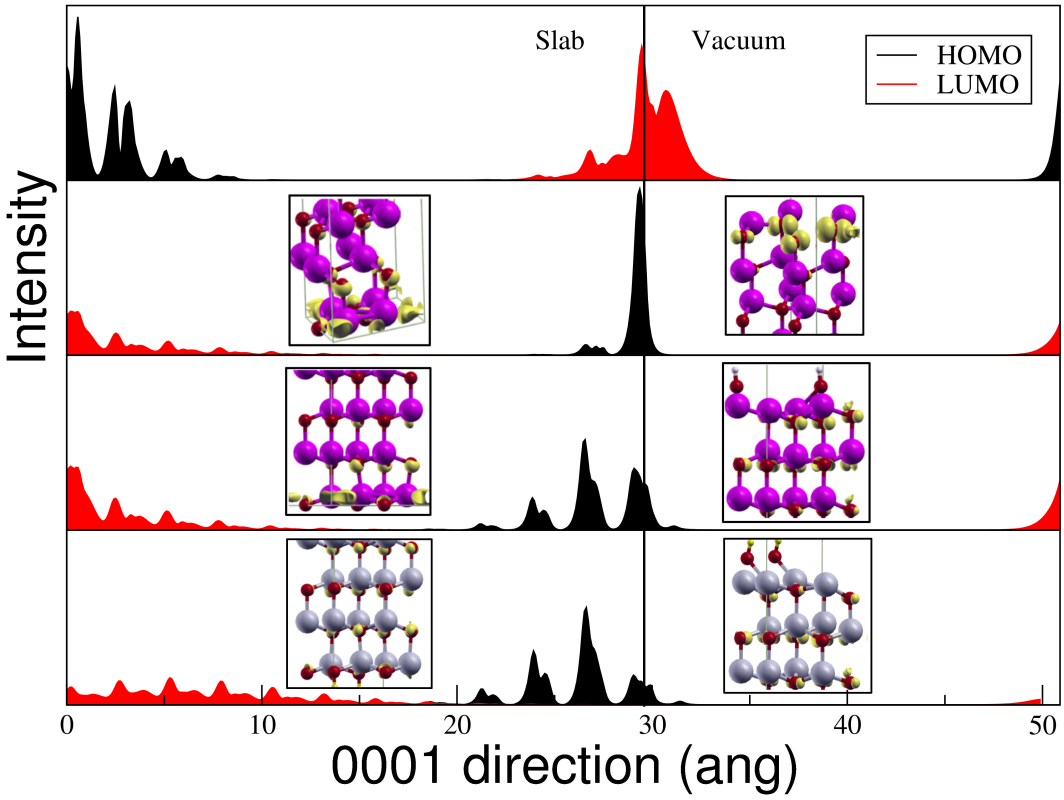

Figure 4.10: HOMO and LUMO plots of clean (a), vacancy reconstructed surfaces (b), OH reconstructed Zn-terminated surface and vacancy reconstructed O-terminated surface (c) and OH reconstructed Zn-terminated surface and H reconstructed O-terminated surface (d). These states 3D plots version are presented in the insets for the reconstructed cases.

The comparison between c) and d) panels shows that the absence of vacancy-induced dangling bonds and the introduction of Hydrogen atoms at the O terminated surface, leads to a bulk-like LUMO state (d panel). The disappearance of a LUMO surface state is associated with a lower contraction of the outermost layer as described in Tab. 4.1.

In conclusion, the electronic analysis performed proves the fictitious nature of the ZnO polar surface metallization: this phenomenon essentially consists in a field induced shift of the LDOS, that causes valence and conduction bands overlap. The different stabilization mechanisms studied are equivalently efficient in decreasing the dipole slab potential as evidenced in Fig. 4.6, although accompanied by different structural and electronic details, derived from the presence/absence of surface or adsorbate states.

4.5 Conclusions

In this chapter we have considered the electrostatics of ZnO(0001) surfaces. We fully characterized the dipole field behaviour along (0001) ZnO polar direction and discussed, from the electronic point of view, the results concerning the electrical stability of polar surfaces. All the studied reconstructions exhibit a substantial equivalence in terms of supercell potential. However many microscopic differences were found, evidenced mainly from DOS and HOMO-LUMO analysis.

This investigation and the relative results are an important starting point for the subsequent study of the Al/ZnO interface, where the dipole field influence must be taken into account in determining the interface features.

Bibliography

[1] L. Landau and E. Lifshitz, *Electrodynamics of Continuous Media*, (Pergamon, Oxford, 1984);

[2] J. Nye, *Physical Properties of Crystals*, (Oxford University Press, London, 1957);

[3] R. M. Martin, Phys. Rev. B **9**, 1998 (1974);

[4] R. Resta, Rev. Mod. Phys. **66**, 899 (1994);

[5] R. D. King-Smith and D. Vanderbilt, Phys. Rev. B **47**, 1651(1993)

[6] Landolt-Boernstein - *Group III Condensed Matter Numerical Data and Functional Relationships in Science and Technology, Volume 41B: II-VI and I-VII Compounds; Semimagnetic Compounds*, Edited by O. Madelung, U. Roessler, M. Schulz;

[7] Andrea Dal Corso, Michel Posternak, Raffaele Resta, and Alfonso Baldereschi, Phys. Rev. B **50**, 10715-10721 (1994)

[8] P. W. Tasker J. Phys. C: Solid State Phys., Vol. **12**, 1979

[9] J. Goniakowski, F. Finocchi and C. Noguera Rep. Prog. Phys. **71** 016501 (2008)

[10] C. Woll Progress in Surface Science **82** 55-120 (2007)

[11] Olga Dulub, Lynn A. Boatner, Ulrike Diebold Surf. Sci. **519** 201-217 (2002)

[12] B. Meyer and D. Marx Phys. Rev. B **67** 035403 (2003)

[13] O. Dulub, U. Diebold, G. Kresse, Phys. Rev. Lett., **90**, 016102 (2003);

[14] G. Kresse, O. Dulub and U. Diebold Phys. Rev. B **68** 245409 (2003)

[15] B. Meyer Phys. Rev. B **69** 045416 (2004)

[16] Jeppe V. Lauritsen, Soeren Porsgaard, Morten K. Rasmussen, Mona C. R. Jensen, Ralf Bechstein, Kristoffer Meinander, Bjerne S. Clausen, Stig Helveg, Roman Wahl, Georg Kresse, and Flemming Besenbacher, ACS Nano **5**, 5987-5994 (2011);

[17] A. Wander et al. Phys. Rev. Lett. **86** 17 (2001)

[18] Valtiner, M.; Todorova, M.; Grundmeier, G.; Neugebauer, J. T, Phys. Rev. Lett. **103**, 065502 (2009)

[19] Lindsay, R.; Muryn, C. A.; Michelangeli, E.; Thornton, G., Surf. Sci., **565**, L283-L287; (2004)

[20] Overbury, S. H.; Radulovic, P. V.; Thevuthasan, S.; Herman, G. S.; Henderson, M. A.; Peden, C. H. F., Surf. Sci. **410**, 106-122; (1988)

[21] N. Jedrecy, M. Sauvage-Simkin, R. Pinchaux Appl. Surf. Sci. **162-163** 69-73 (2000)

[22] Z. L. Wang, J. Phys. Cond. Mat. **16**, R829 (2004).

[23] L. Schmidt-Mende and Judith L. MacManus-Driscoll, Materialstoday **10** 5 (2007)

[24] B. Meyer and David Vanderbilt Phys. Rev. B, **63**, 205426 (2001)

[25] Mirco Bazzani, Andrea Neroni, Arrigo Calzolari, and Alessandra Catellani, Appl. Phys. Lett. **98**, 121907 (2011)

[26] Terentjevs, A. Catellani, D. Prendergast, and G. Cicero, Phys. Rev. B **82**, 165307 (2010)

[27] J. Baxter et al. Nanotechnology **17**, 304 (2006)

[28] Paolo Giannozzi, Stefano Baroni, Nicola Bonini, Matteo Calandra, Roberto Car, Carlo Cavazzoni, Davide Ceresoli, Guido L Chiarotti, Matteo Cococcioni, Ismaila Dabo, Andrea Dal Corso, Stefano de Gironcoli, Stefano Fabris, Guido Frates, Ralph Gebauer, Uwe Gerstmann, Christos Gougoussis, Anton Kokalj, Michele Lazzeri, Layla Martin-Samos, Nicola Marzari, Francesco Mauri, Riccardo Mazzarello, Stefano Paolini, Alfredo Pasquarello, Lorenzo Paulatto, Carlo Sbraccia, Sandro Scandolo, Gabriele Sclauzero, Ari P Seitsonen, Alexander Smogunov, Paolo Umari and Renata M Wentzcovitch, J. Phys.: Condens. Matter **21**, 395502 (2009). See also `www.quantum-espresso.org`.

[29] J. P. Perdew, K. Burke, and M. Ernzerhof, Phys. Rev. Lett. **77**, 3865 (1996).

[30] D. Vanderbilt, Phys. Rev. B **41**, R7892 (1990).

[31] H. Karzel et al. Phys. Rev. B **53** 11425 (1996)

[32] M Peressi, N Binggeli and A Baldereschi J. Phys. D: Appl. Phys. **31** (1998) 1273-1299.

[33] C. Noguera J. Phys.: Condens. Matter **12** (2000) R367-R410

[34] Z. Yufei et al. J. of Semicond. **31** 8 (2010)

[35] J. H. Song et al. Phys. Rev. B **77** 035332 (2008)

[36] A. Wander and N. M. Harrison. J. Chem. Phys. **86** 17 (2001)

Chapter 5

Al/ZnO interface

This chapter is focussed on the main target of the PhD project: the microscopic characterization of the Al/ZnO(0001) interface. Determining the contact behavior (Ohmic vs Schottky) of the interface is mandatory for an optimal modeling of a ZnO based device. As it will be clarified later this aim is very challenging and actual due to the discrepancy between the different theoretical models and experiments. For this compound the macroscopic polarization, and the very many surface reconstructions and local dipole fields play a critical role. Thus a consistent description of this interface is still lacking: the experiments are largely affected by preparation and ambient conditions, which alter in a severe way the polar surface characteristics; on the other hand, while simple model approaches proposed in the past on branching points and Fermi level pinning are ruled out because of bond ionicity and different defect levels usually present at the interface, the most recent band alignment theory developed at DFT level has never been applied in the presence of a macroscopic polarization. From this scenario it is clear that the microscopic description of the structural and electronic properties of the interface as obtained by ab initio simulations may be a fundamental tool to complement the experiments, providing an unbiased understanding.

5.1 Introduction

ZnO has emerged as an exciting new material for wide bandgap optoelectronics and microelectronics [1–3]. With the development of new device applications, an increased demand for the understanding and control of ZnO electrical contact properties has been renewed. These contacts play a central role in the performances of next generation optoelectronics devices. Transparent thin film transistors, blue/UV light emitting diodes and lasers, UV photodetectors, high electron mobility transistors, electronic nanostructures, and spintronics all require metal contacts and hence an understanding of

how electronic properties depend on the nature of ZnO surfaces, ZnO-metal interfaces and the processes involved during contact formation. Until the last decade, research on electrical contacts on ZnO centered primarily on its surface physics and chemistry, due to the pronounced effects that surface atomic bonding and polarity have on charge transfer with adsorbates [4–7]. Yet, at present, a number of controversial experimental data are observed as evidenced by the wide and variable range of barrier heights measured from the same metal on a given ZnO surface [8,9]. For example, the barrier heights of Au diodes on ZnO can range from 0 to 1.2 eV, depending on the crystal, the surface preparation, and the conditions under which the contact is formed. Diodes formed with other metals such as Pt and Ta on ZnO exhibit barrier heights that span a large energy range as well [10]. Furthermore, the n-type barrier heights that should occurr for high work function metals are lower than expected. The observed strong dependence on surface preparation indicates that extrinsic factors such as crystal quality and surface treatment have a relevant effect on ZnO barrier heights.

Along with Schottky barriers (SB), Ohmic contacts represent the two basic metallization technologies for semiconductor device fabrication. According to the simple Schottky model, when a metal is brought into intimate contact with a semiconductor, the Ohmic or rectifying character of the contact depends only upon the work function of the metal and the electron affinity of the semiconductor. Ideally, a metal-semiconductor junction results in an Ohmic behavior if the barrier formed at the contact is zero. In such a case, the carriers are free to flow in or out of the semiconductor so that there is minimal resistance across the contact. For an n-type semiconductor, this means that the work function of the metal must be close to or smaller than the electron affinity of the semiconductor (Fig. 5.1).

Experimental results show that a strong dependence of barrier height on the metal work function is only true for ionic semiconductors. The experimental results for less ionic compounds, such as most of III-V semiconductors, present a barrier height which is almost independent of the metal work function [11]. This has been interpreted in a phenomenological way as due to the fact that usually the Fermi energy level at the interface is pinned in a narrow energy range by intrinsic or extrinsic interface states within the bandgap [12–14]. Most of II-VI semiconductors have instead ionic bonding and large differences in electronic affinity, resulting in unpinned Fermi levels. Consequently, formation of Ohmic contacts to those semiconductors can be realized based on the values of the metal work function and semiconductor electron affinity. ZnO lays at the borderline between covalent and ionic semiconductors. Thus, formation of Ohmic contacts to ZnO with low contact resistivity can be achieved by reducing the barrier height, or/and increas-

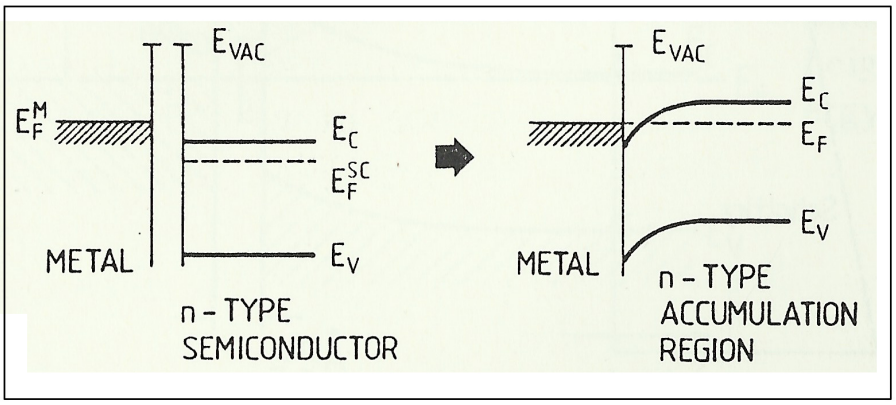

Figure 5.1: Schematic diagrams of band bending before and after metal-semiconductor contact for a low work function metal and n-type semiconductor

ing the ZnO surface doping density so that the barrier width becomes thin enough for carriers to tunnel through.

From a theoretical point of view the comprehension of the intrinsic mechanisms governing the formation of Schottky barriers at metal-semiconductor interfaces have been a source of debate since the first model provided by Schottky and Mott in the 1930s [15–17]. Since then, research into this fundamental issue has focused on the choice of a reference level to align energy band diagrams of the different materials: it has first been proposed that the relationship between Schottky barrier height and metal work function could be linked to the electronegativity of the different semiconductors thus providing a measure of the degree of Fermi-level pinning by interface states. The capability of this model to predict the Schottky barrier-metal work function trend, has led to the replacement of the Schottky-Mott model, with alternatives that make different assumptions concerning the nature of the electronic states at the Metal-Semiconductor interface. Among these, the metal-induced gap states (MIGS) model of Heine and Tersoff [18–20] in which intrinsic interface states are created by the quantum mechanical tunneling of metal wave function tails into the band gap of the semiconductor, has gained increasing popularity. These states arise from truncation of real states at the interface, and belong to the class of virtual gap states (ViGS) with eigenvalues generally within the gap and complex k vectors, and thus give rise to a complex band structure [21]. The ViGS may be understood as a continuation of bulk valence-band (VB) and conduction-band (CB) states extending into the fundamental gap of a semiconductor. At a certain energy, called the branch-point energy (BPE), these states change their character from predominantly VB-like or "donor-like" to mostly CB-like or "acceptor-like". Across the in-

terface, tunneling from one material to the other such states transfer a net charge, the sign of which depends on the position of the Fermi level relative to the BPE. According to Tersoff this charge transfer leads to an intrinsic interface dipole that tends to line up the energy bands in a way that the dipole itself vanishes. Therefore, BPE serves as an energy reference for the band alignment. In the case of a metal-semiconductor contact, this energy is frequently called charge neutrality level. Tersoff established a method to obtain the actual band lineup and therefore the relative energetic positions of the energy gaps by computing BPE for each of the involved semiconductors. An advantage of Tersoff's method is that it explains, in convincing agreement with experiments, the band lineup just in terms of the bulk band structure, i.e., neglecting structural details of the actual interface.

Tersoff method cannot be applied to systems where the BPE appears in the CB region, although there is experimental evidence that the BPE may also occur outside the gap within the bands. This is found for example for wurtzite semiconductors such as ZnO, which is naturally n-doped, as grown. Furthermore, as it will be shown later, a direct evaluation of these SB formation models is complicated by the fact that experimentally determined values of Schottky barriers are sensitive to extrinsic effects such as semiconductor surface contamination, structural faults, and point defects that result in a competition of several interface charge transport mechanisms as well as chemically-active interface structures that alter the traditional Schottky barrier model.

ZnO is an important material for testing the validity of different SB formation models because it is an ionic n-type semiconductor in which Fermi-level pinning is expected to be weaker than for more covalently bonded materials, allowing SB to vary with metal properties [5]. In addition, quasiparticle band-structure calculations place its branch point energy in the first conduction band, which according to MIGS theory should severely restrict the barrier height of metal/semiconductor contacts [5, 22]. From an experimental point of view, a wide range of Schottky barriers are observed for a given metal on ZnO, depending on surface preparation prior to metal deposition [10, 23]. This means that defects play an important role in SB formation and also that not only surface treatment but also the quality of ZnO crystals is a significant factor [24]. The sample quality indeed can vary dramatically depending on the growth method, annealing conditions and subsequent polishing or etching.

Chemistry also plays an important role at metal-ZnO interfaces. There is a qualitative difference between reactive versus nonreactive metal/ZnO interfaces, both in terms of bond formation and/or interdiffusion that can take place as well as the extrinsic defects that such chemical interactions pro-

duce [25]. Metals such as Al, Ta, Ti, and Ir react with oxygen to form oxides with high heats of formation [26,27]. Metals such as Au, Pd, and Pt can form eutectics with Zn whose enthalpy change can drive new interface bonding as well [10]. The reacted layers produced at these metal/ZnO interfaces create interface layers with not only electric dipoles but also native point defects that can act as electrically active donors or acceptors, hopping sites, as well as recombination centers. Thus metals that react with ZnO to form oxides produce defects associated with oxygen vacancies, whereas metals that form eutectics with Zn produce defects associated with zinc vacancies. Depending on the density of defects and the extent of reaction in the sub-surface region, reactive metals can form either Ohmic or blocking contacts.

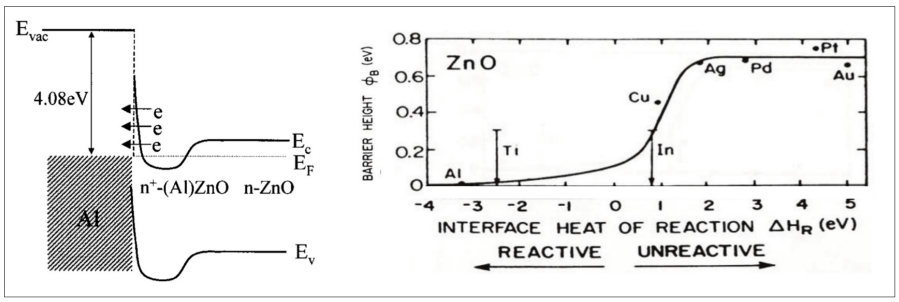

Figure 5.2: Left panel, band diagram of Al-based Ohmic contact on ZnO. The interdiffusion of Oxygen and Aluminum at the interface result in a highly doped AZO surface [28]. Right panel, Schottky barrier height for different metals [10].

Aluminum is a promising metal for forming Ohmic contacts with n-ZnO due to its low barrier height. It has been proposed that O atoms have a tendency to out-diffuse from ZnO and participate in the formation of Al_2O_3 at the interface [28–31], with accumulation of oxygen vacancies near the ZnO surface, that might be responsible of a heavily doped n-ZnO region (see Fig. 5.2). This interdiffusion between Al and O atoms would than result in an increase of doping concentration in the ZnO:Al surface region. Therefore, the Al/ZnO contact actually should consist of the Al/n-(Al)ZnO/n-ZnO structure. The heavily doped n-ZnO surface should reduce the barrier width, enhancing the tunneling process between metal and n-ZnO layer as shown schematically in Fig 5.2.

In order to shed light on these issues and offer a microscopic description of the Al/ZnO(0001) interface, we have performed a series of ab initio calculations, both for the buried interface, and for an interface between ZnO and few Al layers, in the presence of vacuum, to simulate a system closer to experimental conditions.

5.2 Method

We performed density functional total-energy-and-force calculations, as implemented in the Quantum-ESPRESSO package [32]. Calculations were performed employing GGA-PBE and ad an hoc Hubbard correction as for the previous simulations described in this work. This sets the value of the Kohn-Sham gap for ZnO to 3.1 eV, very close to the experimental one (3.3 eV). The atomic potentials are described by ab initio ultrasoft pseudopotentials. The electronic wave functions (charge density) are expanded in a planewave basis with an energy cutoff of 28 Ry (280 Ry), fully consistently with the other studies described in this thesis. For Brillouin zone (BZ) integration, we use a 4x4x1 k-point Monkhorst-Pack mesh. All structures are relaxed until forces on all atoms are lower than 0.03 eV/Å.

We first optimized ZnO and Al bulk crystal structures to fix equilibrium lattice parameters, with which then build the interface supercells (see below). The supercells used in the present work are composed by 8 Zn-O double layers and 4 Al layers in the presence of 18 Å vacuum region. The same slab has also been studied without vacuum, to reproduce a buried interface. The number of layers employed at each portion of the slab allows to correctly simulate the physical quantities of interest in the SB height calculation such as the work function of the individual components (see Fig. 5.3), while preserving the bulk characteristics of the material at each side of the interface.

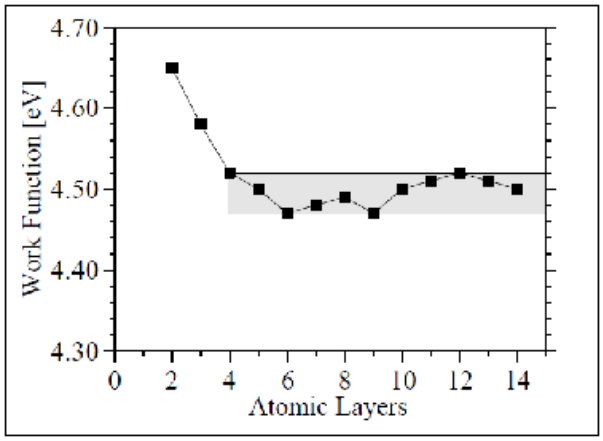

Figure 5.3: Aluminum work function calculation as a function of the slab thickness. From [36]

The main problem in building the supercell was how to interface the two different crystallographic structures of wurtzite-ZnO and Al. As previously described, since SB is very sensitive to the interface microscopic details, mod-

elling the interface with the lowest mismatch and structural stress is a crucial point. Unlike most of the works present in literature that consider an ideally unstrained interface where the metal is perfectly lattice matched to the semiconductor [35], we studied the configuration with lowest interface mismatch, as it can be obtained experimentally. This condition was reached by building up an interface composed of a $\sqrt{3} \times \sqrt{3}$ ZnO(0001) cell and a 2x2 Al(111) (a total of 64 atoms), preserving epitaxial relations with an Al lattice residual strain lower than 1%. Fig. 5.4 helps identifying the different sublattices and the adopted matching construction.

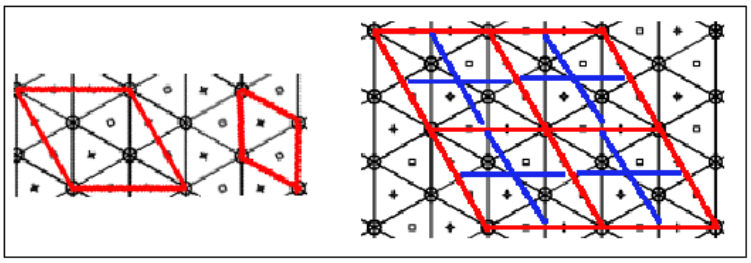

Figure 5.4: Left panel: comparison between ZnO unit cell (the smallest) and the 30° rotated $\sqrt{3} \times \sqrt{3}$ cell. Right panel: representation of the 4x4 Al(111) (blue) and $2\sqrt{3} \times 2\sqrt{3}$ ZnO(0001) (red) lattice match.

Another crucial point in building up the system is the presence of a macroscopic dipole field in the ZnO slab. From the previous dipole analysis described in Chap. 4, we adopted a slab stabilized by the presence of vacancies at both surfaces (Zn-term(0001) and O-term($000\bar{1}$)) to compensate the surface charge: since this means a suppression of 1/4 atoms per surface cell, and because there are 3 surface atoms for each $\sqrt{3} \times \sqrt{3}$ ZnO cell, the final supercell has a two-dimensional size of $2\sqrt{3} \times 2\sqrt{3}$ ZnO, and so a 4x4 Al(111) cell. This configuration chosen to reduce the dipole field effect and lattice mismatch makes the system very demanding (250 atoms, 2000 electrons). By comparison between clean ($\sqrt{3} \times \sqrt{3}$) and vacancy reconstructed ($2\sqrt{3} \times 2\sqrt{3}$) surfaces it is possible to obtain clear guidance on how the dipole field affects interface details and SB height.

Summarizing the configurations studied are:
i) $\sqrt{3} \times \sqrt{3}$ ZnO cell with clean surfaces interfaced with a 2x2 Al(111) cell at the Zn-terminated surface. The interaction between Al and O-terminated surface is prevented by a vacuum region. In the following we will refer to this system as clean free interface.
ii) $2\sqrt{3} \times 2\sqrt{3}$ ZnO cell with vacancy reconstructed surfaces interfaced with a 4x4 Al-(111) cell at the Zn-terminated surface. The interaction between Al and O-terminated surface is prevented by a vacuum region. In the following

we will refer to this system as vacancy free interface.
iii) $\sqrt{3} \times \sqrt{3}$ ZnO cell with clean surfaces interfaced with a 2x2 Al-(111) cell at the Zn-terminated surface. The vacuum region is removed and thus two interfaces are present in this case, since Al and O-terminated surface can now interact. In the following we will refer to this system as clean buried interface.

We adopted the planar average technique for the SB calculations: the determination of the valence-band offset (Schottky barrier) across the interface between two semiconductor (metal/semiconductor), involves lining up the band structures of the two materials (Fig. 5.5), which can be obtained by considering only the variation of the electrostatic potential perpendicular to the interfacial plane, while the other two coordinates can be removed by averaging in planes parallel to the interface, as already defined (see Chap. 2). In

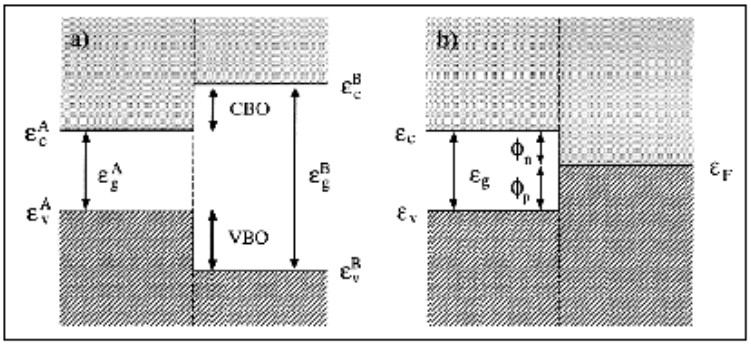

Figure 5.5: Schematic diagrams of the band structures of semiconductor-semiconductor (a) and semiconductor-metal (b) contacts and band offsets - Schottky barriers definitions.

this way, the valence-band offset (Schottky barrier) can then be determined as [36–38]:

$$SBH = (E_F - \bar{\bar{V}}_{Met}) - (VBT - \bar{\bar{V}}_{Sem}) + \Delta V_{int} \tag{5.1}$$

where E_F is the Fermi level of the metal, VBT the semiconductor valence band top and $\bar{\bar{V}}$ the respective macroscopic average potentials. The Schottky barrier is conveniently split into two contributions: a band structure term and an interface term. The band structure term is the difference between the relevant valence band edges in the two materials (between the Fermi level of the metal and the valence-band edge of the semiconductor for a metal-semiconductor contact), when the single-particle eigenvalues are measured with respect to the average electrostatic potential $\bar{\bar{V}}$ in the corresponding bulk crystal. The band-structure term is characteristic of the individual bulks.

This term can be obtained from standard bulk band-structure calculations for each crystal and displays, by definition, transitivity. This is not the case for the electrostatic potential line-up ΔV_{int}, which can, in principle, depend on structural and chemical details of the interface. The potential line-up across the interface between two semi-infinite solids cannot be simply calculated as the difference between bulk quantities; rather, it depends in principle on the detailed structure of the interface. This makes the problem of band alignment at interfaces difficult and it is in principle necessary to calculate accurately the interface charge distribution and the corresponding electrostatic potential. The difference between the macroscopic averages of the electrostatic potential in the two bulk regions is precisely the electrostatic potential line-up, ΔV_{int}. Furthemore, since the macroscopic average commutes with the spatial differentiation in the Poisson equation, the above relation allows one to define in an unambiguous way the concept of the interface dipole for any surface or interface.

$$\Delta V = 4\pi e^2 \int z \, \bar{\bar{\rho}} \, (z) dz \tag{5.2}$$

The SBH calculation in the presence of a macroscopic dipole field along the polar direction where the interface is built are not described in literature, thus we had to study its effect and adapt the well-established methods to the present case.

5.3 Result and discussion

In this section the results relative to Al/ZnO interface simulations will be presented. First the structural and electronic properties of the contact will be discussed taking into account the effects of the ZnO macroscopic polarization field. This analysis allows to highlight important microscopic details such as the presence of surface states, the influence of surface defects and how the presence of the metal affects the ZnO features at the interface. These electronic and structural interface details are critical aspects to characterize from the theoretical point of view the contact type and establish its Ohmic or Schottky character.

5.3.1 Structural analysis

We start our analysis from interface stuctural features: in Fig. 5.6 the relaxed structures relative to the clean and vacancacy free interface systems (see Par. 5.2 for system definition) are shown. As it can be seen from direct inspection, the two interfaces present remarkably different signatures: for the clean case

(left structure) the relaxed atomic positions are very close to the ideal Al and ZnO structures. This occurs both for the free and the buried interface.

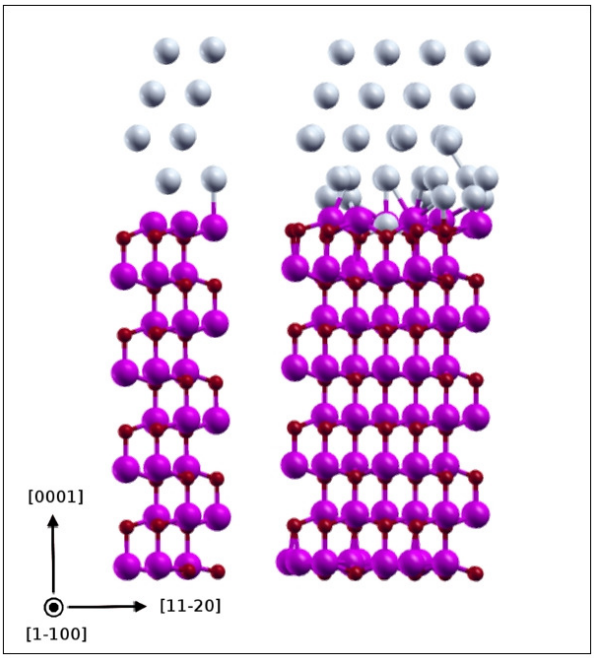

Figure 5.6: Side view along the $(1\bar{1}00)$ direction of the relaxed structures for the clean (left) and vacancy (right) free interface systems. Pink (red) spheres indicate Zn (O) atoms, while Al atoms are indicated as grey spheres.

On the contrary, when ZnO surfaces are vacancy reconstructed (right structure) a strong structural rearrangement at the interface takes place. Now we focus on this case: looking at the first Al layer we notice different behaviour of the atoms: some Al atoms remain substantially in the ideal position, while some of them go down along the polar direction toward the ZnO slab of about 0.8 Å. An Al atom penetrates into the site left empty by one of the three Zn vacancies: according to our previous results on AZO, and Al affinity for O, the Al substitutional atom is involved in bonding with the surrounding oxygens. This situation is presented in detail in Fig. 5.7, where the coordinates along the polar direction (z axis) of the atoms belonging to each Al layer are shown. As it can be seen only the Al atoms belonging to the interface layer are subjected to big variation compared to the initial positions.

In order to understand the origin of the different behavior of Al atoms at the interface layer, Fig. 5.8 shows, respectively, the initial and relaxed positions of the interface layers (first bilayer Zn-O and the first Al layer).

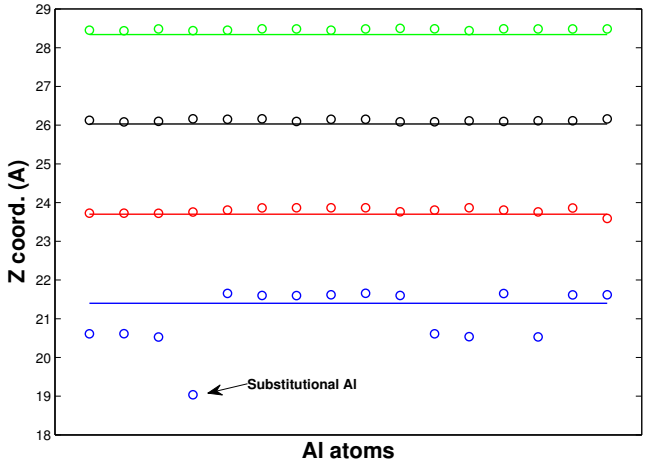

Figure 5.7: Vacancy reconstructed surfaces, coordinates along the polar direction (z axis) of the atoms belonging to each Al layer (circles) in comparison with the relative ideal position (solid lines in the same colour). First interface Al layer are depicted in blue, the second in red, the third in black and the outermost in green.

The first thing to note is the enormous influence of Zn vacancies on the first Al layer: since the three vacancies are not equivalent with respect to the Al atomic positions, their effect on the surrounding Al atoms will be different. Indeed, because of the different stacking of two crystallographic structures, some Al and Zn atoms have the same coordinates on the xy plane and Al lyes just above a Zn atom of the underlying layer, while the projection of the remaining Al atoms on the layer below is the midpoint between two Zn atoms (see the left panel of Fig. 5.8). For this reason, as previously mentioned, the three vacancies are inequivalent: with reference to the the left panel of Fig. 5.8, the vacancy of the first type is indicated by a square while the second type ones with a circle. The presence of these different vacancies is responsible for the strong structural rearrangement pointed out in the right panel of Fig. 5.8 (see also Fig. 5.7): Al atoms not immediately close to a Zn vacancy remain essentially in their ideal positions (green atoms), while the other Al, move closer into the ZnO substrate. Depending of the two kind of vacancies, Al atoms can penetrate deeply and replace the missing Zn (first type vacancies) or descend in an intermediate position between their initial position and the Zn layer (second type).

The just exposed structural analysis provides a first important indication of the metal tendency to penetrate into the ZnO substrate: as it will be

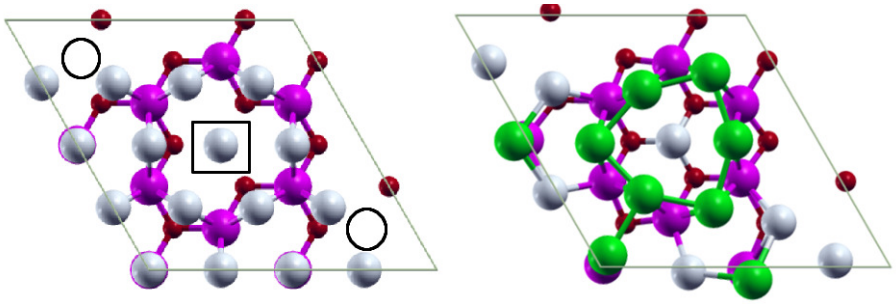

Figure 5.8: Vacancy reconstructed surfaces, initial (left panel) and relaxed (right panel) positions of the interface layers (first bilayer Zn-O and the first Al layer). For an easy viewing the Al atoms that remains substantially in their initial positions are shown in green.

clarified in the next section by electronic analysis, in this process some characteristics of AZO reappar. These issues are in agreement with experimental data relative to annealing processes where formation of AZO regions have been found at the Al/ZnO interface [28, 29].

We conclude this section on the structural properties of the interface with an analysis of the interlayer distances: beyond a simple structural detail, in this specific case, where large interface dipole fields are present, contraction of interlayer distances can be linked to electronic polarizations, thus providing useful information. The interlayer distance is indeed a useful field marker since the presence of a dipole field in the slab leads to large structural rearrangements of the surface layers (see Chap. 4). As visible from a comparison of Tab. 4.1 (Chap. 4) and Tab. 5.1, the Al effect is to act as an electron reservoir: a charge transfer between Al and ZnO surfaces takes place, providing a dipole field reduction as inferred by a lower contraction of the interlayer distances in all cases at the Zn-(0001) interface and also at the O-$(000\bar{1})$ buried interface where an Al/O contact is formed.

5.3.2 Electronic properties

In this section the electronic properties of the Al/ZnO interface will be discussed: the DOS analysis carried out is very important in order to point out the interface microscopic features, such as the presence of defects or influence of the chemical bond, that play an important role in Schottky barrier height. In order to highlight the interface details the local density of states (LDOS) for each part of the system will be presented. This is important also to emphasize the interface contributions and to separate the macroscopic dipole field effect, since both these aspects can affect the Schottky barrier height.

	O-$(000\bar{1})$	Zn-(0001)
Clean free interf.	-0.316 Å(−49%)	+0.003 Å(+0.4%)
Vacancies free interf.	-0.064 Å(−10%)	+0.001 Å(+1.6%)
Clean buried interf.	+0.039 Å(+6%)	+0.032 Å(+5%)

Table 5.1: Al/ZnO contact, Zn-O bond length variation (absolute and percentage in parenthesis) with respect to the bulk value (0.645 Å) for the outermost layer at the two slab sizes, namely at the O-$(000\bar{1})$ and at the Zn-(0001) surfaces. Strong contraction (-) or elongation (+) of the surface Zn-O distance respect to the bulk value indicates a surface structure rearrangement due to the dipole field. The Aluminum effect is to stabilize the surfaces with which it is in contact, as can be seen in particular comparing the differences between the two clean cases (first and last row).

Clean free interface

We start our analysis from the interface between Al and a ZnO clean surface slab. In Fig. 5.9, we reproduce in different panels the LDOS projected on atoms belonging to different portions of the slab, namely, from top to bottom. Region a) represents the DOS for an Al bulk-like layer placed in the middle of the Al slab, b) panel is the interface region which embraces the Al first layer and the first Zn-O bilayer at the Zn-terminated surface, region c) is relative to the LDOS of a bulk-like Zn-O bilayer in the middle of the ZnO slab and finally in the d) region we show DOS projected on the first Zn-O bilayer at the O-terminated surface. The region of most physical interest is region b), whose LDOS describes the energy spectrum of the surface electrons, while the other three regions serve essentially as a reference. The comparison between Fig. 5.9 and the equivalent LDOS picture obtained for the clean surface of the isolated ZnO slab (Fig. 4.5 in Chap. 4) clearly shows that the DOS characteristics of ZnO in the interface system are almost unchanged with respect to those of the ZnO isolated system. Also for Aluminum, the presence of the interface affects only modestly the LDOS (Fig. 5.10). This observation provides a first important indication that the interaction between the two subsystem, Al and ZnO forming the (0001) interface is small, in the clean ZnO interface case. Looking at Fig. 5.9 one notes that, as expected, the Al/ZnO system becomes metallic because of the Al contribution and for the presence of very low density of metallic states in the gap region induced by Al. These states maintain their bulk-like characters and are evenly distributed. Coming to the ZnO part, see Fig. 5.9 (b-d panels), also for the interface system the typical characteristic of the presence of a strong internal dipole field are still

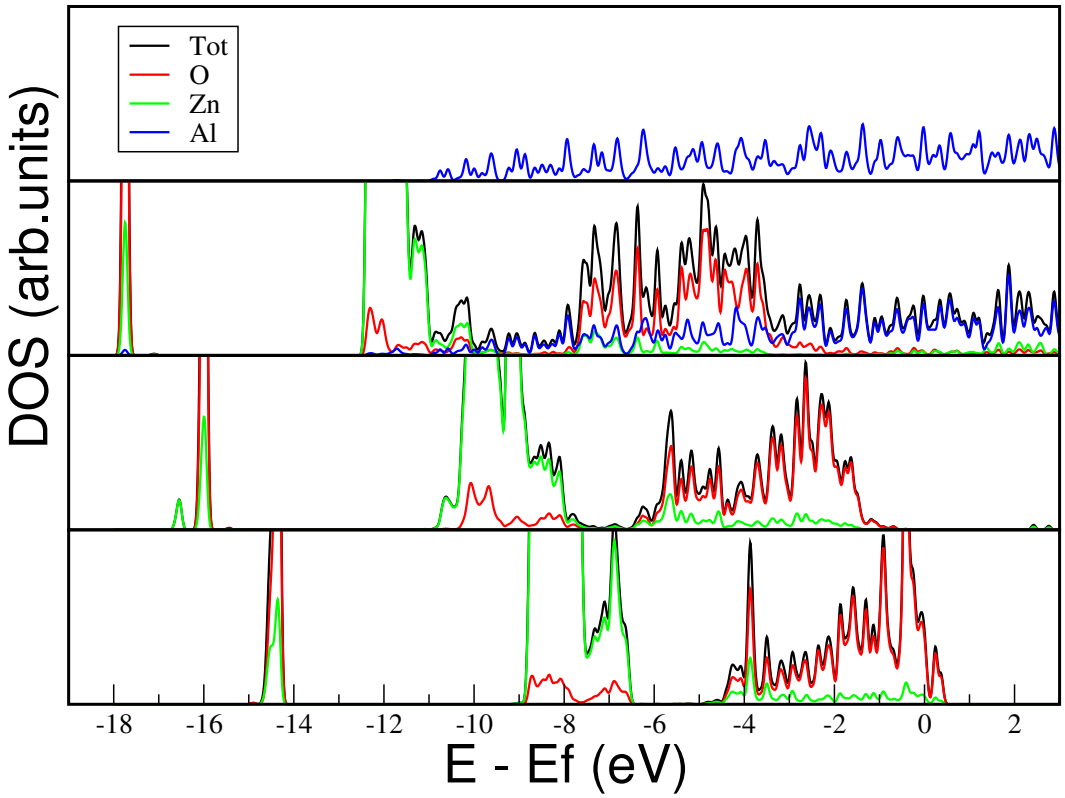

Figure 5.9: Al/ZnO clean free interface, LDOS for four regions: a) Al bulk-like, b) Al first layer and the first Zn-O bilayer at the Zn-terminated surface, c) Bulk-like Zn-O bilayer in the middle of ZnO slab, d) first Zn-O bilayer at the O-terminated surface.

present. Although Al efficiently acts in screening interface charges, as can be inferred from the fact that the interlayer distances at the Zn-terminated surface are somewhat recovering their bulk values (see Tab. 5.1 - first row), the strong charge transfer from the O-terminated free surface is still present and is responsible of both a strong contraction of the surface bilayer and the relatively large DOS at Fermi level (Fig. 5.9 d panel). Thus the slab is still below the effect of a strong electric dipole field as it is reflected also in the shift of the LDOS present in Fig. 5.9, panels b-d. To clarify this point, in comparison with what previously discussed for the clean surfaces (see Fig. 4.5 in Chap.4), in Fig. 5.11 we show the LDOS for the free clean interface along with the macroscopic average of the Hartree potential for this system: it is very interesting to note that the potential drop from one side of the slab to the inner bulk-like region still corresponds exactly to the energy shift of the relative LDOS, although quantitatively this shift is reduced and of opposite

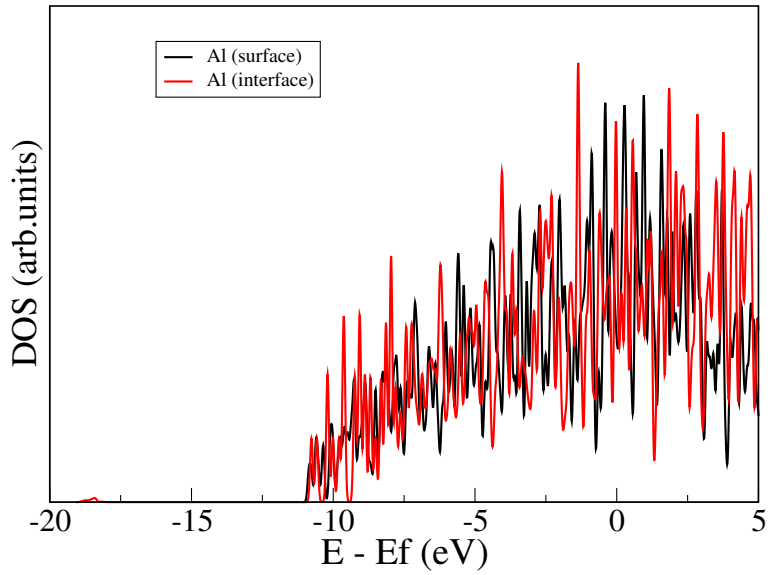

Figure 5.10: DOS Al projection in Al/ZnO (red) vs Al surface isolated system DOS (blue)

sign, with respect to the surface calculation because of the presence of Al.

As it will be shown in Par. 5.3.3, this type of analysis allows to quantify the dipole field effects and then to provide an estimate of its effects in the Schottky barrier calculations.

Vacancy free interface

Now we consider the interface between Al and the ZnO slab with vacancy reconstructed surfaces, whose LDOS is shown in Fig. 5.12. In Chap 4 it was described that vacancy formation is a mechanism for surface charge compensation: this result affects also the interface system. Indeed the LDOS represented in Fig. 5.12 shows that at the Zn side (i.e. the Al/ZnO(0001) interface), the bulk ZnO gap is restored and the surface states related to the presence of vacancies disappear since Al atoms tend to penetrate into the lattice sites left empty by the missing Zn. Furthermore, the presence of Al induces an increased reduction of band displacement from top to central portion of the slab (panels b and c in Fig. 5.12) and in the interlayer deviation from bulk values (Tab. 5.1). This is an indication of a reduction of the dipole field, with respect to the ZnO vacancy compensated surface, as it will be described also in the next section. Another interesting feature of this case is the Fermi level increase toward the ZnO conduction band with respect to the previous clean case (Fig. 5.9). Since this effect is clearly due to the Al

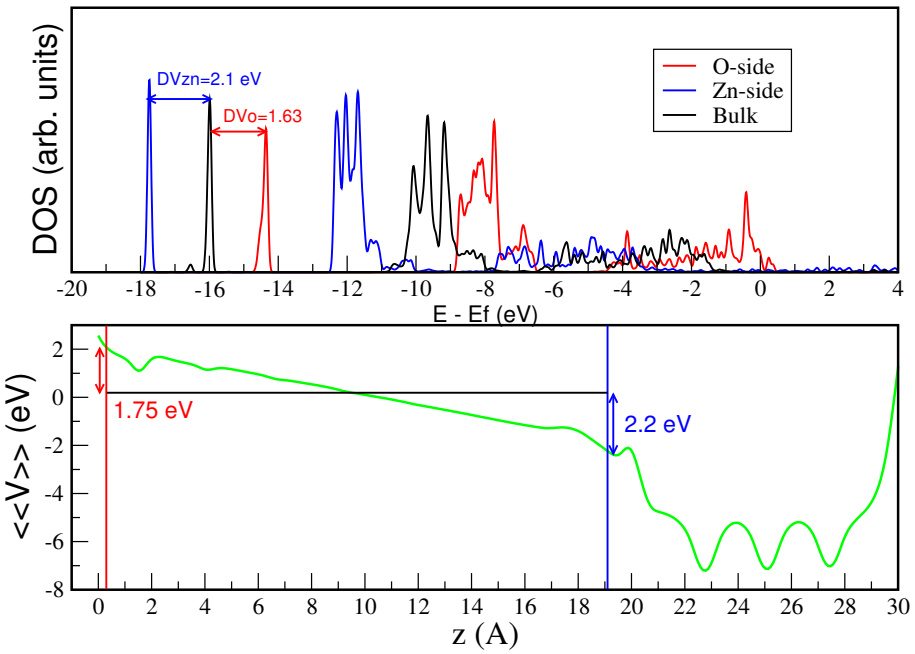

Figure 5.11: Al/ZnO clean free interface: LDOS for Zn and O-terminated surfaces Zn-O bilayer vs bulk-like (top panel) and the potential trend within the ZnO slab (bottom panel). Beyond some correction induced by the presence of the surface, the main contribution to the LDOS shift comes from the potential drop inside the slab, as indicated by arrows.

presence, we explain it in terms of the substitutional Al forming an AZO region at the interface.

Since the Zn vacancy presence is responsible for a deep modification of the interface Al layer, an accurate analysis of Al local density of states for each layer must be performed. Our LDOS analysis emphasizes the typical diffuse contribution of Al from the second to the fourth Al layer, noticed also for all Al layers in the previous clean case. These layers are indeed not involved in structural modification and remain essentially located at the Al ideal positions. As previously discussed (Fig. 5.7), DOS modifications are on the other hand expected from the first Al layer due to the Zn vacancy presence. Fig. 5.13 presents the local density of states of the Al atoms of the first layer close to the ZnO surface (but non-substitutional): this DOS are very different from the typical Al one since some localized contributions are noticed (see also Fig. 5.12, a) and b) panels). In particular the blue line is relative to the substitutional Al atom, while the red one derives from contribution of the first layer Al closer to ZnO slab. As evidenced by charge density plots, these low-energy localized contributions are associated to Al-O

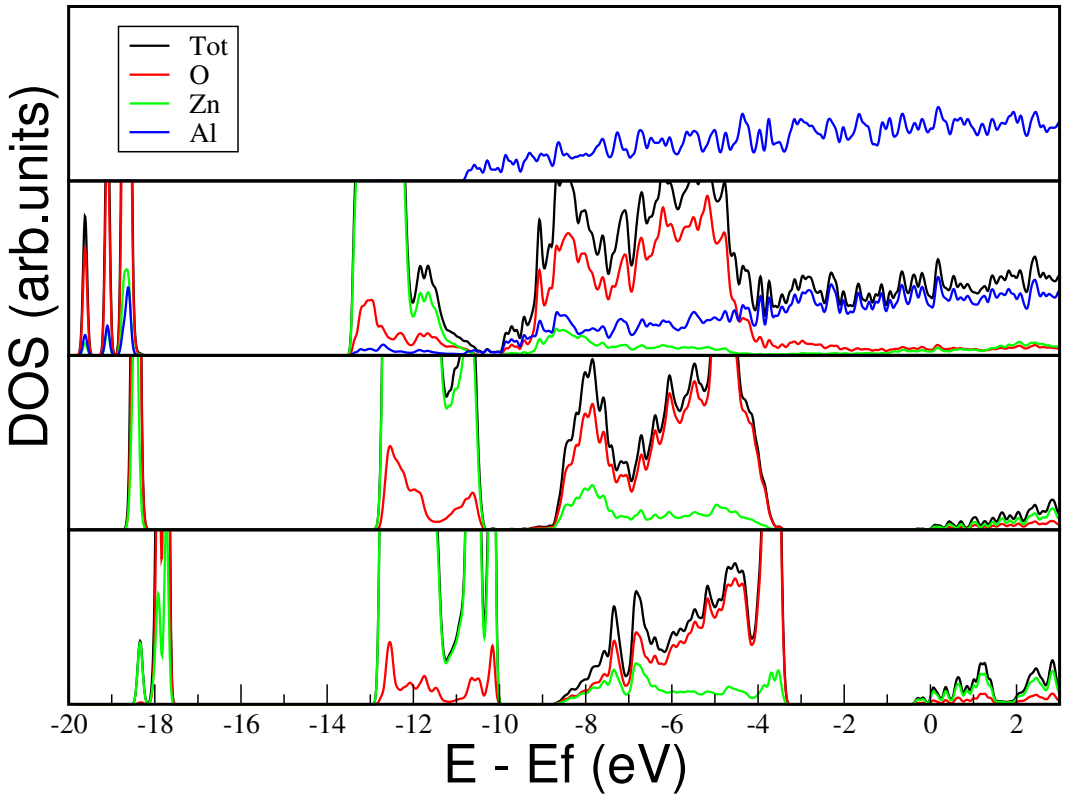

Figure 5.12: Al/ZnO vacancies free interface, LDOS for four regions: a) Al bulk-like, b) Al first layer and the first Zn-O bilayer at the Zn-terminated surface, c) Bulk-like Zn-O bilayer in the middle of ZnO slab, d) first Zn-O bilayer at the O-terminated surface.

interaction and are spatially located mainly on the O atoms. An example of these charge density plots is reported in the inset of Fig. 5.13. This state, due to the bonding between the substitutional Al and the sourrounding Oxygens, is relative to the lowest energy peak of substitutional Al DOS (blue line). The peak relative to the down Al (red line) is instead associated to states spatially located on the O atoms that interact with these Al atoms. This LDOS analysis also provides another important information: the localized contribution in Fig. 5.13 occur at the typical Al-O binding energy of AZO compound (see Chap. 3). This result supports the hypothesis of an AZO interface region formation and of its influence on the presence of interface states in the gap and consequently on SBH.

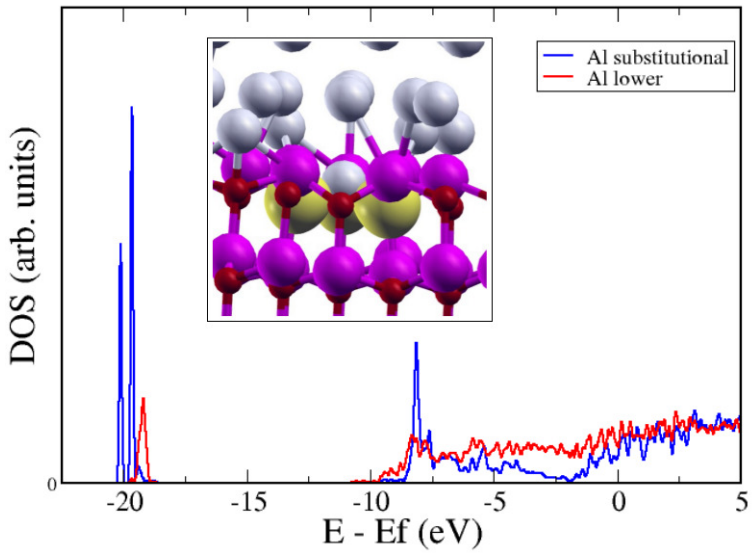

Figure 5.13: Al DOS components of the substitutional Al (blue) and of a first layer Al down to ZnO slab (red). Inset: charge density contour plot of the lowest energy peak in the substitutional Al DOS.

Clean buried interface

Finally we consider the case of the interface between Al and a clean surface ZnO slab without the presence of a vacuum region. In this situation the vacuum absolute reference value, for quantities such as eigenvalues and electronic potential, is lost, but a configuration that allows to study the contact between Aluminum and both ZnO surfaces is reached.

One would expect that this case should be more similar to the clean free interface described previously. Surprisingly the LDOS shown in Fig. 5.14, exhibits several analogies with the just discussed vacancy free interface case. In fact, if compared with Fig. 5.9, the reduction of the shift between LDOS projection on outermost ZnO layers with respect to ZnO bulk, attributed to the internal dipole field (see Chap. 4 and discussion below) is evident, along with the absence of surface states in the ZnO gap region. This field reduction is due to Aluminum that, in this case, can interact also with the O-terminated ZnO surface, providing charge screening and stabilization. This aspect can be understood from the comparison between the first and last row of Tab. 5.1 that confirms the strong reduction of about 50 % of Zn-O distance which vanishes when O-terminated surface is in contact with the Al slab. This interaction is responsible, also in this case, for the Fermi level increase in the ZnO gap region: as in the vacancy case, this effect is due to the interaction between Aluminum and Oxygen. However in this case the involved O atoms

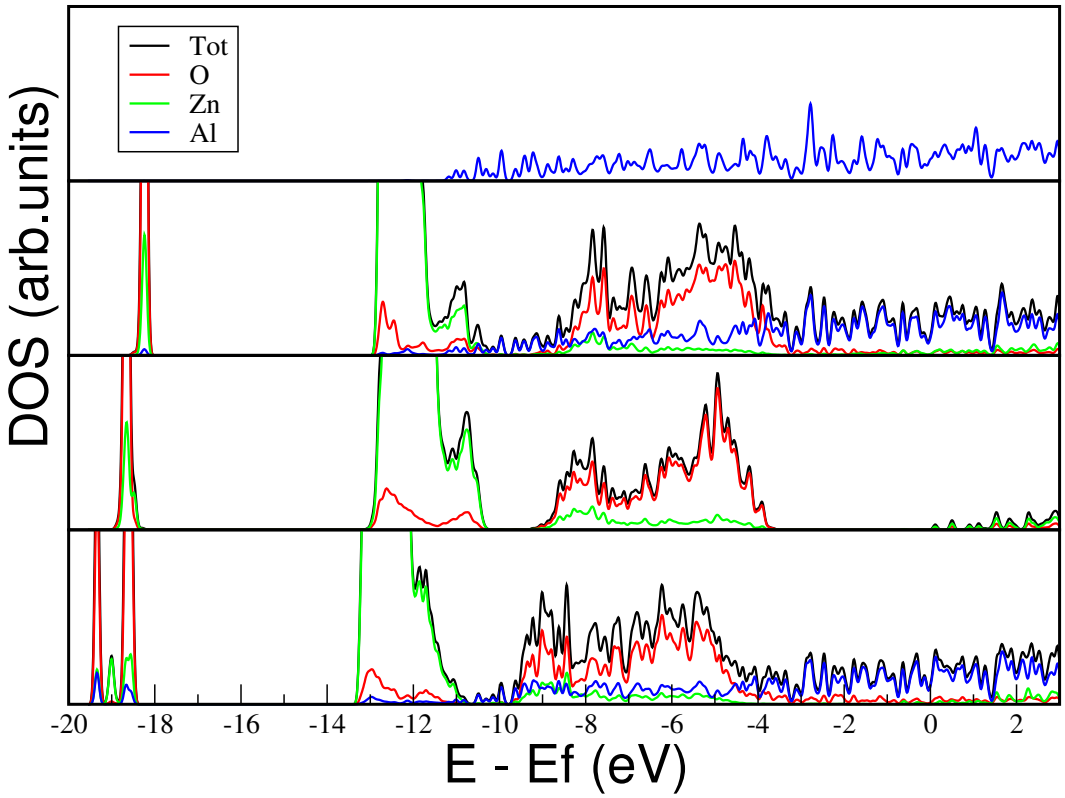

Figure 5.14: Al/ZnO clean buried interface, LDOS for four regions: a) Al bulk-like, b) Al first layer and the first Zn-O bilayer at the Zn-terminated surface, c) Bulk-like Zn-O bilayer in the middle of ZnO slab, d) first Zn-O bilayer at the O-terminated surface.

are those of the O surface.

From the analysis of the electronic properties of these different systems, we can draw the following conclusions:
i) for clean surfaces, in the presence of vacuum, Al and ZnO are poorly interacting and the relative LDOS quickly recovers the respective bulk-like properties immediately away from the interface; the ZnO dipole field is poorly affected by the presence of Aluminum, as seen in the large displacement of the LDOS for outermost ZnO bilayers with respect to the inner portion of the slab
ii)when Al can form bonds with O, on the contrary, either through substitutional sites (vacancy free case system) or when forming an Al-O interface (buried interface calculation), it acts as a donor, as in AZO: the induced screening effect is responsible for a suppression of the internal ZnO dipole

field and a Fermi level shift.
We will see in the following how these different contributions affect the Schottky barrier between Al and ZnO.

5.3.3 Al/ZnO Schottky barrier

In this section we will provide an estimate of the Schottky barrier height for the Al/ZnO contact. The previous analysis allowed to point out the effects of the ZnO macroscopic dipole field: here this contribution will be considered to quantify its influence on the interface potential. Fig.5.15 (left panel) shows

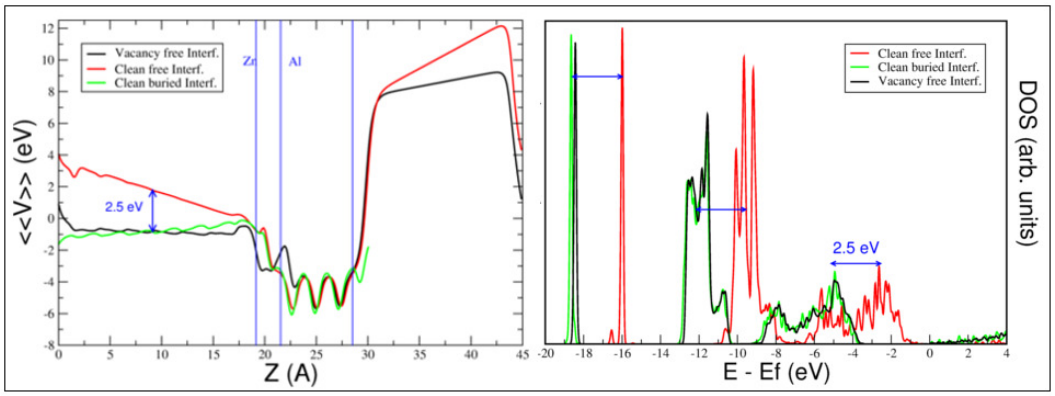

Figure 5.15: LDOS relative to the bulk region of the ZnO slab for each supercells (right panel) and supercells potential trend aligned to Al slab value (left panel).

the Al/ZnO macroscopic average potential (see Par. 5.2) trend accross the supercell for the three considered cases. The vertical lines separate the three regions of the supercell: the ZnO, the Al slab and the vacuum region. Since a vacuum region is not present in all the three supercells and a common reference level for the potential can not be given, we chose to align the three potentials in the Al bulk region (the center of the Al slab). This choice allows for a better comparison with experimental data. Looking at the ZnO slab region the dipole field effects described in the electronic property section are clearly visible: focusing on clean and vacancy free interface (red and black line respectively), we notice the sensible reduction of the slab field already discussed in the previous chapter (Chap. 4) due to the vacancy superficial charge reduction. In both cases, however, the Aluminum screening effect at the Zn side further modifies the potential behaviour visible as further reduction of the potential difference between the two slab sides with respect to the ZnO isolated slab (see Chap. 4). The largest contribution to this reduc-

tion comes from the outermost Zn bilayer, where the interface is built, as detectable also for example by inspection of the first two rows of Tab. 5.1: the surface bilayer stress (a surface field marker) of the O-side are in fact the same with respect to the ZnO slab without Al contact (Tab. 4.1, Chap. 4), while for the Zn side, the strong bilayer contraction of Tab. 4.1 is removed because of Al screening. When the vacuum region is removed and a further interface at the O-terminated side is built with strong Al-O interaction (clean buried interface), the features of the potential change again (green line) and a variation in potential intensity and slope occurs: even if the ZnO surfaces are clean, a strong reduction in the ZnO potential is noticed as a consequence of Al screening. In this situation both surfaces are stabilized as evidenced by the absence of stress in Tab. 5.1 (third row).

Now we focus on how these ZnO potential differences can affect the interface potential barrier. Fig. 5.15 (left panel) shows that the potential drop at the interface is about the same in each case, but the ZnO bulk potential value for the clean free interface case is shifted up of about 2.5 eV. This shift is only due to the stronger dipole field as evidenced by the LDOS relative to the ZnO slab bulk region for each case (right panel): the clean case LDOS shift is indeed exactly the same bulk potential difference noticed in the top panel. Since in the standard Schottky barrier height calculation procedure the potential difference between metal and semiconductor is calculated in the respective bulk region, the strong dipole field in the clean free interface case inevitably influences SBH calculation.

Thus Fig. 5.15, clearly demonstrates that the field does not heavily influence the interface details but introduces a potential shift between the different regions of the slab, whose effects must be taken into account in order to correctly estimate SBH, strongly dependent on the potential alignment.

After providing a description and a quantification of the dipole field influence, now we address on the main target of this chapter: the calculation of the Schottky barrier for the Al/ZnO contact.
In Tab. 5.2 our results, both for n-type and p-type SBHs, are shown: in principles, from a DFT calculation the better way to define SBH is to evaluate what is generally called SBH_p that is for p-type charges, since DFT is an exact theory of the ground state, thus ground state properties, such as bound (Valence band) are properly described, whereas in the experiments, the n-type barrier is typically measured since ZnO is n-doped, as grown. The Schottky barrier height calculation consists in an alignment process between the valence and conduction bands of the semiconductor and the Fermi level of the metal as described in Par. 5.2; this band alignment process is schematically represented in Fig. 5.16. For the SBH values in Tab. 5.2 we used Eq.

	$\bar{\bar{V}}_{Al}$	$\bar{\bar{V}}_{ZnO}$	ϕ_p	ϕ_n
Clean free int.	-6.23 eV	0.075 eV	1.02 eV	2.2 eV
Vacancies free int.	-4.6 eV	-0.84 eV	3.58 eV	-0.28 eV
Clean buried int.	-0.27 eV	3.43 eV	3.6 eV	-0.3 eV

Table 5.2: Macroscopic potential average values in Al (first column) and ZnO (second column) portions of the interface system and the calculated p and n-type Schottky barrier height (third and fourth column respectively)from Eq. 5.1.

5.1 that includes both bulk and interface components. Bulk alignment values (the ZnO valence band top and the Al Fermi level related to their macroscopic average potentials), obtained from the individual bulk systems are shown in Fig. 5.16. The relative interface potential values are instead shown in the first two columns of Tab. 5.2. From these values we obtain from Eq. 5.1 the SBH indicated in the last two columns of Tab. 5.2. Focusing on the n-type SBH values (fourth column), that can be directly compared with experiments, there is a considerable discrepancy between the clean free interface case and the other two. Since, as shown in Fig. 5.15 (left panel), the potential drop at the interface is about the same in all cases, the disagreement is due to the dipole field effect described above, that shifts the bulk region potential of about 2.5 eV (see Fig. 5.15). Indeed, by subtracting this value from the clean SBH, we obtain a value of about 0.3 eV in agreement with the other two cases. This value, in very good agreement with both some experimental data and other preliminar theoretical work [35], confirms the Ohmic character of the Al/ZnO contact highlighted also by the structural and electronic properties analysis. We remind that the experimental scenario is still controversial, and the formation of Ohmic contacts is assigned to defects and/or Al interdiffusion, a panormama which is rather close to the present description.

Beyond the SBH numerical value provided the most important conclusion of this work concerns the importance of the interface microscopic details and how to relate theoretical calculations to experiments. In particular our results highlight the importance of the relative contributions, the band term (bulk) and the interface part, as sketched in Fig. 5.17. For selected interfaces, particularly when large dipole fields and/or atomic interdiffusion take place as in the case of vacancy stabilized interfaces presented here, the interface term cannot be neglected.
In recent years this argument is gaining increasing importance, expecially from the experimental indications [5,39], given by the failure of the theoret-

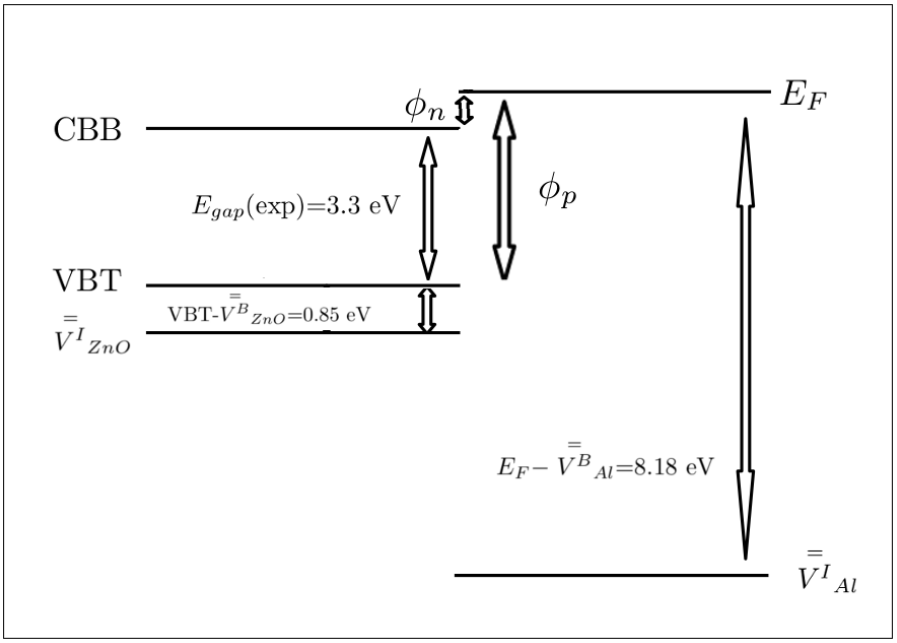

Figure 5.16: Sketch of the Al/ZnO contact band alignment.

ical models in predicting the contact type for several metal/semiconductor pairs.

5.4 Conclusions

In this work an ab initio DFT investigation of the structural and electronic properties of the Al/ZnO interface was performed. For the first time the Al/ZnO Schottky barrier was calculated on a reduced mismatch system, taking into account the macroscopic dipole field effects, adapting well-established methods to the present case.

The most important result of this work concerns the importance of the interface microscopic details and its strong influence on SBH definition in agreement with most recent experimental data. As demonstrated, if a mesoscopic characterization for SBH is provided (determined only on bulk properties), a Schottky like contact is obtained, while focusing on the interface layers, thus giving a microscopic description of the contact, the contact nature seems to be Ohmic.

Another important result regards the interaction between Al and ZnO and

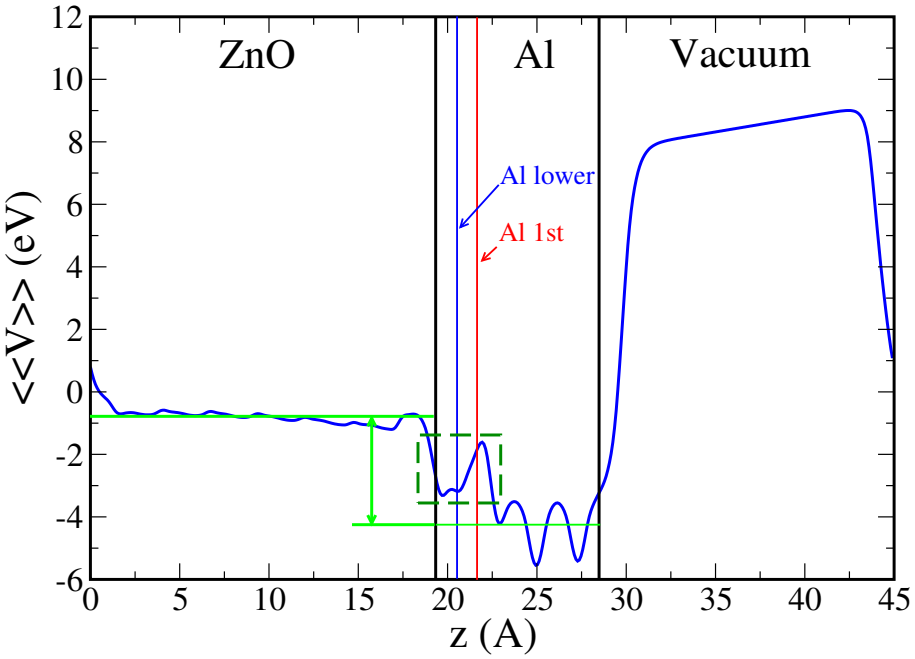

FIGURE 5.17: Macroscopic potential average for vacancy free interface case: Mesoscopic (light green references) and microscopic (dark green dashed square) SBH definitions.

the related effects on the electronic properties: in the clean free interface Al and ZnO are poorly interacting recovering the respective bulk-like properties immediately away from the interface. On the contrary, when Al can form bonds with O (either through substitutional sites as in the vacancy free case system or when forming an Al-O interface as in the buried interface calculation), it acts as a donor, as in AZO.
The formation of this sort of AZO buffer layer is responsible for the screening of the ZnO internal macroscopic field and Fermi level shift, leading to Ohmic contacts.

Bibliography

[1] Jiming Bao, Mariano A. Zimmler, and Federico Capasso NANO LETTERS Vol. **6**, No. 8 1719-1722(2006)

[2] D. C. Look, Mater. Sci. Eng. B **80**, 383 (2001).

[3] F. Tuomisto, K. Saarinen, D. C. Look, and G. C. Farlow, Phys. Rev. B **72**, 085206 (2005).

[4] M. Lazzarino, G. Scarel, S. Rubini, G. Bratina, L. Sorba and A. Franciosi C. Berthod, N. Binggeli, and A. Baldereschi Phys. Rev. B **57**, 16 (1998)

[5] M.W. Allen and S. M. Durbin Phys. Rev. B **82** 165310 (2010)

[6] C. Berthod, N. Binggeli and A. Baldareschi, Phys. Rev. B **68** 085323 (2003)

[7] A. Ruini, R. Resta, S. Baroni, Phys. Rev. B **56**, 23 (1997)

[8] Y. Dong, Z.-Q. Fang, D. C. Look, G. Cantwell, J. Zhang, J. J. Song, and L. J. Brillson, Appl. Phys. Lett. **93**, 072111 (2008).

[9] H. Frenzel, A. Lajn, M. Brandt, H. von Wenckstern, G. Biehne, H. Hochmuth, M. Lorenz, and M. Grundmann, Appl. Phys. Lett. **92**, 192108 (2008).

[10] Leonard J. Brillson and Yicheng Lu J. Appl. Phys. **109**, 121301 (2011)

[11] C. A. Mead in *Ohmic Contacts to Semiconductors*, edited by B. Schwartz, (Electrochem. Soc., NY, 1969).

[12] C. A. Mead, Solid-State Electron. **9**, 1023 (1966).

[13] W. E. Spicer, P. W. Chye, P. R. Skeath, C. Y. Su, and I. Lindau, J. Vac. Sci. Technol. **16**, 1422 (1979).

[14] L. J. Brillson, Surf. Sci. Repts. **2**, 123 (1982).

[15] W. Schottky, Phys. Z. **41**, 570 (1940).

[16] N. Mott, Proc. Cambridge Philos. Soc. **34**, 568 1938.

[17] J. Bardeen, Phys. Rev. **71**, 717 (1947)

[18] V. Heine, Phys. Rev. **138**, A1689 (1965).

[19] J. Tersoff, Phys. Rev. Lett. **52**, 465 (1984).

[20] W. Monch, Phys. Rev. Lett. **58**, 1260 (1987).

[21] H. Luth, *Surfaces and Interfaces of solids*, Springer-Verlag (1992)

[22] L. J. Brillson, Surf. Sci. Repts. **2**, 123 (1982).

[23] J. Uhlrich et al. J. Phys. Chem. C **113**, 21147 (2009)

[24] L. J. Brillson et al. Appl. Phys. Lett. **90**, 102116 (2007)

[25] L. J. Brillson, Phys. Rev. Lett. **40**, 260 (1978).

[26] O. Kubachewski, C. B. Alcock, and P. J. Spencer, *Materials Thermochemistry* (Pergamon, Oxford, 1993).

[27] D. D. Wagman W. H. Evans, V. B. Parker, I. Halow, S. M. Bailey, and R. H. Schumm, *Selected Values of Chemical Thermodynamic Properties*, National Bureau of Standards Tech. Notes 270-3-270-7 (U. S. GPO, Washington, D.C., 1968-1971).

[28] H. K. Kim, K. Kim, S. Park, T. Seong, and I. Adesida, J. Appl. Phys. **94**, 4225 (2003).

[29] H. K. Kim, T. Y. Seong, K. K. Kim, S. J. Park, Y. S. Yoon, and I. Adesida, Jpn. J. Appl. Phys. **43**, 976 (2004).

[30] H. K. Kim, and J. M. Lee, Superlattices Microstruct. 42, 255 (2007).

[31] J. H. Kim, J. Y. Moon, H. S. Lee, W. S. Han, H. K. Cho, J. Y. Lee, and H. S. Kim, Mater. Sci. Eng. B **165**, 77 (2009)

[32] Paolo Giannozzi, Stefano Baroni, Nicola Bonini, Matteo Calandra, Roberto Car, Carlo Cavazzoni, Davide Ceresoli, Guido L Chiarotti, Matteo Cococcioni, Ismaila Dabo, Andrea Dal Corso, Stefano de Gironcoli, Stefano Fabris, Guido Frates, Ralph Gebauer, Uwe Gerstmann, Christos Gougoussis, Anton Kokalj, Michele Lazzeri, Layla Martin-Samos, Nicola Marzari, Francesco Mauri, Riccardo Mazzarello, Stefano Paolini, Alfredo Pasquarello, Lorenzo Paulatto, Carlo Sbraccia, Sandro Scandolo, Gabriele Sclauzero, Ari P Seitsonen, Alexander Smogunov, Paolo Umari and Renata M Wentzcovitch, J. Phys.: Condens. Matter **21**, 395502 (2009). See also `www.quantum-espresso.org`.

[33] J. P. Perdew, K. Burke, and M. Ernzerhof, Phys. Rev. Lett. **77**, 3865 (1996).

[34] D. Vanderbilt, Phys. Rev. B **41**, R7892 (1990).

[35] Y. Dong and L.J. Brillson, Journal of Electronic Materials, **37**, 5, (2008)

[36] M Peressi, N Binggeli and A Baldereschi J. Phys. D: Appl. Phys. **31** (1998) 1273-1299.

[37] A. Baldereschi et al. Phys. Rev. B **69**, 035320 (2004)

[38] J. Von Pezold, P. D. Bristowe Journal of Materials Science **40**, 3051 (2005)

[39] S. Picozzi et al. Phys. Rev. B **65**, 165316 (2002)

Chapter 6

Conclusions

This thesis is part of a broad effort aimed at gaining a better description of the active elements in functionalized nanostructures for energy applications, and a deeper understanding of charge and energy transfer mechanisms in these complex systems. In particular this work focused on AZO, recently proposed for interesting photovoltaic applications, and on the Al/ZnO interface since Metal/ZnO contacts are central to all ZnO electronic devices. Beside the fundamental interest in the challenging topics related to material science and nano structures, the control of the interactions at these interfaces offers a unique opportunity to unravel the interplay between structures and functionalities of increasing complexity and technological relevance.
Our approach is based on ab initio Density Functional Theory (DFT) simulations and it consists in focusing on relevant microscopic properties and processes that characterize the fundamental building blocks of ideal structures and interfaces.

The first target of this work was to address the Al doped ZnO issues (AZO). This was a very challenging aim not only because it is commonly recognized that doping of oxides is a complex problem, but mainly because its optical, electrical, structural and mophological properties are essential in determining performances in optoelectronic devices. Although AZO films have been successfully grown, the local geometry of the Al inclusion, the diffusion mechanisms, and the electronic properties of the system are still completely non characterized.
Our first principle results on AZO allowed us to characterize at the microscopic level the TCO properties, taking into account the interplay between the electronic and structural properties of the system and demonstrate the detrimental role of interstitials.
Our investigation provide also an important preliminary modeling of the Al diffusion mechanisms on ZnO substrate, completely missing in literature.

The second important goal of this work was the study of the ZnO polar surface stabilization. This problem, still controversial, was in fact mandatory to correctly approach the Al/ZnO interface investigation, since the ZnO macroscopic polarization, and the very many surface reconstructions and local dipole fields play a critical role.
We address the problem by means of ab initio DFT calculations. The original contribution of our investigation was to provide a comprehensive electronic analysis for several reconstructions considered to stabilize polar surfaces.

Finally, the main target of the PhD project, the Al/ZnO interface, was addressed. Metal/ZnO interface is central to all ZnO electronic devices, however, the discrepancy with experiments indicates that interface features such as surface contamination, interface native defects, chemical bonding etc. play a very important role which is even more relevant for nanostructures, where the surface-to-volume ratio is more important.
In order to determine the Ohmic vs Schottky contact behaviour and to provide a structural and electronic characterization still lacking, we performed an ab initio simulation of the Al/ZnO interface. Our investigation is particularly important since, for the first time, the Al/ZnO Schottky barrier was calculated on a reduced mismatch system, taking into account the macroscopic dipole field effects adapting the well-established methods to the present case. Our results highlight the Ohmic character of the contact, clearly showing the strong influence of the interface microscopic details on the barrier height calculation.

Chapter 7

Acknowledgements

I would like to give my first thanks to CINECA for the PhD grant and for the computer time, provided through a series of ISCRA grants. I would like to thank CINECA hpc staff and in particular Carlo Cavazzoni for the specialistic support and availability.

I would like to thank Alessandra Catellani and Davide Cassi for the support throughout my Ph.D program and for their precious contribution to my work and to my professional growth.

I would like to thank Arrigo Calzolari for support and insightful discussions.

A special thanks goes to the CNR-IMEM institute, we hosted me during this period, also providing fundings for my activity, through e.g. the CariTRO-DAFNE project.

Chapter 8

Publications

- M. Bazzani, A. Neroni, A. Calzolari and A. Catellani, Appl. Phys. Lett. 98 121907 (2011).
- Arrigo Calzolari, Mirco Bazzani, and Alessandra Catellani, *Dipolar and charge transfer effects on the atomic stabilization of ZnO polar surfaces* , Phys. Rev. B. submitted
- A. Catellani, M.Bazzani and A. Calzolari, *Optoelectronic properties of Al:ZnO: critical dosage for an optimal transparent conductive oxide*, Scienza e Supercalcolo, Monografia biennale sulle attivitÃ di ricerca del Cineca, pubblicazione con codice ISBN;
- M. Bazzani, A. Catellani, Report ISCRA Class C Project "Electric field effect in low dimensional ZnO structure";
- A. Catellani, M. Bazzani, A. Neroni, Report ISCRA Class C Project "Dopant diffusion in Oxide Semiconductors".
- A paper on the structural and electronic properties of the Al/ZnO interface is in preparation.
- A paper on the Al diffusion mechanisms on ZnO is in preparation.

Appendix A

Reports of the different projects submitted to CINECA to obtain computer time

Italian SuperComputing Resource Allocation ISCRA

Class B Project Report

Objectives

This project, focused on the study of electronic and optical properties of Aluminum-doped Zinc Oxide (AZO), is part of a larger research activity concerning characterization and modeling of III generation photovoltaic ZnO nanowire-based solar cells (DSSCs) [1], where AZO films have been recently proposed as optimal choice as Transparent Conductive Oxides (TCOs) substrates/films. The idea of combining nanostructures and TCO should improve efficiency in charge transport, reducing the resistance between ZnO and the TCO contact. Although AZO films have been successfully grown, the local geometry of the defect, the diffusion mechanisms, and the electronic properties of the system are still poorly characterized. In addition, from the purely theoretical point of view the remarkable combination of conductivity in an albeit wide-gap (i.e. transparent) material [2], as well as the study of complex oxides that involve d-states (often in presence of spontaneous polarization fields) [3], are still the subjects of intense debate. Hence, a full understanding of the formation, and stability of TCOs still constitutes a fundamental challenge and a technological goal.
The scientific aims of the present project was therefore to provide a microscopic description of electronic and optical properties of Aluminum-doped Zinc Oxide in order to discriminate the ideal Al content for an optimal TCO behavior. in terms of transparency (optical gain), with minimal lattice distortion and structural defects, while increasing charge mobility. Our aim was therefore to perform first principles investigations of Al doped ZnO, because this method offer the unique possibility of characterizing the optoelectronic properties of TCO at an atomistic level, taking directly into account the interplay between the electronic and structural properties of the system.
In this way the first target of the present project was to investigate how doping affects electronic and optical properties of AZO up to the experimental solubility limit, considering the details of neutral substitutional Aluminum at Zinc site. According to thermodynamic considerations, this kind of doping mechanism is indeed the most probable for low Al concentration.
The second project aim was devoted to high doping regimes: we considered the possibility of other kind of defect formation, such as interstitial and clustering, on the basis of recent transport experimental data [4] showing non-monotonic variations in AZO electronic properties (unexpected deterioration of mobility) increasing dopant concentration.
From the computational point of view the oxide doping problem is very demanding due to the systems large size required to simulate low doping regimes in the presence of Zn d-states and by the need of reiterated DFT calculations to explore different atomic configurations.
In addition to the ambitious aims mentioned, this project was also important as a starting point for the characterization of the interface between ZnO nanostructures and AZO substrate, involved in photovoltaic devices described above, that is the scope of newest calculations through further ISCRA B project now in progress.

[1] M. N. E. M. S Tricot, C Boulmer-Leborgne and J. Perriμere, J. Phys. D: Appl. Phys. 41, 175205 (2008).
[2] S. Lany and A. Zunger, Phys. Rev. B 78, 235104 (2008).

[3] A. Janotti, D. Segev, and C. G. Van de Walle, Phys. Rev. B 74, 045202 (2006).
[4] K.-M. Lin, Y.-Y. Chen, and K.-Y. Chou, J. Sol- Gel. Sci. Technol 49, 238 (2009).

Achievements

The scientific goals of the present project focused on the fully characterization of the electronic and optical properties of Aluminum doped ZnO by means of ab initio simulations: we performed density functional total-energy-and-force calculations as implemented in the Quantum Espresso package with PBE generalized gradient approximation and ultrasoft pseudopotentials. The inclusion of the semicore 3d shell of Zn in the valence shell and the large cell size required to simulate low doping regimes, made the project challenging, while the publication of recent experimental results on similar systems rendered it also particularly timely.
AZO bulk systems were simulated by periodic supercells, multiples of the undoped ZnO lattice parameters, with different amount of substitutional Al to reproduce different doped system in the range of 0-3.2%. Clustering and interstitial defects at the same high (3.2%) Al content were also considered, to suggest a possible explanation for the detrimental effect on the optoelectronic properties at high doping concentration, revealed by recent transport experiments. For all systems, structural relaxation was performed and terminated when the magnitude of the Hellmann–Feynman forces on each ion was less than 0.03 eV/Å. The AZO optical properties were studied calculating the imaginary part of the dielectric function (absorption spectrum), without the electron-hole interaction. A Hubbard correction to improve the bandgap and the position of Zn-d bands was included in the calculations: the U term was optimized through numerical fit to optimize the description of p – d interaction and to correctly describe the optical spectra.
Our results, allowed us to describe the electronic properties of AZO as a function of the percentage of Al and of the different doping mechanisms, through bands and density of states analysis: at low dosages doping is not associated with the inclusion of defect states in the pristine ZnO gap that remains almost unchanged. Al electrons are fully donated to the system as additional free charge: the effect is reflected in a mere shift of the Fermi level up in the conduction bands that increases with Al percentage increasing.
From the optical point of view, the dielectric function spectra show a strong blue shift of the absorption edge for substitutional AZO (explained in terms of the Burnstein-Moss effect) and the absence of peaks associated to Al, confirming that Al low dosage doping preserve ZnO transparency in the visible range, as required for a good TCO. On the contrary, at high Al content, the simulation of interstitial defects shows completely different characteristics: additional almost dispersionless localized filled states appear in the pristine ZnO gap: these states, acting as optical traps, are characterized by large effective masses and low electron mobility.
Our calculations allowed us to highlight an optimal TCO behavior for AZO below solubility limit, above which the presence of interstitial Al defects is responsible for the degradation of AZO optoelectronic pointed out by the most recent transport experiments.
The results of this project have been published in a JCR journal [1], and presented in a number of international conferences.

[1] M. Bazzani, A. Neroni, A. Calzolari and A. Catellani, Appl. Phys. Lett. 98, 121907 (2011).

Italian SuperComputing Resource Allocation ISCRA

Class C Project Report

Objectives

The purpose of this ISCRA C project is to perform a series of preliminary tests on Zinc Oxide (ZnO) polar surfaces, to evaluate the optimal solution to be adopted in subsequent calculations. The solution must be a compromise choice, since it must be computationally feasible although physically meaningful. The problem arises because ZnO is a polar compound, that crystallizes in a low symmetry lattice, the wurtzite crystal structure: along the polar direction, namely along the stacking c axis in the lattice, usually defined as (0001) direction, the alternating planes are either Zn or O terminated. This implies that when the bulk structure is cut perpendicular to the polar axis one obtains positively charged Zn-(0001) and negatively charged O-(000-1) surfaces, resulting in a normal dipole moment, which diverges as the system thickness increases, as well as the surface energy. This means that these ideally cut surfaces are unstable [1]: thus cut, the material slab presents a non-vanishing surface dipole associated to an electrostatic potential that is responsible for charge transfer from one surface to the other. Exposed polar surfaces experience indeed a number of different, long-range reconstructions [2], defects or adsorbates [3] that allow to minimize charge transfer and regain surface stability. Computationally, the problem is not addressable in plane-wave methods that impose periodic boundary conditions on the electrostatic potential [4]. For this reason, from a theoretical point of view, these surfaces still represent a formidable challenge in surface science. In particular, thorough tests on the best numerical approach are mandatory.
Our goal is therefore to perform calculations that allow to stabilize the ZnO polar surfaces by addressing both physical and numerical problems, and obtain the best numerical parameters to simulate a realistic physical system, that will be studied in a followup of the present project.
In this light, different compensations of ionic excess charge mechanisms are tested: the configurations include surface defects such as Zn and O vacancies, adsorption of oxygen atoms or neutral OH groups. In particular, in order to completely characterize the problem, the dipole dependence on slab size and k-point sampling will be considered. Artificial field effects will be also taken into account, using the dipole field correction as implemented in the Quantum-Espresso suite [5]. All these different possibilities tend to reduce the supercell potential jump at the supercell boundaries: the one that allows to obtain the smallest field in the smallest supercell will be chosen as optimal for subsequent large scale calculations. These issues represent an important topic in very demanding system with large size (~200 atoms, 1800 electrons, due to the presence of Zn d-states) as in our case.

Related Publications

[1] C. Noguera, J. Phys. Condens. Matter 12 (2000) R367–R410.
[2] G. Kresse, O. Dulub and U. Diebold, Phys. Rev. B 68, 245409 (2003)
[3] C. Woll, Progr. Surf. Sci. 82, 55-120 (2007)
[4] L. Bengtsson Phys. Rev. B 59, 19 (1999).
[5] P. Giannozzi et al. J. Phys. Condens. Matter 21, 395502 (2009).

Achievements

The results obtained in this project made it possible to completely characterize the numerical issues associated with ZnO polar surfaces stabilization, highlighting the microscopic details linked to the charge rearrangement process involved in dipole field quenching (charge transfer mechanism). All calculations are based on density-functional theory (DFT) within the generalized gradient approximation (GGA) using the plane-wave pseudo-potential method as implemented in Quantum-Espresso suite.
The most common stabilization mechanisms of ZnO polar surfaces were considered and compared, in terms of dipole field drop within supercell, such as vacancies introduction and OH group absorption on polar surfaces. The different surface terminations were compared in terms of charge transfer, ionization potential at the different slab surfaces and surface formation energy. Through structural optimization (terminated when the magnitude of the Hellmann–Feynman forces on each ion is less than 0.03 eV/A) the reference dipole field for clean surfaces was obtained, to compare with the different stabilization solutions subsequently considered. Relax of ideally truncated surfaces are compared to calculations for vacancies and OH groups (one every four superficial atoms and 1/2 monolayer respectively, to compensate the superficial charge excess) in order to test their stabilizing effect compared to clean case. The dipole field trend, obtained from macroscopic average [1], shows that the reduction of surface charge introduced by defects and reconstructions better reduces the dipole field inside the slab, as expected.
Since the slab thickness influences the intensity of the dipole strength because the charge transfer can occur in different ways depending on the slab size and length, each reconstruction considered was tested for several number of bilayer along the polar direction, up to twelve, a number more than satisfactory for studying the effects of interest.
The introduction of an external compensation field, as implemented in QE suite, is also considered in order to prevent the artificial field arising given by supercell periodic boundary conditions: this routine that applies a counter field in the vacuum region which intensity is equal to that generated by surface charges, is designed to completely cancels the artificial field in the vacuum region without introducing any appreciable effect on the slab potential, so it can be used in conjunction with reconstructions to reproduce experimental conditions in which vacuum vanishing field is required.
Finally for all described configurations, dipole dependence on k-point sampling was considered, testing possible differences between uniform mesh and special k-point. In this regard, some anomalies were noted in the calculation of the counter field as properly reported in the description of the dipfield routine. Further tests would be necessary to fully take advantage of the reoutine, in particular for k-point dependence.
All these preliminary tests allowed us to find the optimal numerical setup to correctly model ZnO polarization effects and to choose the most suitable stabilization mechanism to simulate a metal/ZnO (0001) interface, that will be the scope of forthcoming calculations (an ISCRA B project is in preparation).

[1] M Peressi, N Binggeli and A Baldereschi J. Phys. D: Appl. Phys. 31 (1998) 1273–1299.

Italian SuperComputing Resource Allocation ISCRA

Class C Project Report

Objectives

The purpose of this ISCRA C project was to perform a series of preliminary tests on Aluminum incorporation in Zinc Oxide (ZnO), to evaluate the optimal set of computational parameters to be adopted in subsequent calculations: indeed, Al is a typical dopant for the realization of ZnO based TCOs [1]. These tests are mandatory because the oxide doping problem is very demanding from a computational point of view, due to the systems large size required to simulate low doping regimes; the presence of Zn d-states and polar low symmetry lattice render even more cumbersome the calculations.
Notwithstanding the increasing technological interest, the electronic properties of these complex systems have only recently been explored in detail, and the role of surface contamination and interdiffusion at the metal/oxide interface, interface native defects, chemical bonding or other extrinsic factors are far to be fully understood [2-3]. During the last year, we have characterized the electronic and structural properties of bulk Aluminum doped ZnO (AZO) compounds via ab initio simulations, within the ISCRA project AID. The results have been published in Ref [4] and presented in international conferences.
The next step planned was therefore to extend these results providing a full description of the role of Al impurities in ZnO, studying the mechanisms for surface and subsurface incorporation and diffusion of Al in the ZnO crystal. In this way the central issue of the present project was the optimization of all the computational aspects for subsequent large system calculations that will be subject of a forthcoming ISCRA B. In particular we intend to study in the forthcoming project the diffusion of Al ion along different paths in bulk and at surfaces, probing both polar and non polar directions in order to evaluate non uniformities in dopant incorporation (induced by the spontaneous polarization field). These differences are important to correctly model ZnO nanostructures such as nano-wires that grow along the polar axis and present non-polar surfaces.
In order to achieve these goals, we performed ab initio calculations of energy barriers for Al adsorption in ZnO using the PWscf code, based on Density Functional Theory. PWscf includes the NEB algorithm [5], with climbing the image (CI) and variable spring constants schemes, required to estimate the activation energy barriers.
The energy barriers experienced by Al adatoms are fundamental to understand the motion of such impurities and then build up a diffusion model able to correctly describe important physical quantities such as the penetration length and the reaction pathway, still completely missing, but mandatory for improving efficiency in ZnO based electronic devices.

[1] G. Goniakowski et al., Rep. Prog. Phys 71, 016501 (2008).
[2] L.J. Brillson et al., Appl. Phys. Lett. 90, 102116 (2007).
[3] S.B. Zhang, S.-H. Wei, and A. Zunger, Phys. Rev. B 63, 075205 (2001).
[4] Mirco Bazzani, Andrea Neroni, Arrigo Calzolari and Alessandra Catellani, Appl. Phys. Lett. 98, 121907 (2011).
[5] Henkelman, G.; Jonsson, H. J. Chem. Phys. 113, 9978 (2000).

Achievements

The results obtained in this project made it possible to completely characterize the numerical issues associated with NEB algorithm as implemented in the Quantum Espresso suite, to describe the problem of Aluminum penetration and diffusion inside a Zinc Oxide (ZnO) bulk crystal, and at ZnO surfaces. The preliminary tests performed allowed us to find the optimal numerical setup for subsequent large system calculations. The well-known almost linear scalability of the code and the large scale reproducibility of our test systems allowed us to properly plan the forthcoming calculations (ISCRA B in preparation) to achieve the physical information aimed at building up a complete diffusion model for Al diffusion, that is the real scientific objective.
All calculations are based on density-functional theory (DFT) within the generalized gradient approximation (GGA) using the plane-wave pseudo-potential method, in conjunction with Nudge Elastic Band algorithm, that will be fully employed in the future. This method offers the possibility to evaluate the diffusion activation energy and the minimum energy path (MEP), essential quantities for correctly model Al diffusion.
The first step was to perform a series of relax calculations (terminated when the magnitude of the Hellmann–Feynman forces on each ion is less than 0.03 eV/A) designed to determine the stable sites of Al inclusion at non-polar ZnO surfaces, and inner layers, to design a simple diffusion model: these results have been the subject of a Laurea Thesis [1], and have been discussed in a number of internal talks and international conferences.
We furthermore started the evaluation of the shape of the potential energy surface (PES) acting on the dopant for different paths, on an evenly spaced grid, along the high symmetry lines of the non-polar surface [1]. From the evaluation of PES we estimated the preferential diffusion trajectory of Al impurity and the related saddle points that define the energy barriers that the adatom must overcome to diffuse from one local minimum to another. This step is mandatory in order to identify the local minima of the configurations that can be considered as starting/final images for NEB calculations and hence evaluate the minimum energy path.
Although nowadays standard calculations,, NEB simulations themselves require a fine-tuning of the computational frame, for large system calculations (we aim at studying systems with up to 128 atoms, 1152 electrons). We thus performed selected tests to optimize: the k point grid, the type of Climbing Image scheme, and the number of images, the variable elastic constants scheme and the type of optimization scheme, as well as the forces and energy convergence threshold. We subsequently focused on parallelization issues: in particular, we checked the load balancing of system images through a series of performance tests varying the number of images per group of processors, since the code performances can take advantage from the intrinsic subdivision in CPU groups.
All these preliminary tests allowed us not only to find the optimal numerical setup, but also to obtain important information from a physical point of view in order to address the problem of Al diffusion via NEB. Indeed it was possible to reach meaningful indication about dopant incorporation, stability and diffusion anisotropy that will be developed in the subsequent part of the project.

[1] Andrea Neroni, “Meccanismi di drogaggio di film ZnO mediante calculi ab initio”, Tesi di Laurea Specialistica in Scienza e Tecnologia dei Materiali Innovativi”, Universita’ degli Studi di Parma, Novembre 2010.